Geometric Parameterization of Sedimentary Basins in Southern California for Site Response Analysis and Modelling

Final Technical Report on research supported by the United States Geological Survey (USGS) Award G23AP00066

Chukwuebuka C. Nweke, Assistant Professor (PI), chukwueb@usc.edu

Rashid Shams, Graduate Student, rashidsh@usc.edu

Sonny Astani Department of Civil and Environmental Engineering

University of Southern California (USC)

3620 S. Vermont Avenue, Los Angeles, CA 90089-2531

(213) 740-0574

Award Term: 12 Months, January 2023 – December 2023 (Extended, May 2024)

Submitted September 2024

Acknowledgement of Support

This material is based upon work supported by the U.S. Geologic Survey under Grant No. G23AP00066.

Disclaimer

Abstract

Site response in sedimentary basins is influenced by complex three-dimensional (3D) features, including trapped seismic waves, focusing of seismic energy, and resonance of the entire basin structure. Current ground motion models (GMMs) incorporate basin effects using one-dimensional (1D) parameters like V_{S30} and iso-surface depths, which are limited in capturing lateral and 3D effects. This study explores geometric features as predictive parameters to improve site response characterization in sedimentary basins, focusing on the Los Angeles Basin (LAB). Using geological cross-sections and community velocity models, we define the shape and depth constraints of LAB. We then investigate a suite of geometric parameters, including standard deviation of crystalline basement depth, distance from basin margin, and spatial area of influence based on V_{S30} variability, and others. These parameters are designed to capture 2D and 3D seismic site effects that conventional 1D parameters miss. Analyzing a database of Southern California ground motion recordings, we assess current GMMs' performance and develop geometric parameter models using mixed-effect residuals analysis/regressions. These models are incorporated into the Boore et al. (2014) NGA-West2 GMM that was updated by Nweke et al. (2022), with performance evaluated through site terms and site-to-site variability analysis. Results show that parameters like the standard deviation of the difference between sedimentary ($z_{1.5}$ or $z_{2.3}$) and crystalline basement depths (z_{cb}), and spatial area of influence based on V_{S30}, significantly reduce site-to-site variability in the LAB. We also identify biases in V_{S30} scaling between individual Southern California basins, highlighting the need for basin-specific approaches in site response modeling. This research demonstrates the potential of geometric parameters to enhance site response predictions in sedimentary basins, offering a path towards more accurate seismic hazard characterization. The findings emphasize the importance of considering basin-specific characteristics in ground motion modeling and provides a framework for improving current GMMs by accounting for previously neglected multi-dimensional basin effects.

Table of Contents

Chapter 1: Introduction

The devastating impacts of site response during seismic events have been starkly demonstrated throughout history. The 1985 Mexico City earthquake (**M**8.0) caused catastrophic damage up to 350 km from its epicenter, with ground shaking amplified at various sites in Mexico City up to a factor of 8x in the 2 – 4 second period range (Seed et al., 1988). More recently, the 2010 Maule earthquake (**M**8.8) in Chile exhibited amplification factors of up to 4x in the deeper parts of the Santiago basin (Pilz et al., 2011; Assimaki et al. 2012). These events underscore the critical role of local geology in modifying seismic waves and amplifying ground motions, particularly in sedimentary basins.

The physics of seismic wave propagation in complex subsurface media is fundamentally three-dimensional (3D). As seismic waves encounter interfaces between materials with different elastic/plastic properties, they undergo reflection, refraction, and mode conversion (Aki and Richards, 2002). In sedimentary basins, this leads to phenomena such as wave trapping, focusing of seismic energy, and basin-edge generated surface waves (Graves et al., 1998; Kawase, 1996). The resulting ground motions can be significantly amplified and prolonged compared to bedrock sites, with complex spatial and spectral characteristics that depend on basin geometry, impedance contrasts, and the frequency content of the input motion.

Current ground motion models (GMMs) attempt to capture these effects primarily through one-dimensional (1D) parameters such as V_{S30} (time-averaged shear wave velocity in the top 30 meters) and $z_{1.0}$ or $z_{2.5}$ (depth to shear wave velocities of 1.0 or 2.5 km/s) (Abrahamson et al., 2014; Boore et al., 2014, Campbell and Bozorgnia 2014). While these parameters have proven useful, they fail to fully capture the 3D nature of basin response. V_{S30}, being a near-surface measure, does not account for deeper velocity structures that significantly influence long-period motions. The iso-surface depths ($z_{1.0}$ and $z_{2.5}$), while providing some information about basin depth, are essentially point measurements that don't capture lateral variations in basin geometry or the complexities of basin edges.

Studies have shown that sites with identical V_{S30} and $z_{1.0}$ values can exhibit significantly different amplification characteristics due to variations in basin shape and edge effects not accounted for by these parameters (Thompson et al., 2014; Choi et al., 2005). Moreover, the effectiveness of these depth parameters can vary regionally, with some studies finding weak correlations between some iso-surface depths and observed amplifications in certain basins (Day et al., 2008). The iso-surface depths also fail to account for impedance contrasts within the basin (intra-basin features), which can lead to significant amplifications not predicted by simple 1D depth metrics (Bard and Bouchon, 1985). These limitations become particularly apparent in regions with complex 3D velocity structures, where the assumption of 1D wave propagation implicit in these parameters breaks down. An example region is Los Angeles, which is situated atop a complex sedimentary basin. The Los Angeles basin, with its variable depth (up to 10 - 13 km), complex geometry, and heterogeneous fill, presents a significant seismic hazard to millions of residents (Shaw et al., 2015). Current models struggle to accurately predict the spatial variability of ground motions observed in past earthquakes and simulations (Olsen, 2000; Graves et al., 2011).

Given these challenges, there is a pressing need for more sophisticated approaches to characterizing site response in sedimentary basins. Recent advances in 3D velocity modeling (e.g., Lee et al. 2014; Shaw et al., 2015) and high-performance computing have paved the way for more detailed investigations of basin effects. However, translating these insights into practical, computationally efficient GMMs remains a significant challenge.

This study aims to address this gap by exploring geometric parameters that can capture the three-dimensional aspects of basin response while remaining computationally tractable for use in GMMs. By focusing on the Los Angeles Basin as a case study, we seek to develop and validate parameters that can compliment existing site response models, reduce uncertainty, and improve the accuracy of seismic hazard assessments in basin environments.

Our research plan (RP) is structured as follows, where the RP tasks fall under three major parts as shown in Figure 1.1:

1. Basin Shape Definition: We begin by defining the shape and depth constraints of the Los Angeles Basin using a systematic exploration of geological cross-sections and Community Velocity Model profiles. This step is crucial for understanding the basin's three-dimensional structure and identifying key geometric features.
2. Geometric Parameter Investigation: We investigate a suite of geometric parameters, including but not limited to basin centroid, area of basin, distance from basin margin, and basin eccentricity. These parameters are designed to capture aspects of basin geometry that influence seismic wave propagation and amplification.
3. Data Analysis and Residual Computation: Using a comprehensive database of ground motion recordings from Southern California, we perform residual analysis to assess the performance of current GMMs and identify areas for improvement. This step helps us understand where existing models fall short and guides our parameter development.
4. Model Development: We develop geometric parameter models using polynomial fitting techniques. These models are then incorporated into the Boore et al. (2014) NGA-West2 ground motion model that was updated for basin effects by Nweke et al. (2022), creating an enhanced GMM that accounts for more complex basin effects.
5. Performance Evaluation: Finally, we evaluate the performance of these enhanced models through analysis of site terms and site-to-site variability. This step allows us to quantify the ability of our new parameters to reduce bias and uncertainty in basin site response analysis.

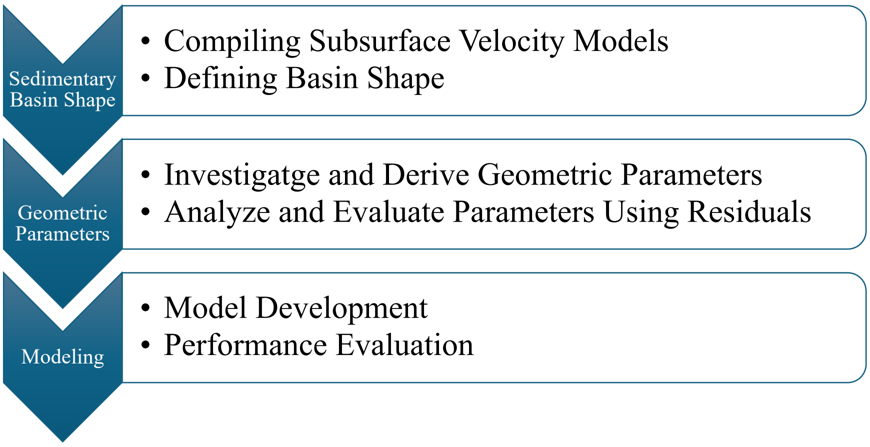

Figure 1.1: Flowchart for the research plan (RP) with each task associated with one of three categories.

Through this systematic approach, we aim to provide a more comprehensive framework for site response modelling in sedimentary basins. This study is structured to systematically address the limitations of current ground motion models and explore new geometric parameters for improving site response characterization in sedimentary basins. Chapter 2 details the database used for this study, outlining the data selection procedures adopted. Chapter 3 presents the ground motion analysis conducted for Southern California (SoCal) data using residual analysis, employing the classical non-reference site approach (Fields and Jacobs, 1995) for site response computation.

In Chapter 4, we delve into the site response of the Los Angeles Basin (LAB), providing a comprehensive overview of its geology. We compute the site response for LAB, investigate mean site terms, and evaluate the performance of V_{S30}. Chapter 5 focuses on defining the shape of LAB through an extensive study of geological cross-sections, establishing basement constraints for the basin. Chapter 6 forms the core of our research, detailing the computation and analysis of various geometric parameters explored for LAB. We investigate their performance in relation to V_{S30} and identify alternative parameters that show potential to complement V_{S30} in ground motion models.

Chapter 7 extends this analysis by developing V_{S30} scaling models for SoCal site classes and individual basins, examining the biases and differences between V_{S30} scaling in different basins and the SoCal scaling model (Nweke et al., 2022). The culmination of our analysis is presented in Chapter 8, where we model selected geometric parameters and investigate their performance when incorporated into the site component of ground motion models. We evaluate the impact on mean site terms and the reduction in site-to-site variability achieved by incorporating these additional geometric parameter models. Finally, Chapter 9 synthesizes our findings, presenting major recommendations, acknowledging limitations, and outlining the future scope of this work. The results of this study will improve the accuracy of seismic hazard assessments, particularly in urban areas situated within sedimentary basins, and contribute to more effective earthquake engineering practices.

Chapter 2: Database

2.1 Data Source and Processing

This study utilizes a comprehensive dataset compiled from the NGA-West2 database and supplemented by data from related efforts (Wang and Stewart 2019; Ahdi et al. 2020). For the purposes of this research endeavour, we refer to it as NGA-West2+. The dataset covers ground motion recordings in Southern California from 1938 to 2020. All newly added data has been processed using Next Generation Attenuation (NGA) procedures (Ancheta et al. 2014; Kishida et al. 2020), ensuring consistency with the existing NGA project datasets. This included applying, to each waveform/time history record, instrument corrections, high and low pass filters, and baseline corrections, all to remove non-earthquake signal (noise), drifts and unwanted/unjustified displacements, as well as establish a usable range for the data (minimum usable frequency is taken as 1.25 times the high pass corner frequency). Metadata for each new event and station has been comprehensively compiled.

2.2 Geographic Focus and Data Selection

Our study focuses on the Southern California region given its complex geology, high seismic risk, and dense network of data availability. This is displayed in Figure 2.1 which identifies the location of ground motion recording stations, their distribution in the study region, the categorization of site as a basin, non-basin, or intermediate (basin edge and valley), and the location/outline of the major sedimentary basins. For the region, the compiled dataset is comprised of 189 events recorded by approximately 1000 stations/sites in Southern California, yielding a total of 10850 recordings.

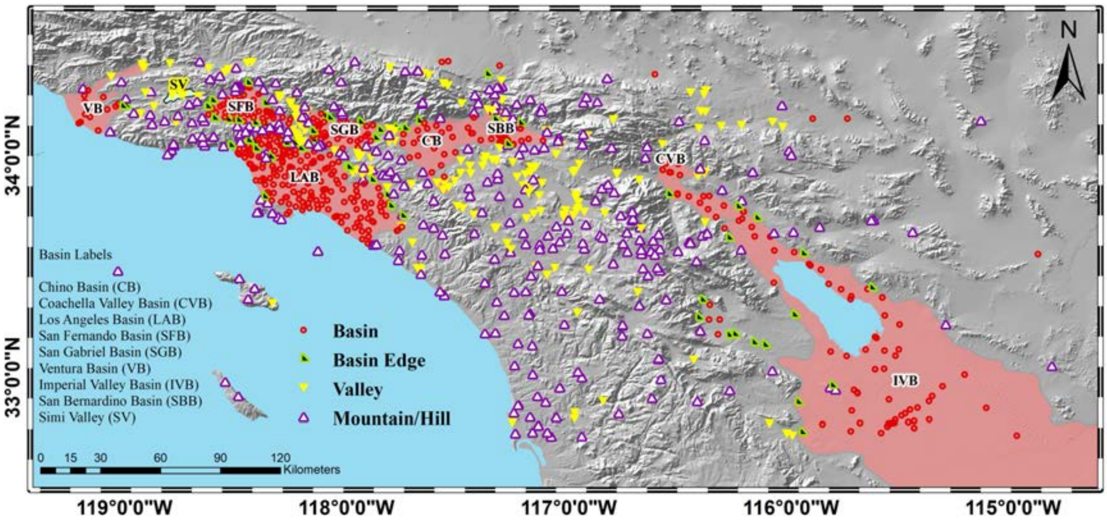

Figure 2.1: Sedimentary Basins in Southern California with seismic stations marked according to their site class (basin, basin edge, mountain, and valley)

To mitigate bias from distant records (Ancheta et al. 2014), avoid spurious fictitious non-linear site effects from low magnitude events (Stafford et al. 2017), and ensure a robust estimate of site terms, we applied the following data selection criteria:

1. Magnitude-distance cutoff as suggested by Boore et al. (2014)
2. Minimum magnitude threshold of 3.95
3. Minimum of 3 recordings per station

After applying these filters, our final dataset for consists of 132 events recorded by 648 stations, totaling 7968 recordings. The subset of this data for the Los Angeles basin consists of 87 events, 132 stations/sites (shown in Figure 2.2), for a total of 1122 recordings. The magnitude range of the selected events is 3.95 to 7.3, and the distance range is 0 to 400 km.

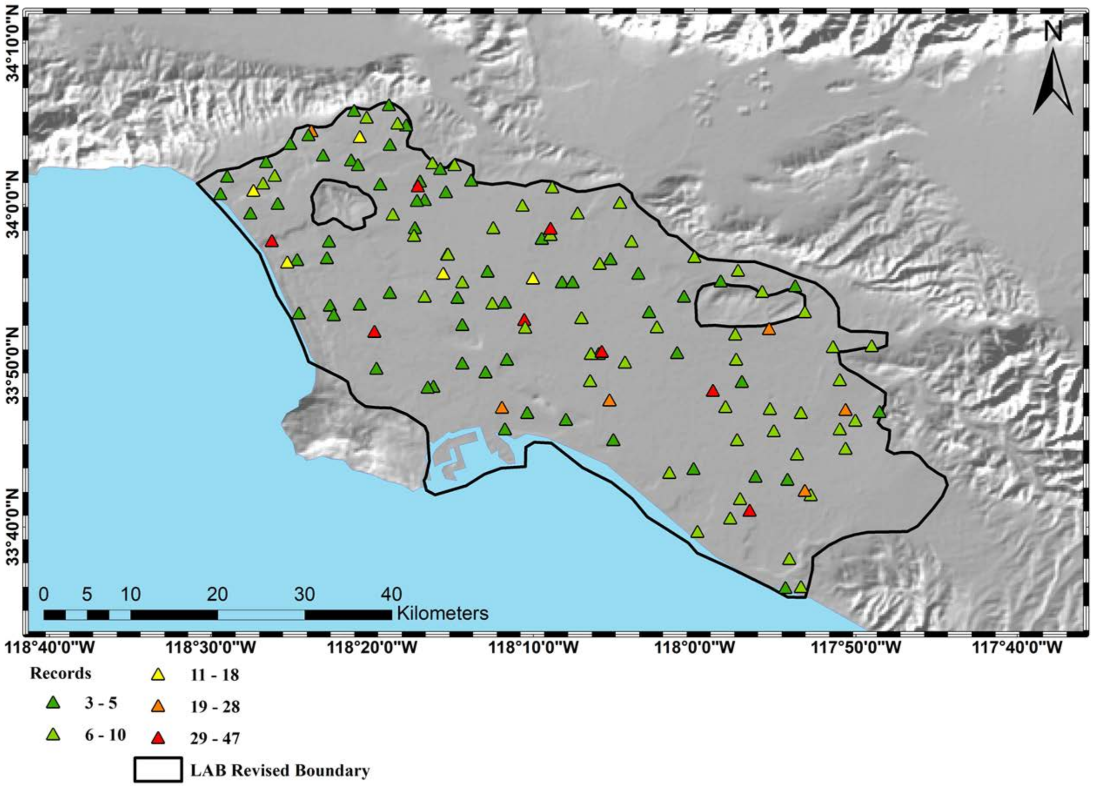

Figure 2.2: Los Angeles Basin boundary (Nweke et al. 2022) with stations in LAB colour coded based on the number of recordings at each station from NGA-West2 plus dataset. (showing stations with 3 or more recordings)

2.3 Metadata and Site Parameters

For each earthquake recording, extensive effort was made to aggregate a validated set of metadata including:

- Event parameters (magnitude, event hypocenter coordinates, focal mechanism)
- Path parameters (distance metrics, azimuth)
- Site parameters (V_{S30}, iso-surface depths/basin depths: $z_{1.0}$ and $z_{2.5}$)

The site metadata, crucial for our analysis, includes V_{S30} values (combination of those derived from measurements and those from proxies) and basin depths queried from the Community Velocity Models (CVMs). Specifically, we use updated basin depth values from the recent models: CVM-S4.26.M01 (Lee et al., 2014) and CVM-H v15.1 (Shaw et al., 2015). Figure 2.3 presents histograms showing the distribution of key parameters: magnitude, joyner-boore distance, V_{S30}, and basin depth ($z_{1.0}$). These distributions highlight the gaps (limited magnitude coverage; skewed $z_{1.0}$ estimates emphasizing likely erroneous zero depth sites) and benefits (log normal distribution of V_{S30}; good coverage of distances) of the available dataset. However, when compared to the global dataset NGA-West2+, we observed that the Southern California subset exhibits strong consistency in magnitude-distance space as revealed in Figure 2.4. Figure 2.4 also shows that the distance (R_{jb}) coverage shown in Figure 2.3 still suffers from a lack of representation in close distance sites for critical magnitudes (M≥5).

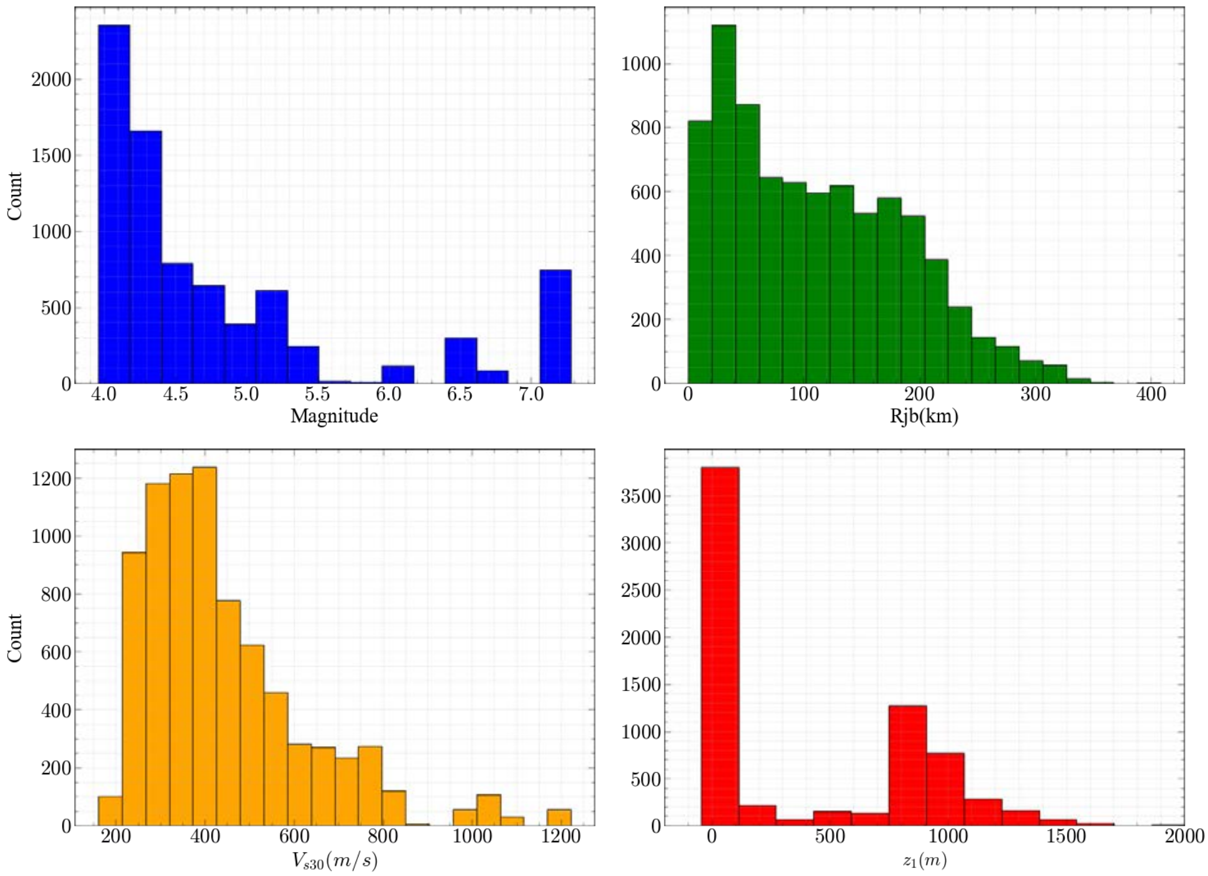

Figure 2.3: Histogram for NGA-West2 plus SoCal dataset showing distribution of Magnitude, Distance, V_{s30} and Basin depth ($z_{1.0}$) from CVMH (Shaw et al. 2015).

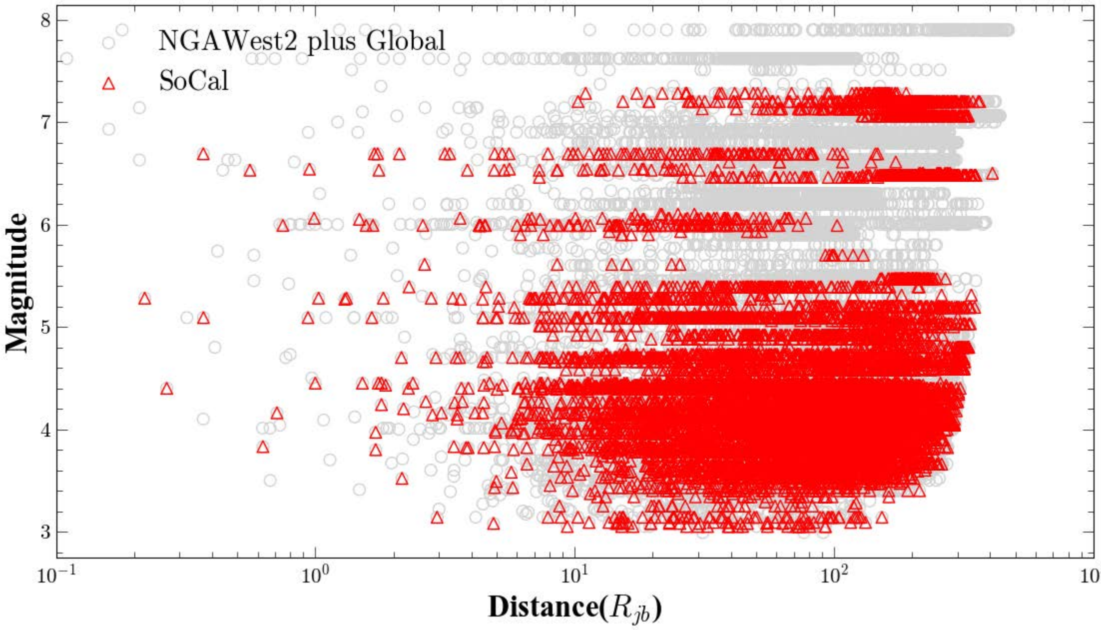

Figure 2.4: Shows whole NGAWest2 plus records as well as SoCal records (with red markers)

Upon inspection of the dataset as a function of period, it can be seen that NGA-West2+ more than doubles the available number of recordings, even though more than half of it is unusable beyond T = 3 seconds, as shown in Figure 2.5. This limits the robustness of the analysis to estimate long period site effects, but the provision of twice the number of records counters those issues.

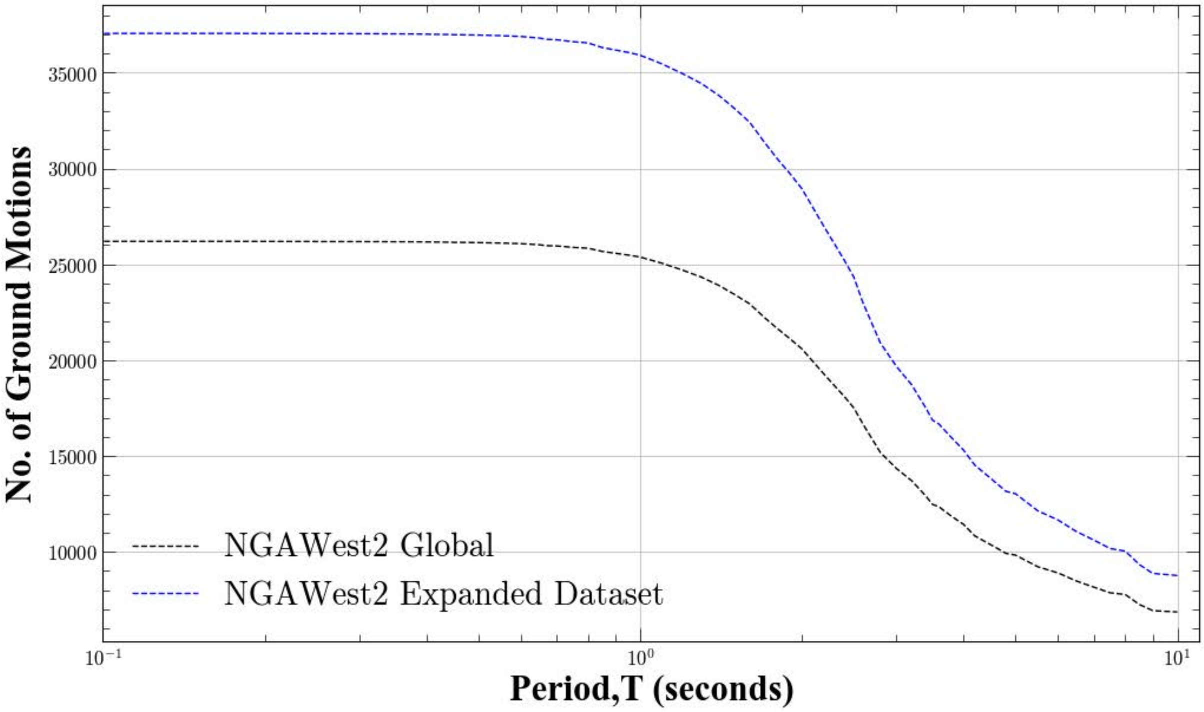

Figure 2.5: Shows number of ground motions (recordings) with period (sec) available for analysis in NGA-West2 dataset global (black line) and recordings in SoCal (blue line) based on SoCal study region shown in Figure 2.

This dataset forms the foundation for our subsequent analyses of site response in the Los Angeles Basin and the development of new geometric parameters for improving ground motion predictions.

Chapter 3: Ground Motion Residual Analysis for Southern California (SoCal)

3.1 Residual Analysis

In the context of seismic hazard assessment, ground motion models (GMMs) play a crucial role in predicting the intensity of shaking at a given site for a specified earthquake scenario. However, these models are inherently imperfect representations of complex physical processes. To evaluate and improve these models, we employ residual analysis, a powerful statistical tool that quantifies the discrepancies between observed ground motions and model predictions.

3.1.1 Definition and Importance of Residuals

A residual, in its simplest form, is the difference between an observed value and its predicted counterpart. In ground motion modeling, we define the residual as:

$$R_{ij} = \ln(Y_{ij}) - \mu_{ij} \tag{1}$$

where R_{ij} is the residual, Y_{ij} is the observed ground motion intensity measure, and μ_{ij} is the median prediction from the GMM (in natural log units, as is the same for the prior two components). The indices i and j refer to a specific earthquake and recording station, respectively. We use the natural logarithm to account for the lognormal distribution typically observed in ground motion intensities (Abrahamson and Youngs, 1992). In general, residual analysis serves several critical purposes:

1. It provides a means to identify systematic biases in the model predictions.
2. It quantifies the model's predictive uncertainty.
3. It guides model refinement by highlighting areas where predictions consistently deviate from observations.

3.1.2 Components of Ground Motion Residuals

The total residual for a ground motion observation can be decomposed into several components, each representing different sources of variability. These components can be categorized as fixed effects (systematic biases) and random effects (aleatory/epistemic in nature).

Fixed effects are systematic deviations that are consistent across multiple observations and can, in principle, be predicted and corrected. Random effects, on the other hand, represent inherent variability that cannot be predicted deterministically (Al Atik et al., 2010). We can represent this decomposition as:

$$R_{ij} = c_k + \eta_{ei} + \delta W_{ij} \tag{2}$$

where:

- c_k is the overall model bias (a fixed effect)
- η_{ei} is the event term, representing deviations for a specific earthquake (a random effect at the inter-event level)
- δW_{ij} is the within-event residual (a random effect at the intra-event level)

The within-event residual (δW_{ij}) can be further decomposed to isolate different sources of variability:

$$\delta W_{ij} = \eta_{sj} + \eta_{pij} + \varepsilon_{ij} \tag{3}$$

where:

- η_{sj} is the site term, representing site-specific deviations (a random effect at the site level)
- η_{pij} is the path term, accounting for path-specific effects (a random effect at the path level)
- ε_{ij} is the remaining residual, representing unexplained variability

3.1.3 Mixed-Effects Analysis for Residual Partitioning

To partition the total residual into its components, we employ mixed-effects analysis, a statistical technique that can simultaneously estimate fixed and random effects (Abrahamson and Youngs, 1992). This approach allows us to isolate the contributions from the event and local site features, respectively, to the manifested earthquake ground shaking recording, despite the interdependencies due to the path.

We implement a two-stage mixed-effects regression analysis (Rodriguez-Marek et al. 2014; Stafford et al, 2014) that provides estimates of the residual components using Eq. 2, and subsequently estimates the components for Eq. 3. The following model is a complete representation of the two-stage approach:

$$R_{ij} = c_k + \eta_{ei} + \eta_{sj} + \varepsilon_{ij} \tag{4}$$

This analysis is performed using the lme4 package in R (R Core Team 2019; Bates et al., 2015), executed as a subroutine within our main Python script (Gautier, 2009).

3.1.4 Model Evaluation through Residual Analysis

By examining the patterns in these residual components, we can evaluate the performance of the GMM and identify areas for improvement. For instance:

1. A non-zero c_k indicates overall model bias.
2. Trends in η_{ei} with magnitude suggest inadequacies in the model's magnitude scaling.
3. Patterns in δW_{ij} with distance may reveal issues with the model's distance scaling.
4. Systematic variations in η_{sj} could point to deficiencies in the site response component of the model.

In this study, we apply this residual analysis framework to evaluate different components of the site response in the Boore et al. (2014) GMM (BSSA14), complemented with the Southern California basin model developed by Nweke et al. (2022) (henceforth termed the BSSA14-NEA22 GMM). Specifically, we compute three different sets of residuals:

1. Reference-rock site terms (η_{sj}^{r}): These residuals are computed by setting V_{S30} = 760 m/s (the reference site condition), effectively removing the site response component from the model.
2. V_{S30}-scaled site terms (η_{sj}^{v}): These residuals include only the V_{S30}-scaling component but do not include the basin-specific component.

3. Full model site terms (η_{sj}^{b}): These residuals incorporate all currently established site response components, including both V_{S30}-scaling and basin-specific effects.

By analysing these three sets of residuals, we aim to quantitatively assess the predictive capabilities of our proposed geometric parameters in comparison to the current GMM site parameters (V_{S30}, z_x, basin category). This comparative analysis serves two crucial purposes:

1. It will help identify which geometric parameters are viable options worth pursuing for the development of a new GMM site component model. This is essential for improving the accuracy and reliability of ground motion predictions, particularly in complex basin environments.
2. It will elucidate the underlying mechanisms driving the predictive power of current models, highlighting both their strengths and limitations in capturing site response effects. Understanding the strengths and limitations of existing parameters will guide our approach in developing more comprehensive and accurate site response models.

This comprehensive residual analysis approach will enable us to systematically evaluate the potential of new geometric parameters to capture basin effects, which is the primary focus of our study. By doing so, we aim to contribute to the advancement of ground motion modeling, particularly in regions with complex basin structures.

It's important to note that while we explicitly estimate event terms (η_{ei}) and site terms (η_{sj}), we do not specifically estimate path terms (η_{pij}) in our mixed-effects analysis. Instead, we assess the adequacy of the path scaling in the model by examining the within-event residuals (δW_{ij}) as a function of distance. This approach allows us to check if our dataset covers a sufficient variety of paths such that any path-specific biases cancel out on average. The results of these residual assessments will be presented in the subsequent section.

3.2 Results for GMM Assessment Using Residual Analysis

The methodology described in Section 3.1 forms the foundation for our evaluation of newly derived geometric parameters. By estimating site residuals, we aim to assess which parameters show significant predictive power, indicated by appreciable trends with site terms. This assessment will guide our selection of viable parameters for further model development.

Before we can confidently use these site residuals for evaluating geometric parameters, it is crucial to verify the performance of the underlying ground motion model, particularly its magnitude and distance scaling components. While Nweke et al. (2022) previously conducted this assessment, we repeat it here for validation and confirmation purposes, especially given our expanded dataset.

This section presents the results of our assessment of the BSSA14-NEA22 GMM, focusing on model bias, magnitude scaling, distance scaling and path effects, and site terms. By systematically reviewing these components, we establish the reliability of our site residuals for subsequent geometric parameter evaluation.

3.2.1 Model Bias

We first examine the overall model bias (c_k) to ensure the BSSA14-NEA22 GMM provides a suitable baseline for our analysis. Figure 7 illustrates c_k as a function of period.

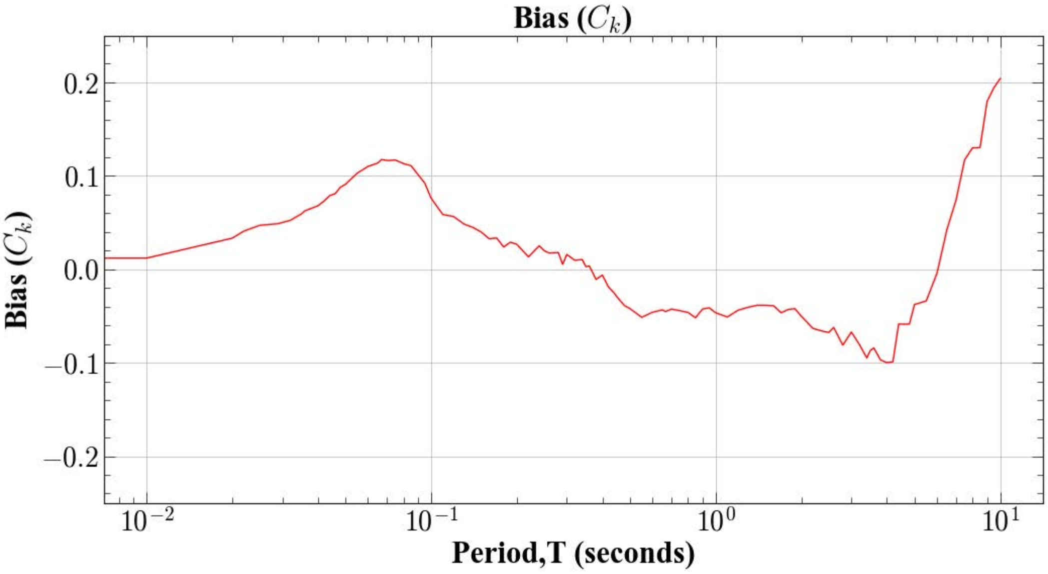

Figure 0.1.1: Model Bias (c_k) with period using the SoCal dataset based on BSSA14-NEA22 GMM and basin depths from CVM-H model.

The relatively small values of c_k across most periods (86% on an average between ± 0.1) indicates a general compatibility between the model predictions and the observed data. This confirms that the BSSA14-NEA22 GMM serves as an appropriate foundation for our subsequent analyses.

3.2.2 Magnitude Scaling

To verify the adequacy of the GMM magnitude scaling, we examine the derived event terms (η_{ei}). Figure 3.2 displays η_{ei} as a function of period for both the global NGA-West2+ dataset and the SoCal subset.

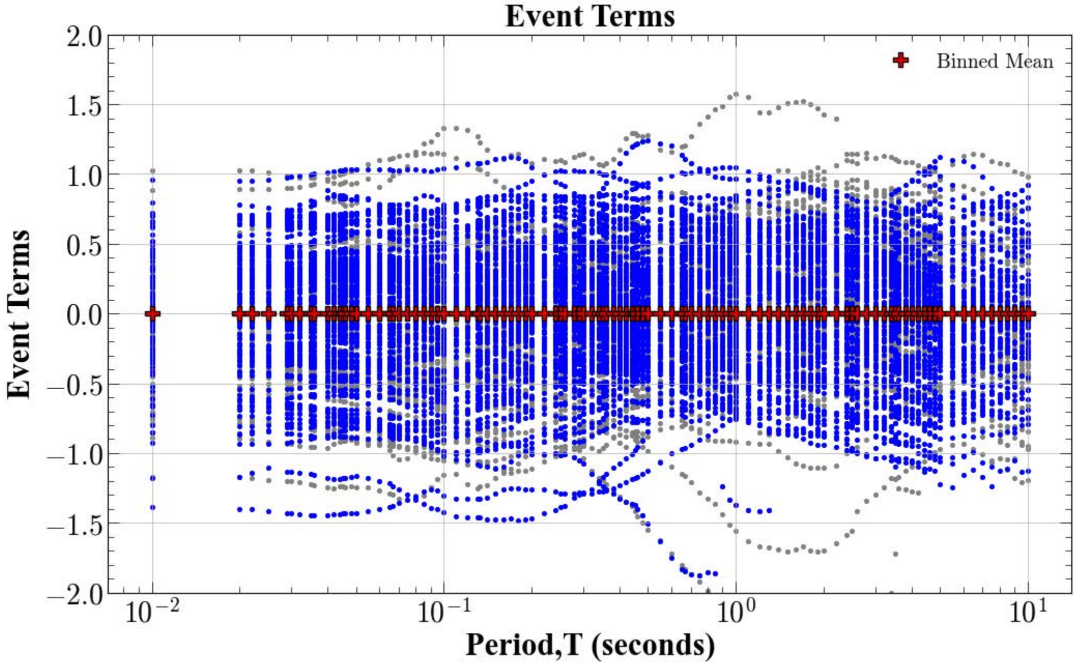

Figure 3.2: Event Terms with period using full NGA-West2+ dataset (grey markers) where blue markers highlight SoCal data based on BSSA14-NEA22 GMM with basin depths from CVM-H.

The clustering of binned means (red markers representing the average trend on the data) around zero validates our mixed-effects analysis approach. To further assess magnitude scaling, we plot η_{ei} against magnitude for various spectral periods (shown in Figure 3.3).

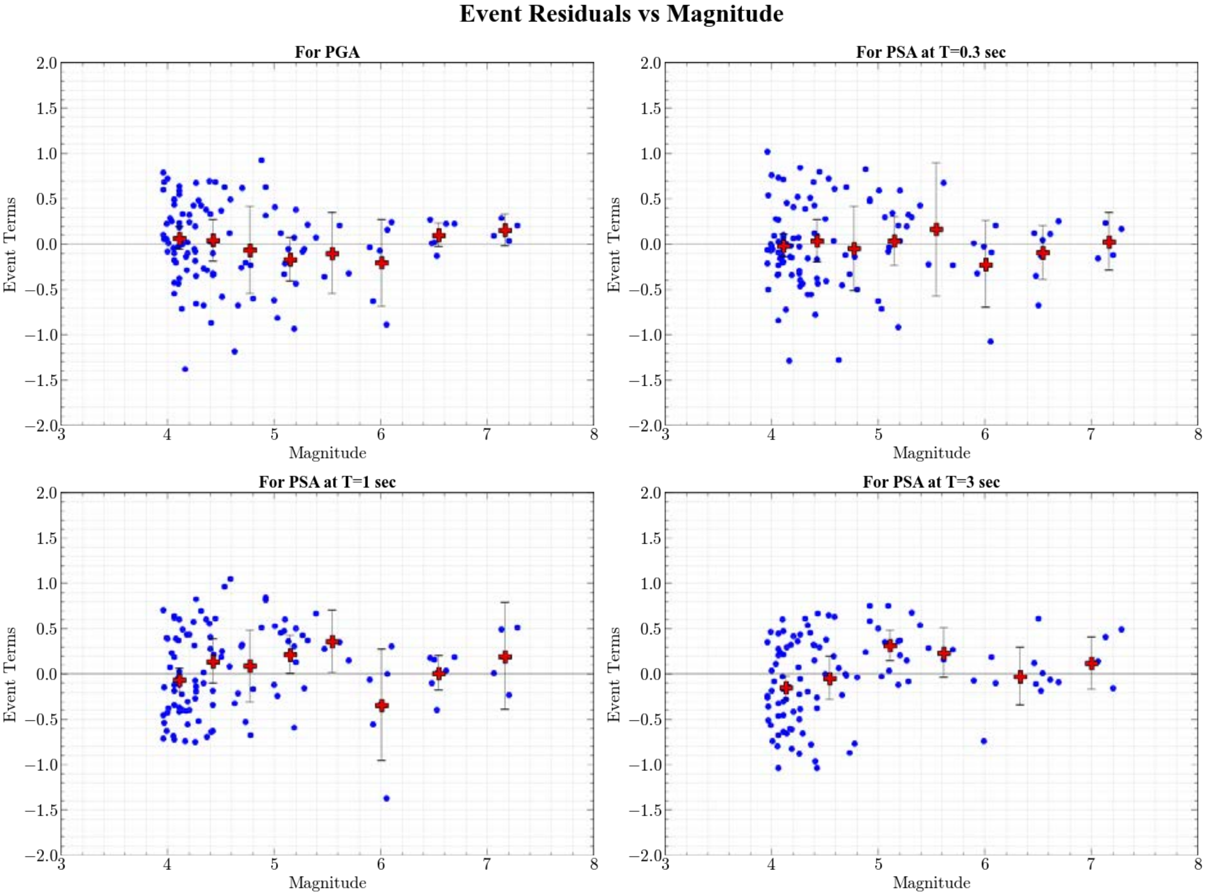

Figure 3.3: Event Terms as a function of event magnitude for SoCal dataset where red markers show binned means.

The absence of clear trends in Figure 3.3 suggests that the magnitude scaling in the BSSA14-NEA22 GMM adequately captures the data trends for Southern California, confirming the findings of Nweke et al. (2022) with our expanded dataset.

3.2.3 Distance Scaling and Path Effects

Although we do not explicitly estimate path terms (η_{Pij}), we assess the adequacy of distance scaling by examining within-event residuals (δW_{ij}) as a function of distance. Figure 3.4 presents these residuals for PGA, Sa (0.3), Sa (1.0), and Sa (3.0) for the Southern California subset.

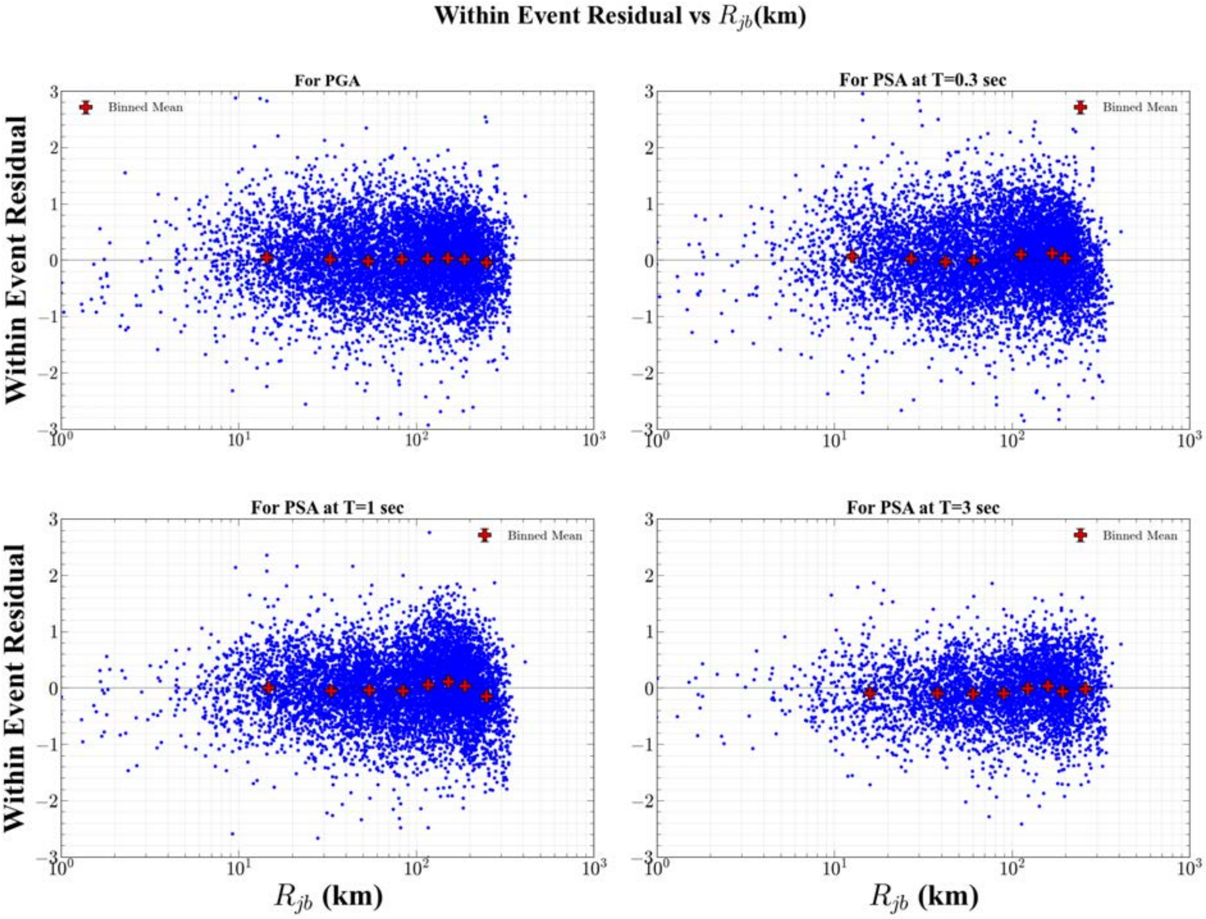

Figure 3.4: Within-Event residuals plotted as a function of Joyner-Boore distance for SoCal dataset where red markers show binned means. There are no trends in the data which indicates path scaling is unbiased for the region in the GMM.

The lack of clear trends in Figure 3.4 indicates that the path scaling in the model is unbiased for our dataset. This observation supports the assumption underlying the non-reference site approach for estimating site effects - that path biases average approximately to zero and do not significantly bias the site term estimates (Field and Jacobs 1995).

3.2.4 Site Terms

With the magnitude and distance scaling components verified, we can confidently examine the site terms (η_{sj}) computed based on the BSSA14-NEA22 GMM. Figure 3.5(a) shows the reference-rock site terms for PGA and PSA at T= 1 second plotted against V_{S30}. Figure 3.5(b) shows the impact of adding the V_{S30}-scaling component, which is depicted by the reduction in the positive shit in bias. Figure 3.5(c) versus the reference condition that does not consider a site parameter.

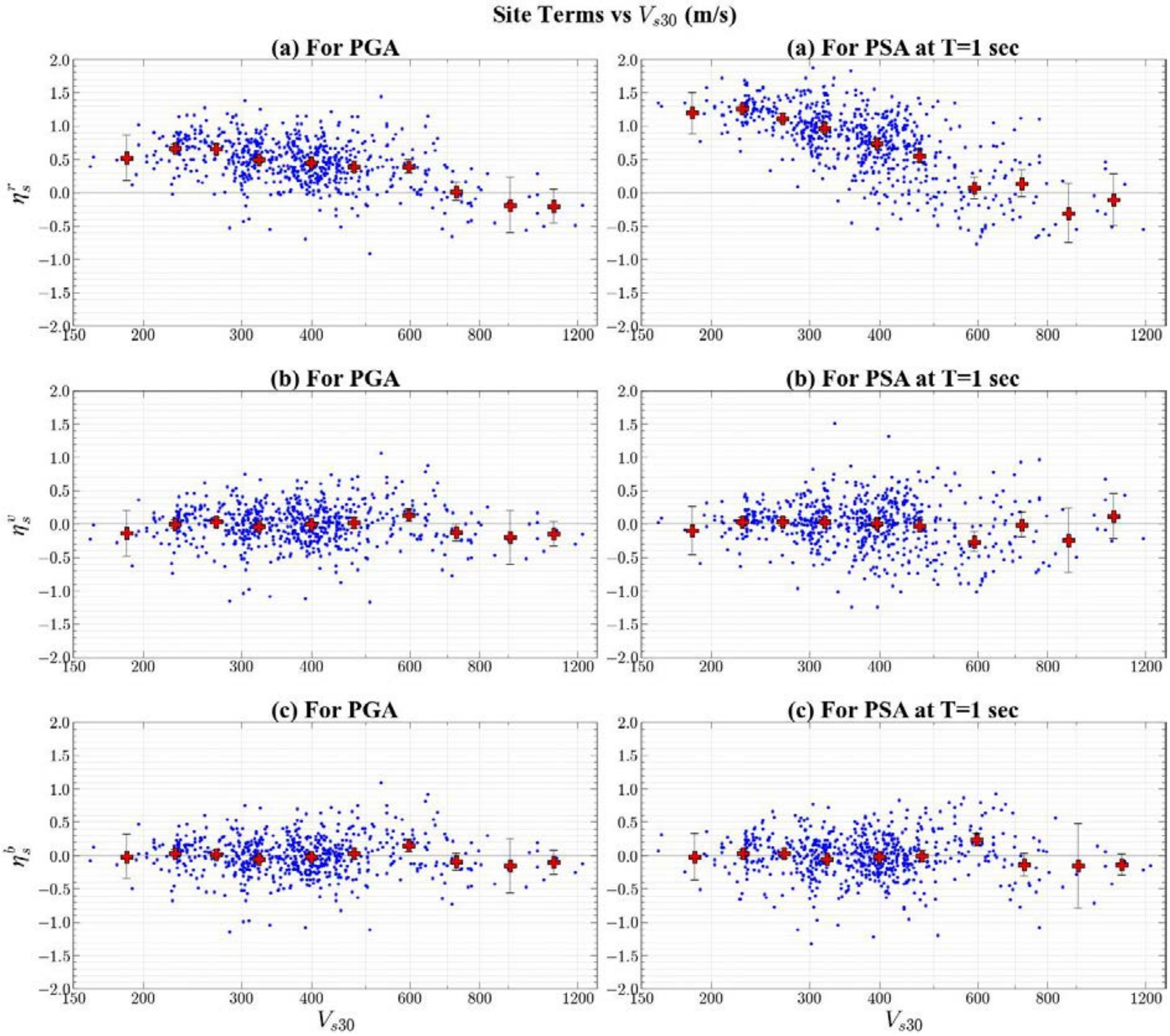

Figure 3.5 (a): Site Terms (η_{sj}^{r}) (based on full BSSA14-NEA22 GMM) shown as a function of V_{S30} for SoCal dataset where red markers show binned means for the data. (b) Site Terms (η_{sj}^{v}) shown as a function of V_{S30} for SoCal dataset where red markers show binned means for the data. (c) Site Terms (η_{sj}^{b}) shown as a function of V_{S30} for SoCal dataset where red markers show binned means for the data.

These V_{S30}-dependent (and basin-dependent) site terms approximately represent the difference between average site amplification and the model predictions. The patterns observed in these plots will serve as a baseline for comparing the performance of our new geometric parameters.

3.2.5 Implications for Geometric Parameter Evaluation

The results of this assessment of the GMM using residual analysis provide a solid foundation for our subsequent investigations of geometric parameters. We have confirmed that:

1. The BSSA14-NEA22 GMM shows minimal overall bias.
2. Magnitude scaling is adequately captured.
3. Distance scaling is unbiased across our dataset.
4. Site terms show patterns that may be improved upon.

These findings validate our approach and allow us to proceed with confidence in evaluating new geometric parameters. In the following chapters, we will explore how these parameters can potentially address residual patterns in site terms and improve ground motion predictions in basin environments.

Chapter 4: Site Response in Los Angeles Basin

4.1 Geology and Geologic History of the Los Angeles Basin

Understanding the geological context of the Los Angeles Basin (LAB) is crucial for interpreting site response characteristics and developing effective geometric parameters. This section provides a detailed overview of the basin's formation, structure, and composition, synthesizing findings from multiple studies.

4.1.1 Basin Formation and Evolution

The Los Angeles Basin's evolution is best understood through two complementary models: the five-phase model by Yerkes et al. (1965) and the three-stage model by Ingersoll and Rumelhart (1999). These models, while using different approaches, together provide a comprehensive picture of the basin's complex history. Yerkes et al. (1965) described the basin's evolution in five major phases:

1. Pre-depositional phase: Formation of the heterogeneous basement upon which later sediments accumulated.
2. Pre-basin phase: Deposition of upper Cretaceous to lower Miocene rocks, primarily marine clastic sedimentary deposits.
3. Basin inception phase: Differential emergence and erosion across the basin, marking the beginning of the LAB as a distinct structure.
4. Principal phase: Accelerated subsidence and continuous deposition, largely responsible for the basin's present form and structure.
5. Modern phase: Continued sedimentation in the central basin, with additional sediments derived from surrounding uplifts.

Ingersoll and Rumelhart (1999) proposed a three-stage evolution model that focuses on the tectonic forces shaping the basin:

1. Rifting Stage (18-13 Ma): Characterized by extension and rifting, resulting in the initial formation of the basin. This stage correlates with the pre-depositional and early pre-basin phases of Yerkes et al. (1965), representing the creation of accommodation space for sediment accumulation.
2. Translational Stage (13-6.5 Ma): Marked by the transition to strike-slip faulting and the development of local basins. This stage saw the deposition of submarine fan systems and the initial subsidence of the central trough. It aligns with the later pre-basin phase, basin inception phase, and early principal phase of Yerkes et al. (1965), representing the period of major sediment accumulation and basin deepening.
3. Compressional Stage (6.5 Ma-present): Dominated by north-south compression, leading to structural inversion, folding, and uplift. This stage resulted in the modern basin configuration and the development of major structural features. It corresponds to the later principal phase and the modern phase of Yerkes et al. (1965), representing the final shaping of the basin and ongoing tectonic activity.

From an engineering perspective, this evolutionary history is crucial for understanding the basin's current structure and its influence on seismic wave propagation. The Rifting Stage created the initial basin geometry, the Translational Stage led to significant sediment accumulation and fault system development, and the Compressional Stage resulted in the complex folded and faulted structure we observe today. Each stage contributed to the formation of the thick sedimentary sequence that now influences site response across the Los Angeles Basin.

4.1.2 Basin Structure and Depth

The Los Angeles Basin is characterized by a complex three-dimensional structure, as revealed by studies such as Shaw et al. (2015) and Ma and Clayton (2016). The basin's overall shape is that of a large structural syncline with a central axis trending southeast to northwest from Santa Ana to Beverly Hills (Yerkes et al., 1965).

The sediment-basement interface that marks the bottom of the basin (basin depth) varies significantly, ranging from less than 1 km in the northeast to over 8 km in the central parts. This depth variation is asymmetric, with the basin deepening more gradually from the northeast and more steeply from the southwest. Key structural features include major depocenters, particularly in the central trough and the Compton-Los Angeles domain, representing areas of maximum subsidence and sediment accumulation.

The basin's structure is further defined by a network of faults. The Santa Monica fault system bounds the northern edge, while the Newport-Inglewood fault traverses the central portions of the basin. The Whittier fault runs along the northeastern margin, and the Palos Verdes fault defines the southwestern edge. These fault systems contribute significantly to the basin's complex geometry and sediment distribution. The basin is also bounded by several significant features. To the north lie the Santa Monica Mountains and Elysian Hills, while the eastern edge is defined by the Puente Hills and Repetto Hills. The Santa Ana Mountains border the basin to the south, while the western parts of the basin extends into the Pacific Ocean.

The Moho depth provides context for the overall crustal structure, ranging from about 17 km beneath the center of the basin to 27 km at the basin edges. This variation in Moho depth influences the propagation of seismic waves from deep earthquakes, adding another layer of complexity to the seismic response of locations within the basin.

These structural elements collectively contribute to the Los Angeles Basin's complex geometry. The significant variations in basin depth, the complex geometry of the sediment-basement interface, and the network of faults all play crucial roles in shaping the basin's structure.

4.1.3 Sedimentary Composition

The Los Angeles Basin is composed of a complex sequence of rocks and sediments, reflecting its long and varied geological history. This includes the basement rocks, the lower and upper sequences, and the surficial units.

Basement Rocks:
The basement of the Los Angeles Basin consists primarily of Catalina Schist and igneous rocks (Shaw et al., 2015). The Catalina Schist, a metamorphic rock formed during the Mesozoic era, is predominantly found in the western and central parts of the basin. In the eastern parts, the basement transitions to igneous rocks, primarily granitic in nature, similar to those exposed in the San Gabriel Mountains. This variation in basement rock type is a result of the different tectonic processes that shaped the region during the Rifting Stage of basin formation (Ingersoll and Rumelhart, 1999).

Lower Sequence:
Overlying the basement rocks is the lower sequence, composed predominantly of marine sedimentary rocks of Miocene age (Wright, 1991; McCulloh and Beyer 2003). This sequence includes:

1. The Topanga Group: Comprising marine sandstones and volcanic rocks, deposited during the middle Miocene (about 16-11 Ma). These rocks represent the early stages of basin subsidence and marine transgression.
2. The Monterey Formation: A widespread unit of organic-rich shales and siliceous rocks, deposited in a deep marine environment during the middle to late Miocene (about 13-6 Ma). This formation is particularly important as a source rock for hydrocarbons in the basin.

The distribution of these units varies across the basin, with thicker accumulations in the central and western parts, reflecting the asymmetric nature of basin subsidence (Sawyer et al. 1987).

Upper Sequence:
The upper sequence consists of late Miocene to Quaternary sedimentary rocks, including both marine and non-marine deposits:

1. The Pico Formation: Marine sandstones and siltstones of Pliocene age (about 5-2 Ma), deposited during a period of rapid basin subsidence and sediment influx.
2. The Repetto Formation: Marine sandstones and shales of early Pliocene age (about 5-3 Ma), representing deep-water fan deposits.
3. The San Pedro Formation: Pleistocene marine and non-marine sandstones and gravels, reflecting the gradual filling of the basin and transition to surface/terrestrial environments.

These formations show a general trend of shallowing upward, indicating the progressive filling of the basin.

Surface Geology:
The surface geology of the Los Angeles Basin is dominated by Quaternary alluvial deposits, as shown in Figure 4.1. These deposits are primarily the result of sediment transport and deposition by rivers draining the surrounding mountains, particularly the Los Angeles River, San Gabriel River, and Rio Hondo River.

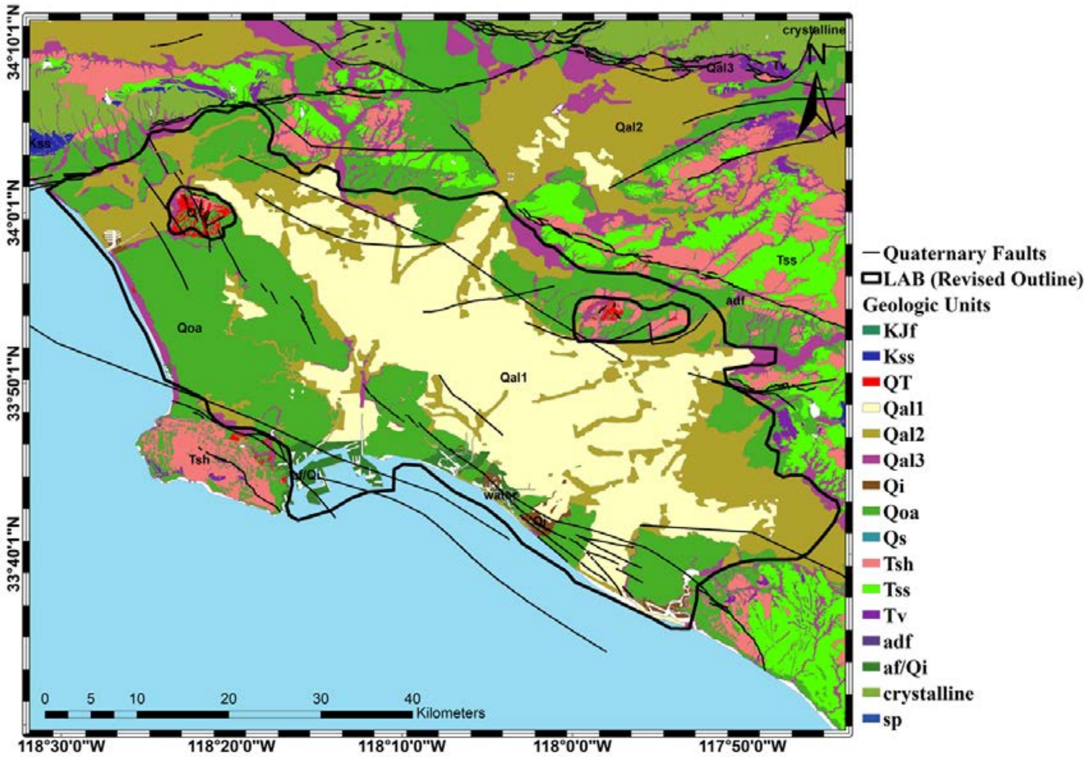

Figure 4.1: Geology of Los Angeles Basin from Wills et al. (2015) map.

The distribution of these surface deposits has been significantly influenced by geomorphological processes. This includes alluvial fans that are found at the base of the surrounding mountains, representing areas of sediment deposition where steep mountain streams transition to the flatter basin floor; floodplains that are comprised of extensive areas of flat-lying alluvium deposited by the rivers during major flood events; and along the western margin of the basin, beach and dune deposits reflect coastal influences.

Historical events have also shaped the surface geology. For instance, the Los Angeles River has changed course several times in recorded history, most notably in 1825 when it shifted from its western outlet near Marina Del Rey to its current southern outlet in Long Beach. These course changes have resulted in the redistribution of surface sediments across the basin. Human-induced changes have also played a role in recent times. Extensive urbanization has led to significant areas of artificial fill, particularly in low-lying areas and along the coast.

Figure 12 illustrates this complex surface geology, showing the predominance of alluvium and older alluvium deposits across much of the basin floor, with older sedimentary units exposed in the surrounding hills and mountains. Understanding this sedimentary composition and its spatial variation is crucial for interpreting seismic site response across the Los Angeles Basin, as different sedimentary units can significantly affect the amplification and propagation of seismic waves.

4.1.4 Implications for Seismic Response

The complex geology and structure of the Los Angeles Basin significantly influence seismic site response:

1. Basin Geometry and Depth: The asymmetric shape and variable depth (< 1 km to > 8 km) affect seismic wave propagation by: (a) Focusing seismic energy, particularly in

deeper parts; (b) Generating and trapping surface waves, especially at basin edges; (c) Amplifying ground motions due to impedance contrasts.

2. Sedimentary Sequence: The thick accumulation of sediments significantly influences site response via: (a) Complex velocity structures created by the shallowing-upward trend in the sedimentary sequence affects wave propagation and amplification; (b) Different sedimentary units (e.g., marine shales vs. alluvial deposits) have varying mechanical properties, leading to complicated site response across the basin.
3. Lateral Heterogeneity: The spatial variation in sediment thickness and composition across the basin can lead to complex patterns of amplification and resonance. This is particularly evident in: (a) The transition zones between different sedimentary units; (b) Areas near the basin edges where sediment thickness changes rapidly.
4. Fault Systems: The network of faults within and bounding the basin, can influence wave propagation and local site effects by: (a) Creating localized zones within the basin, and (b) Potentially channeling seismic energy along fault planes.
5. Surface Geology: Quaternary alluvial deposits that dominate the surface geology can: (a) Significantly amplify ground motions due to their low seismic velocities and potential for nonlinear behavior during strong shaking; and (b) The spatial distribution of various geomorphological features like alluvial fans and floodplains can also lead to spatial variations in site response.
6. Deep Crustal Structure: Variations in Moho depth (17-27 km) influence the propagation of seismic waves from deep earthquakes.

These geological features and their interplay underscore the need for sophisticated, three-dimensional approaches to characterizing site response in the Los Angeles Basin. The complex basin structure highlights the challenges in predicting site response and emphasizes the importance of considering basin-specific characteristics in seismic hazard assessments. This complexity also underscores the potential value of new geometric parameters that can capture these three-dimensional effects, which is the focus of this study.

4.2 Site Response in Los Angeles Basin and Current GMM Site Parameters (V_{S30}, $z_{1.0}$, and Basin Category)

Building upon our understanding of the Los Angeles Basin's (LAB) complex geology, this section examines the site response characteristics of the basin and evaluates the performance of conventional site parameters, particularly V_{S30}, $z_{1.0}$, and basin category, in capturing these effects.

4.2.1 Computation of Site Response

We computed site response in the LAB using the Southern California (SoCal) dataset and the residual analysis methodology described in Chapter 3. Our analysis employs the Boore et al. (2014) Ground Motion Model (BSSA14 GMM), which incorporates V_{S30} and basin depth ($z_{1.0}$) as primary site parameters, complemented by the Southern California basin model developed by Nweke et al. (2022).

4.2.2 Spatial Variation of Site Terms

Figure 4.2 illustrates the spatial variation of site terms (ηs) across the Los Angeles Basin, computed using the BSSA14-NEA22 GMM for different periods of pseudospectral acceleration (PSA).

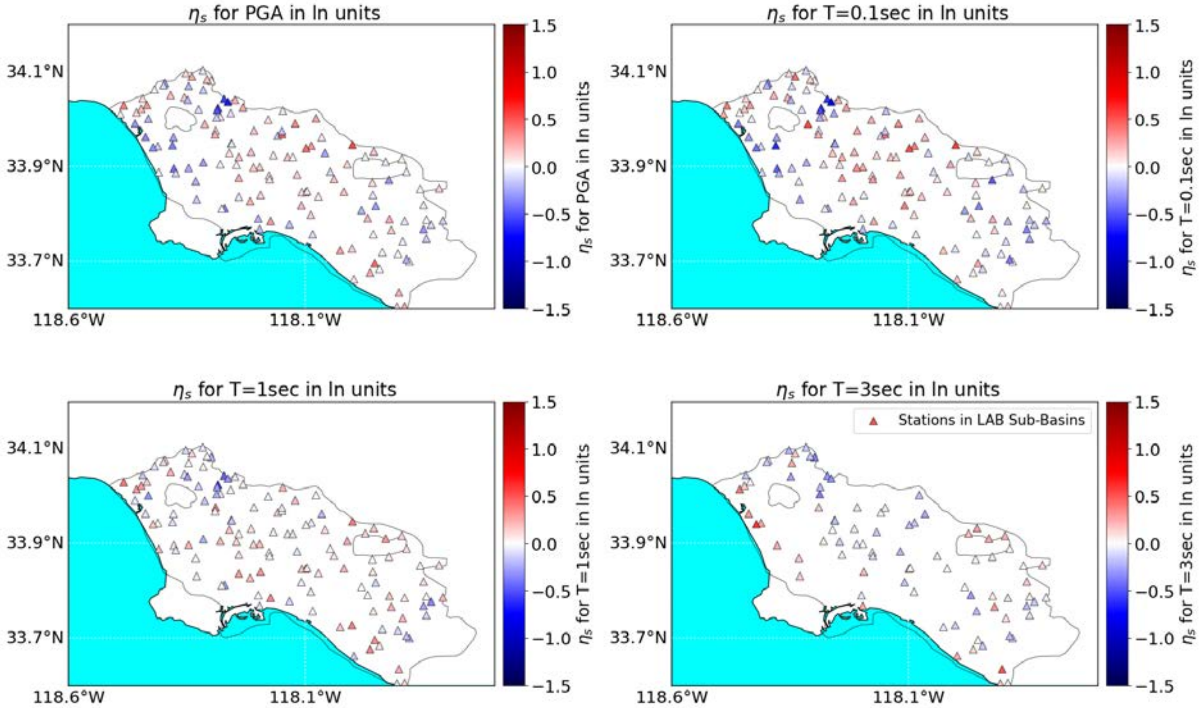

Figure 4.2: Spatial variation of η_S over Los Angeles Basin (LAB) where triangle markers are stations in LAB colored by η_S obtained based on the BSSA14-NEA22 GMM.

This figure reveals significant spatial and period-dependent variability in site response across the basin:

1. Short-Period Response (PGA and T=0.1s): At PGA (top left subplot) and T=0.1 seconds (top right subplot), we observe higher values of site terms (warmer colors) in the northwestern-most portion of the basin, the central part, and the southern portions. This pattern reflects the influence of complex basin geometries that resonate with short-period intensity measures, suggesting that factors beyond V_{S30}, $z_{1.0}$, and basin category may be controlling site response in these areas.
2. Intermediate to Long-Period Response (T=1s and T=3s): As we progress to longer period pseudospectral intensities (T=1 second, bottom left subplot; T=3 seconds, bottom right subplot), there is a notable reduction in high site terms (warmer colors) and an increase in closely-neutral colors (near white) and slight over-predictions (cooler colors) throughout the basin. This shift indicates that the combination of V_{S30}, $z_{1.0}$, and basin categories performs better at longer periods, implying that these parameters are able to somewhat represent the features in the basins that resonate with long-period intensity measures.
3. Basin Margin Effects: Notably, warmer colors persist at the margins of the basin across all periods, particularly evident in the T=1s and T=3s subplots. This suggests that while the current parameters capture much of the long-period basin response, there are still areas for improvement, especially in characterizing site response near basin edges.

These observations highlight the complex, period-dependent nature of site response in the Los Angeles Basin. While current parameters (V_{S30}, $z_{1.0}$, and basin category) capture many aspects of this response, particularly at longer periods, the persistent spatial patterns – especially at short periods and basin margins – indicate that additional factors may be influencing site response.

4.2.3 Performance of V_{S30}, $z_{1.0}$, and Basin Category in Capturing Site Effects

To evaluate the effectiveness of V_{S30}, $z_{1.0}$, and basin category in capturing site effects within the LAB and the broader SoCal region, we examined the trends in site residuals from the BSSA14 GMM under different conditions:

Reference Rock Condition:

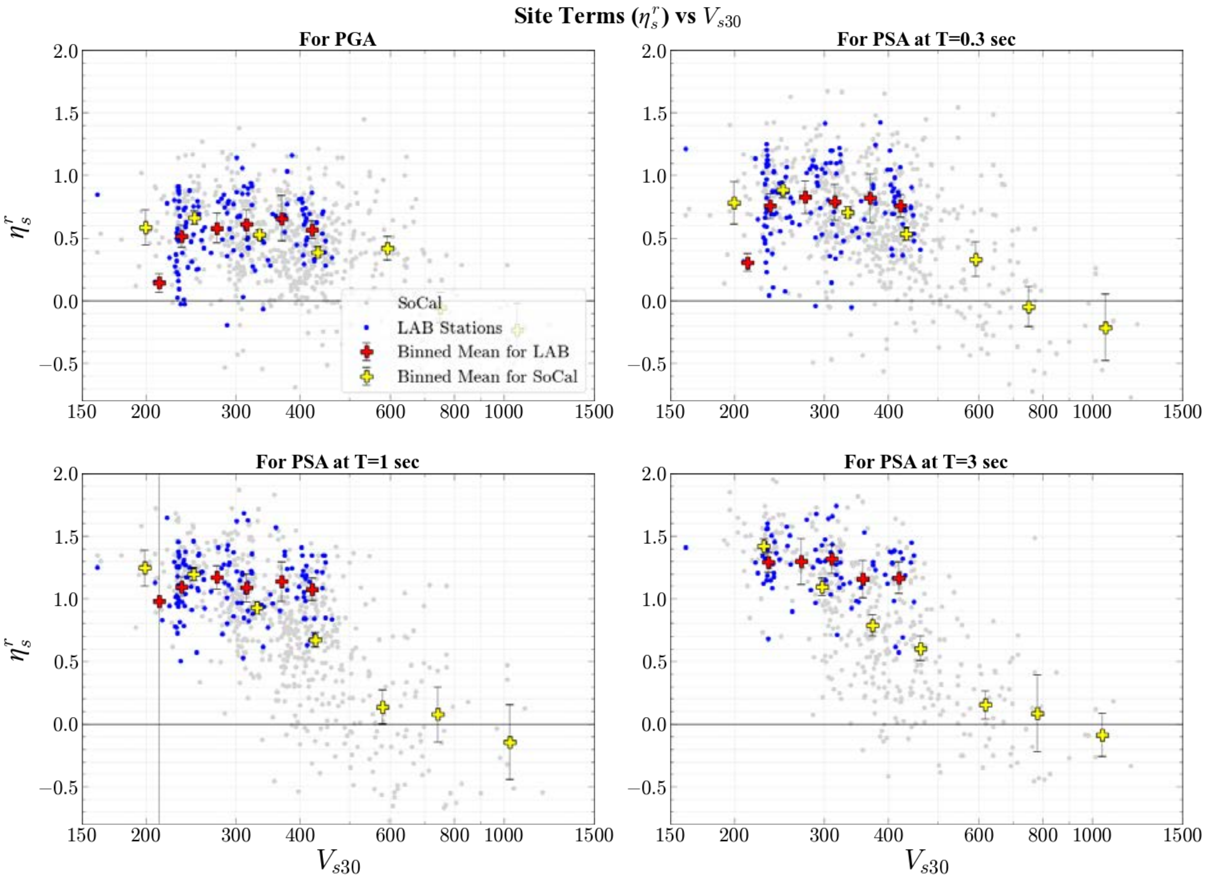

Figure 4.3: Trends of Site Terms (η_{sj}^r) with V_{S30} for sites in LAB and SoCal under reference rock conditions.

Figure 4.3 shows the trends of site terms against V_{S30} when site response is not accounted for in the GMM. The impact of this lack of consideration is evident in the strong trend and shift in residuals toward higher site term values. This pattern is observed for both LAB sites and sites in the greater SoCal region across all periods of intensity, with longer periods showing stronger scaling (steeper slope). The figure clearly demonstrates the significant site effects present when site response is not incorporated into the model.

V_{S30}-Scaled Condition:

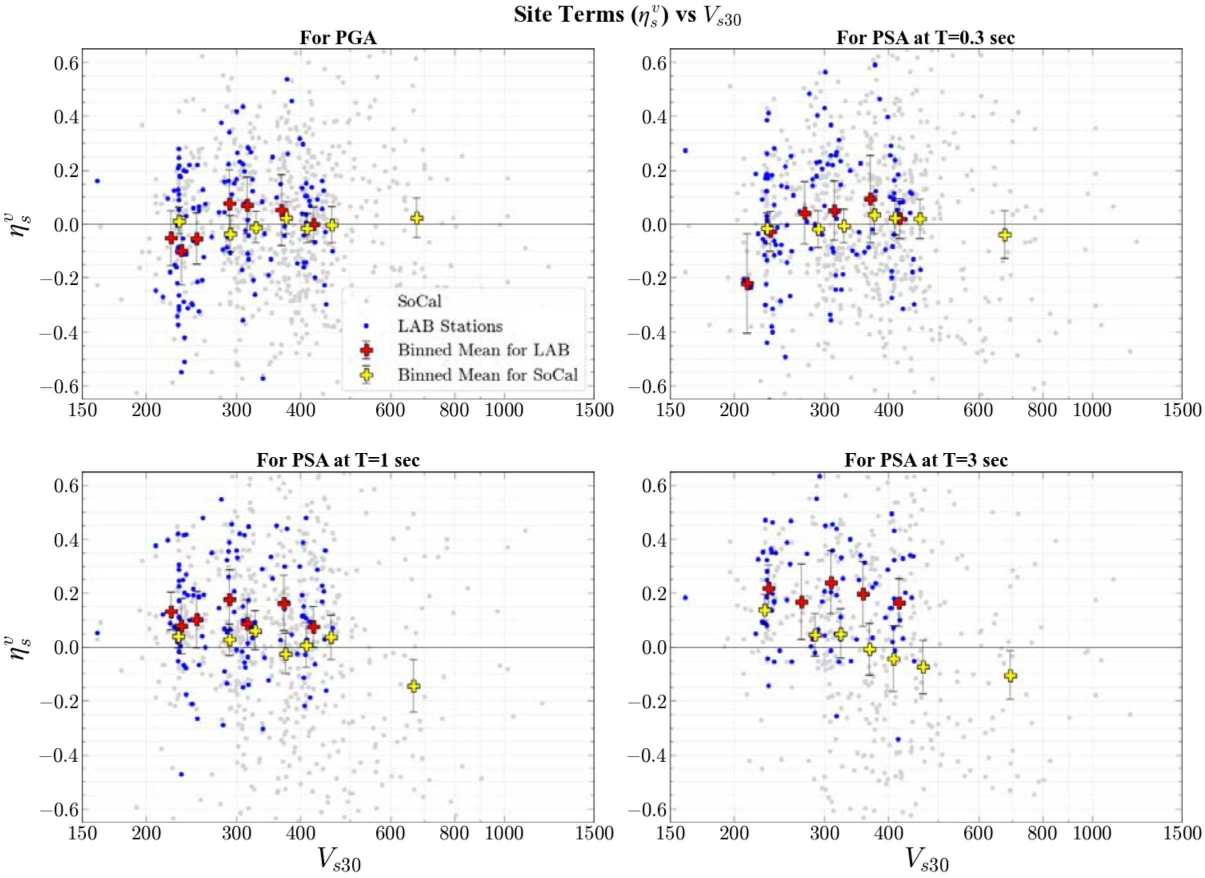

Figure 4.4: Trends of Site Terms (η_{sj}^{v}) with V_{S30} for sites in LAB and SoCal under V_{S30}-scaled conditions.

Figure 4.4 illustrates that the trends observed from the reference conditions have been significantly reduced compared to Figure 4.3, demonstrating the effectiveness of V_{S30} in capturing substantial portions of site response. However, the scatter remains quite large, indicating considerable variability not explained by V_{S30} alone. Notably, while the trends for the greater SoCal region are relatively unbiased, the trends for LAB show appreciable bias, particularly for intermediate to longer periods. This suggests that additional factors beyond V_{S30} may be influencing site response in the Los Angeles Basin.

Full Model Condition:

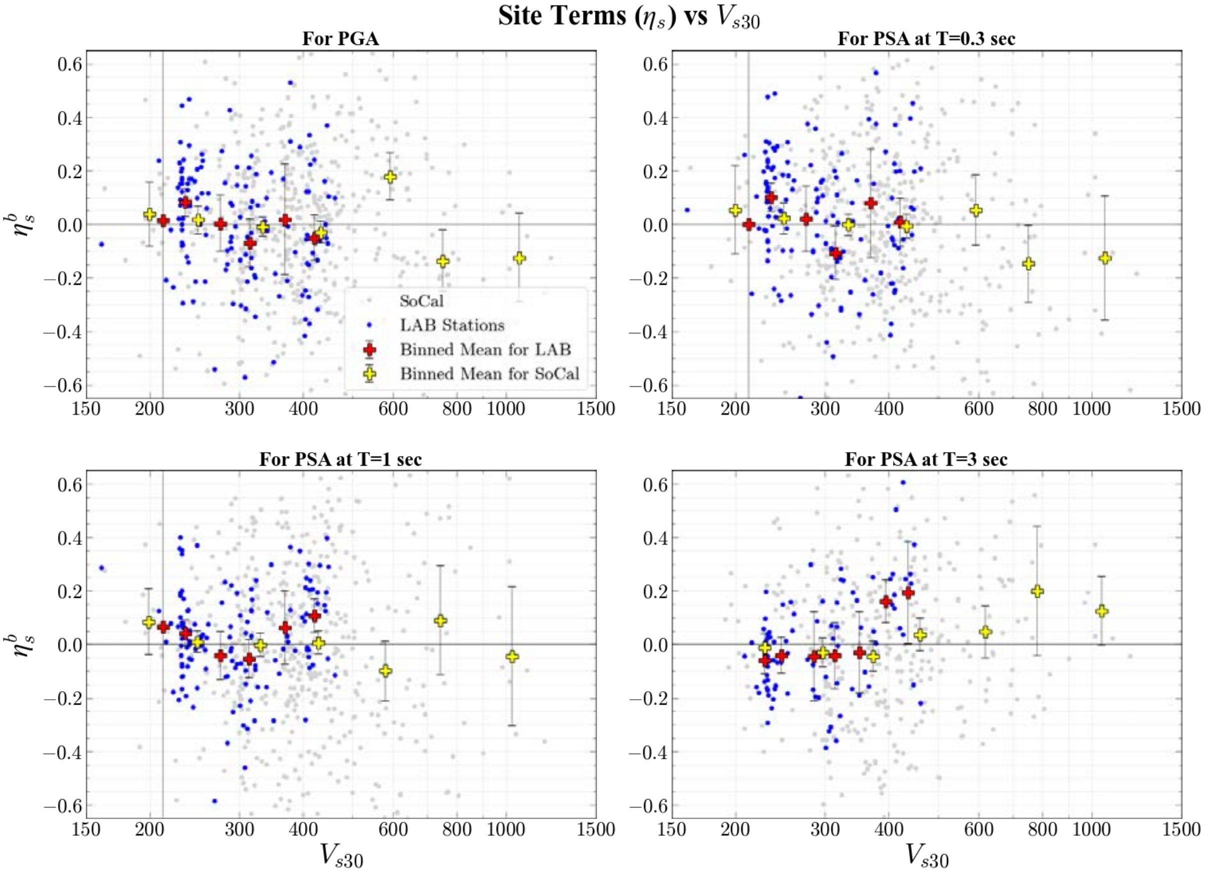

Figure 4.5: Trends of Site Terms (η_{sj}^b) with V_{S30} for sites in LAB and SoCal under full model conditions (V_{S30}, $z_{1.0}$, and basin category).

Figure 4.5 shows improvements in the trends when compared to the V_{S30}-scaled condition in Figure 4.4, particularly for softer sites (lower V_{S30} values). This indicates that the inclusion of $z_{1.0}$ and basin category parameters help to capture additional aspects of site response not accounted for by V_{S30} alone. However, trends still persist for LAB sites (and to some extent for the greater SoCal sites) as we progress to stiffer sites (higher V_{S30} values). Moreover, the dispersion (scatter) remains appreciable, suggesting that there are still unaccounted factors influencing site response, especially in the Los Angeles Basin.

4.2.4 Implications and Need for Additional Parameters

The analysis presented in Figures 13-16 demonstrates that while V_{S30}, $z_{1.0}$, and basin category are effective in capturing many aspects of site response, they do not fully account for all site effects, particularly in the Los Angeles Basin. The remaining trends and substantial scatter in the full model residuals (Figure 13 and 16) indicate that there are basin effects not adequately captured by these current parameters.

These observations motivate our exploration of additional geometric parameters that could complement V_{S30}, $z_{1.0}$, and basin category in characterizing site response. By developing parameters that can capture 2D and 3D basin effects, we aim to reduce the remaining biases and improve the accuracy of site response predictions in complex basin environments like the Los Angeles Basin.

In the following chapters, we will introduce and evaluate a suite of geometric parameters designed to address these limitations and enhance our ability to model site response in sedimentary basins.

Chapter 5: Sedimentary Basin Shape for Los Angeles Basin (LAB)

5.1 Overview

Defining the shape and depth constraints of the Los Angeles Basin (LAB) is crucial for developing effective geometric parameters to characterize site response. This chapter explores various methods and data sources used to map and constrain the basin's geometry, with a particular focus on determining the depth to the sedimentary basement (layer of stiffest sedimentary rock) and crystalline basement. Our goal is to establish a robust framework for the derivation of geometric parameters that will be used in subsequent analysis of basin effects and site response modeling.

5.2 Basin Boundary Definition

A distinct definition of the Los Angeles Basin (LAB) boundary is a crucial first step in developing geometric parameters for site response analysis because a well-defined boundary serves as a reference necessary for deriving geometric features and establishes the extents of what is considered a basin site. This delineation is essential for accurately characterizing the seismic response within the basin context. Nweke et al. (2022) initially developed a basin boundary for the LAB based on several considerations:

1. Topographic relief: They primarily used mountain ranges and other non-basin features as constraints for the basin edges.
2. Geological constraints: Major faults were considered where they aligned with significant changes in basin/topographic characteristics.
3. Previous studies: They considered basin delineations from earlier research, synthesizing this information with newer data.

However, their approach had some limitations. First, the gradual transitions in basin properties (i.e., gradient of iso-surface depths) did not always align with the sharp boundaries typically assumed. Additionally, there was limited data available in certain areas, particularly near the basin edges. Lastly, reconciling the surface geology with the deep basin structure proved challenging, further complicating the analysis. In this study, we made subtle updates to the northern boundary established by Nweke et al. (2022). Specifically, we moved the northern part of the basin boundary southward to align more closely with the Santa Monica fault system (instead of the estimated topographic relief that occurs closer to the foothills). This adjustment was made based on updated findings about the depth of sediments on either side of the fault (Catchings et al. 2008), which necessitated a revision to adhere to established data and geologic knowledge. This refinement allows for a more accurate representation of the basin's structural limits in this area. Figure 5.1 illustrates the revised LAB outline along with quaternary faults.

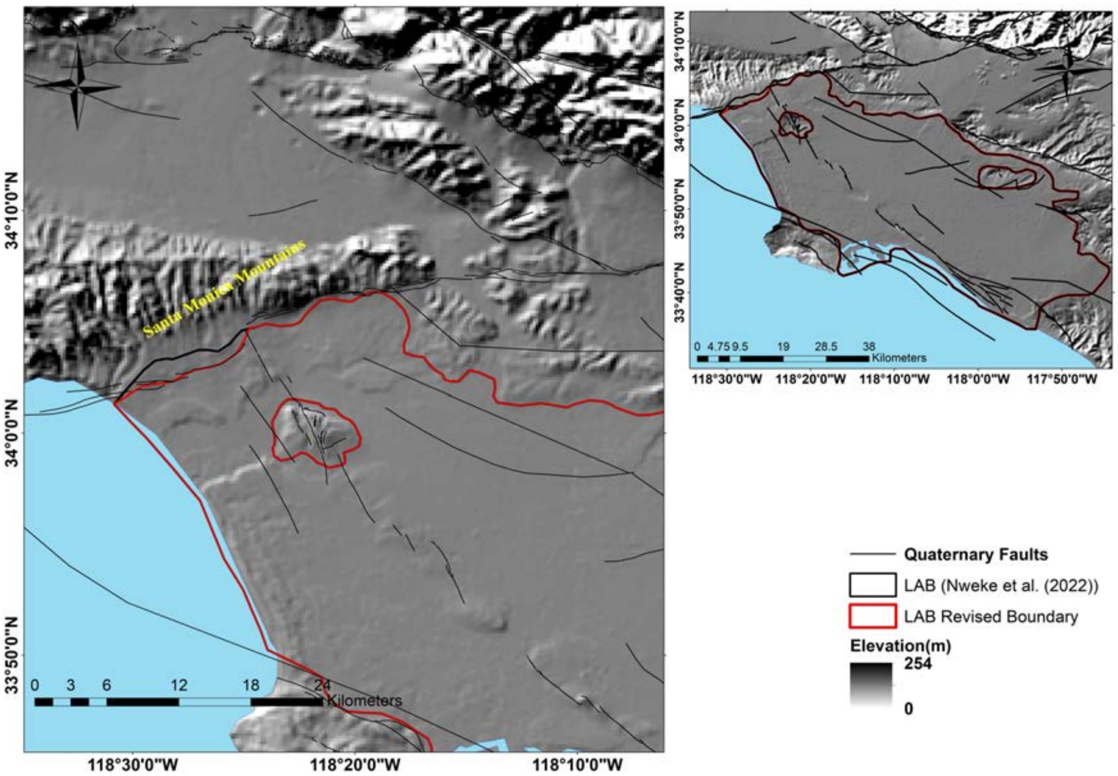

Figure 5.1: Revised LAB outline modified after Nweke et al. (2022) where black lines show quaternary faults and red boundary represents revised basin boundary.

It's important to note that the western boundary, which appears to terminate at the Pacific Ocean coastline, does not represent a true geological boundary of the basin. In reality, the LAB extends westward into the ocean. The boundary we've defined here represents the extent of engineering concern for onshore infrastructure and the practical limit of our analysis given available data. This artificial western boundary is a necessary simplification for our study but should be considered when interpreting results, particularly for coastal areas. Overall, the refined basin boundary provides a more accurate reference frame for developing geometric parameters. It allows for a better representation of the basin's structural characteristics and their potential influence on seismic wave propagation, particularly in the northern part of the basin where the adjustment was made. In the following sections, we'll use this updated boundary as the basis for exploring the configuration of basin's internal structure.

5.3 Depth to Crystalline Basement Rock

The depth to crystalline basement (z_{cb}) represents the thickness of sedimentary deposits (soil and soft rock) overlying the crystalline rock that forms the foundation of the basin (Shaw et al., 2015). This parameter is crucial for understanding basin geometry and its influence on seismic wave propagation, as the impedance contrast between sediments and crystalline rock significantly affects site response (Graves et al., 1998).

Direct measurements of z_{cb} are scarce, primarily limited to oil exploration data. As a result, we rely on modeled estimates of crystalline basement depth. Shaw et al. (2015) developed z_{cb} as a triangulated surface using mostly gravity data, which served as a part of the foundation for the Community Velocity Model for Southern California (CVM-H v15.1). This model integrates various data sources, including seismic reflection and refraction surveys, gravity data, well logs, and tomographic studies, to create a comprehensive 3D representation of the basin contents and structure. While the CVM-H model represents the best available estimate of z_{cb}, it is important to acknowledge its limitations. The model's reliance on gravity data, a potential field method, introduces inherent resolution constraints, resulting in a smoothed representation of the basement surface that may not capture small-scale features. The non-unique nature of gravity data interpretations means that different density distributions can produce similar gravity signatures, leading to uncertainties in basement depth estimates, particularly in areas with complex geology. Additionally, the accuracy of these estimates decreases with depth due to the attenuation of gravity signals. The model's interpretation is also based on assumptions about density contrasts between the basement and overlying sediments, and variations in these contrasts can affect the accuracy of depth estimates. Lastly, the model's accuracy may vary across the region depending on the density and quality of available gravity measurements. These limitations underscore the need for cautious application of the CVM-H z_{cb} estimates, especially in areas of complex geology or deep basins. However, given that this is primary resource it will serve as the current "best estimate". Figure 5.2 illustrates the spatial variation of z_{cb} across the Los Angeles Basin derived from CVM-H. The central part of the LAB forms the deepest portion of the basin, with z_{cb} reaching over 8 km in some areas. This deep central trough is surrounded by shallower regions, particularly towards the basin edges, providing a clear visualization of the basin's complex 3D structure.

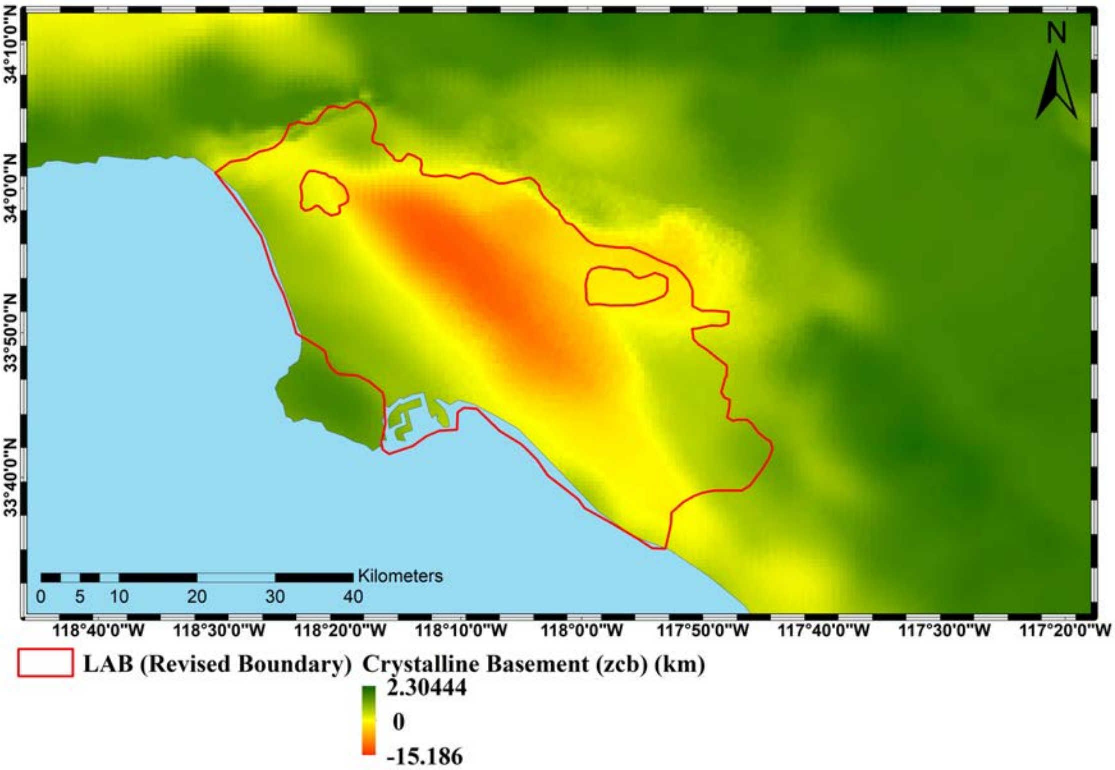

Figure 5.2: Spatial variation of z_{cb} (km) over LAB where red colour shows deeper portions and lighter colour shows shallower parts of the basin.

We explored the potential correlation between z_{cb} and V_{S30}, motivated by the findings of Day et al. (2008) who established a signification correlation between basin (iso-surface depths) and V_{S30}. This relationship has since been incorporated into many current ground motion models (i.e., Chiou and Youngs 2014 and their existing relationship between $z_{1.0}$ and V_{S30} and the updates by Nweke et al. 2022). Since both $z_{1.0}$ and z_{cb} are derived from velocity models, we hypothesized that they might share similar associations with V_{S30}. This assessment was aimed at understanding whether z_{cb} could provide additional or complementary information to $z_{1.0}$ in characterizing site response. Figures 5.3 and 5.4 illustrate our findings regarding the relationship.

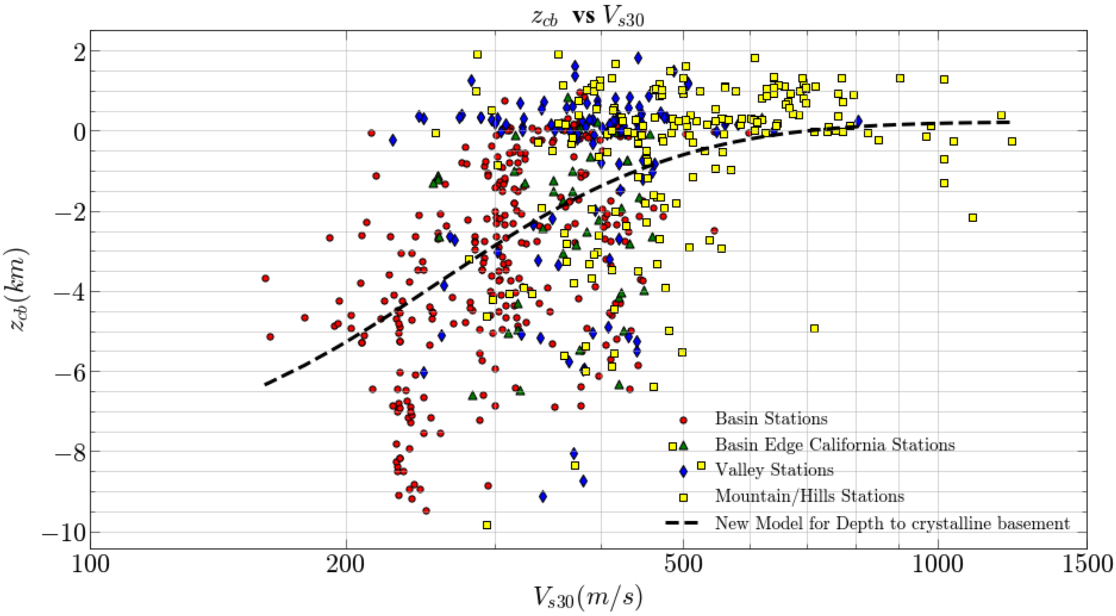

Figure 5.3: z_{cb} for SoCal sites coloured based on their geomorphic province with V_{S30} (m/s). The black dashed line is the best fit based on functional form in Nweke et al. (2022).

Figure 5.3 shows the distribution of z_{cb} values against V_{S30} for different geomorphic provinces in Southern California. The color-coding helps visualize how the relationship varies across different geological settings.

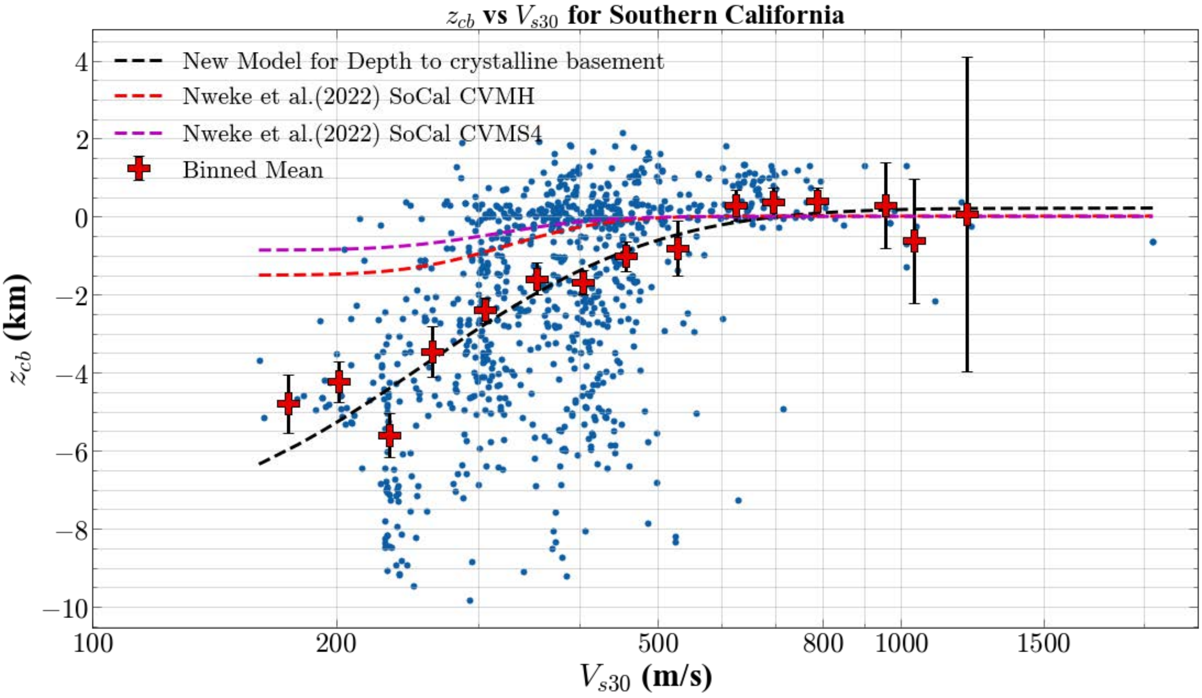

Figure 5.4: Mean depth model between z_{cb} and V_{S30} by adopting a similar function form adopted by Nweke et al. (2022). The red markers are the binned means for the data and the black dashed line is the best fit. *Note: Nweke et al. (2022) trends are not referenced to elevation but to a "squashed" velocity model reference point.*

Figure 5.4 focuses on the mean trend of the z_{cb}-V_{S30} relationship via the binned means (red markers), and how a best-fit curve (black dashed line) compares to the Nweke et al. (2022) update for Southern California. The z_{cb} curve can be described by the following equation:

$$z_{cb} = a\left[1 + erf\left(\frac{ln(V_{S30}) - ln(b)}{c\sqrt{2}}\right)\right] + d \tag{5}$$

Where a = -4.03759191, b = 256.488634, c = -0.526637759, and d = 0.220761861

The similarity between the z_{cb}-V_{S30} relationship and the $z_{1.0}$-V_{S30} relationship established by Nweke et al. (2022) for Southern California suggests that z_{cb} and $z_{1.0}$ provide similar site response predictive capabilities. However, this similarity also indicates that z_{cb} cannot be directly used to model site response in GMMs as if offers no new information related to the site response. This is in addition to the issues of multicollinearity (as discussed in Nweke et al. 2022). Figure 21a&b supports this claim through the lack of trends observed in the z_{cb}-η_s and δz_{cb}-η_s plots of Figure 5.5(a) and 5.5(b).

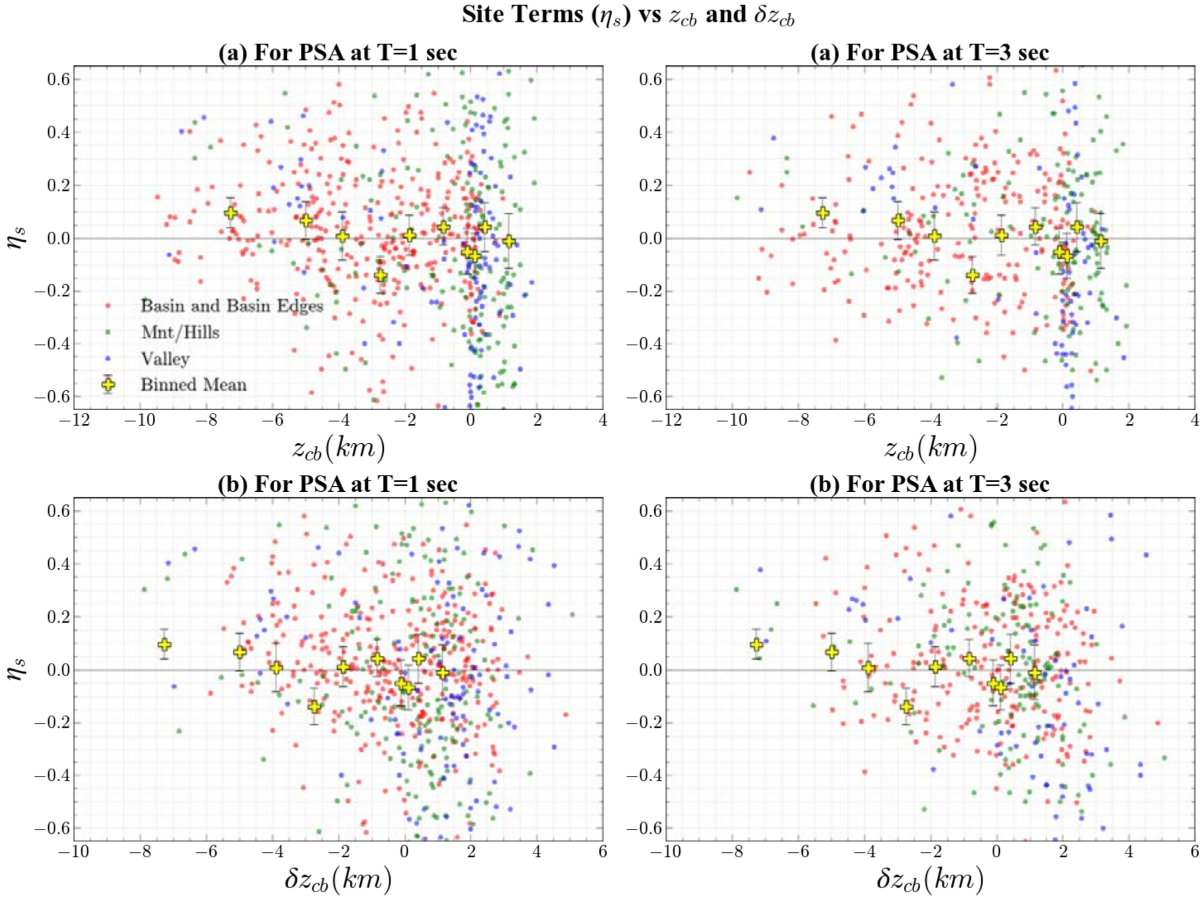

Figure 5.5: For both T = 1 & 3 seconds; (a) Shows η_s with z_{cb} for sites in SoCal. Yellow markers show binned means for basin and non-basin sites. (b) Shows the η_s with δz_{cb} for sites in SoCal

This lack of trend between the site terms (η_s) and z_{cb} or δz_{cb} is shown by the clustering of the binned means (yellow markers) around zero. This suggests that z_{cb} (or δz_{cb}) provides no significant improvement over current parameters (V_{S30} and $z_{1.0}$) in predicting site response, further supporting the decision not to directly incorporate z_{cb} as a geometric parameter update in the ground motion models. These findings underscore the need for alternative parameters that can provide unique information about basin structure and its influence on site response. In the following section, we investigate efficacy of a depth parameter relative to the stiffest sedimentary rock horizons rather than the crystalline basement rock interface.

5.4 Depth to Stiffest Sedimentary Rock

The depth to the stiffest sedimentary rock is important because it potentially represents a key impedance contrast that can significantly influence ground motion as seismic waves travel from the source to the site. While the interface between crystalline rock and overlying sediments (or sedimentary rock) is often assumed to be the critical boundary, this transition may sometimes be more gradual, reducing its impact on seismic response. In such cases, the more crucial impedance contrast may occur higher in the sequence, between the stiffest sedimentary rock and a less stiff sedimentary formation. This shift in the key interface could play a larger role in controlling how seismic waves are amplified or attenuated as they pass through, and into, the basin.

To better identify this influential boundary, we use a comparative approach that integrates geological cross-sections with velocity model profiles. This method allows us to align geological formations with velocity structures, pinpoint significant impedance contrasts, and develop a clearer understanding of how the basin's internal structure affects seismic wave propagation. Figure 5.6 illustrates the locations of various cross-sections analyzed across the Los Angeles Basin.

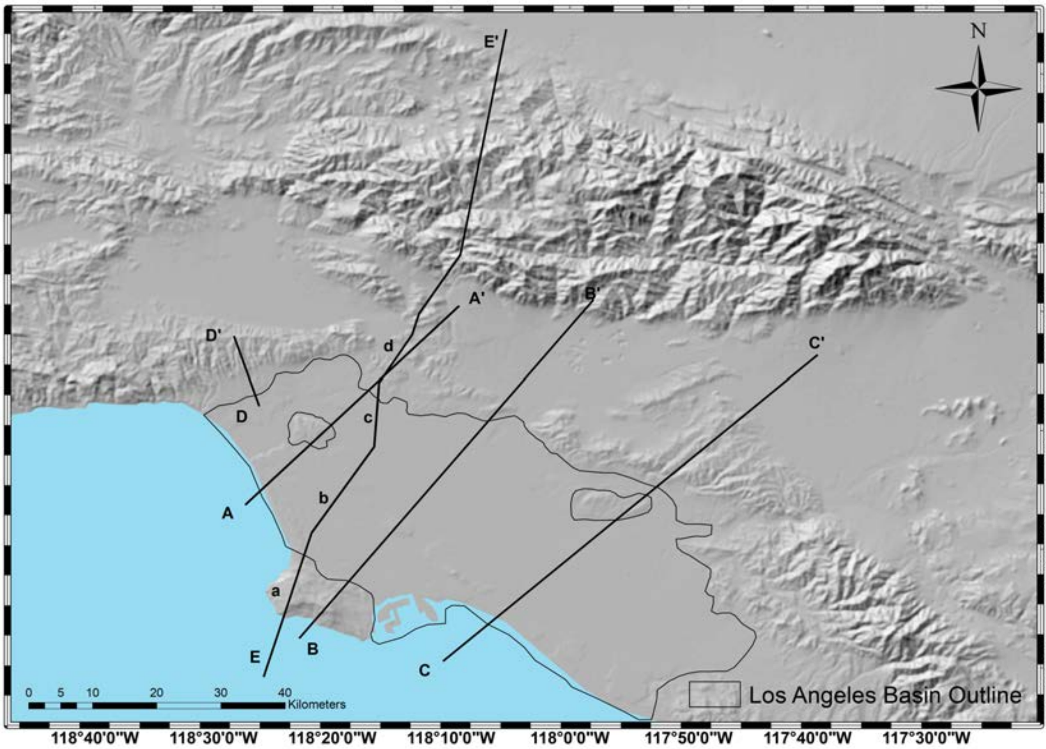

Figure 5.6: Map showing different cross-section locations studied in the LAB.

Figures 5.7 compares a geologic profile from Beyer (1988) with velocity profiles derived from CVM-H (Shaw et al. 2015) for cross section A-A’, which spans a distance of 40 km and traverses major locations like the Los Angeles International Airport, Baldwin Hills, Elysian Heights, and the Rose Bowl. The vertical axis of the geologic profile is in thousands of feet, while the velocity profile is in meters. The black line in the velocity profile represents the depth at which crystalline basement rock is encountered which falls within shear wave velocity range of approximately 2.0 – 3.5 km/s. Visually, this crystalline basement depth shows good agreement with the depth at which the Catalina Schist (basement complex rocks) are identified in the geologic profiles. This instils confidence that the z_{cb} from the CVMM-H model is an adequate estimate, but it also shows, via the range of velocity values, that the governing impedance contrast may correspond with boundaries higher in the depositional sequence.

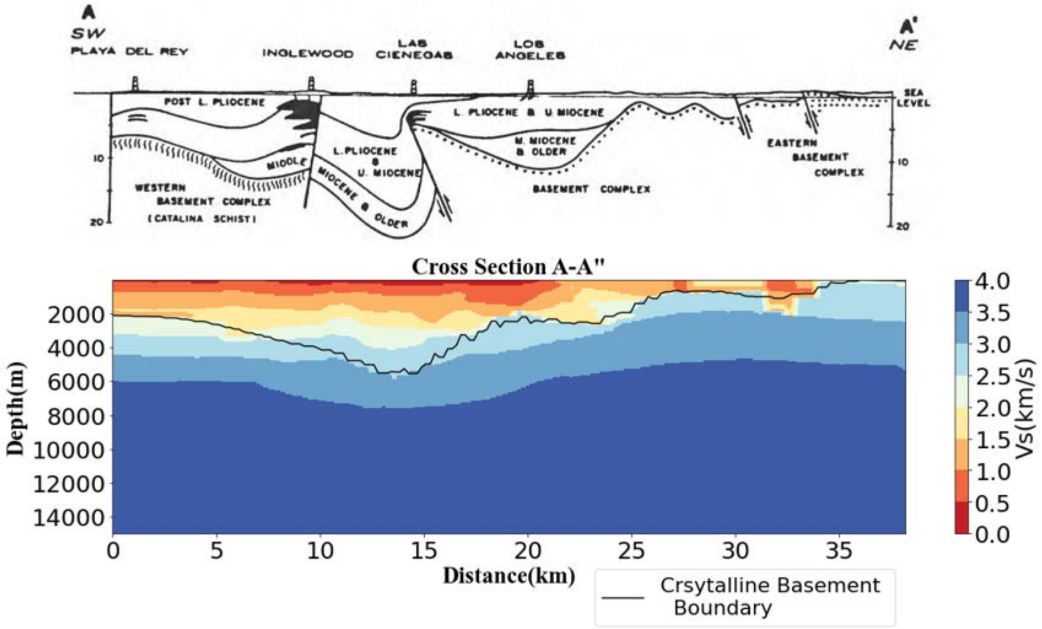

Figure 5.7: Comparison of geologic profile and velocity model profile for cross-section A-A’

Figure 5.8 compares a geologic profile from Beyer (1988) with velocity profiles derived from CVM-H for cross section B-B’, which spans a distance of 63 km and traverses major geologic features like the Palos Verdes peninsula, City of Compton and South Gate (center of the LAB), and the foothills of the San Gabriel Mountains. Similar to cross section A-A’, the velocity range of z_{cb} is similar for B-B’ and the location of the crystalline basement rocks shows good agreement between the geologic profile and CVM-H.

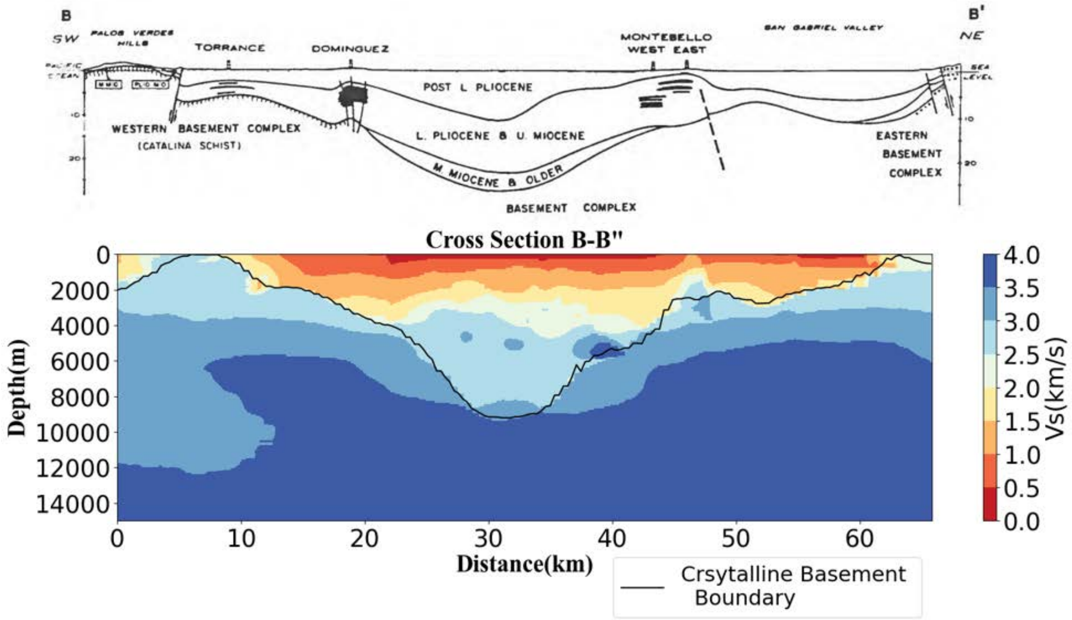

Figure 5.8: Comparison of geologic profile and velocity model profile for cross-section B-B’

Figure 5.9 compares a geologic profile from Beyer (1988) with velocity profiles derived from CVM-H for cross section C-C’, which spans a distance of approximately 70 km and traverses

Long Beach/Seal Beach, Brea Hills, Chino Hills, and the City of Ontario. Similar agreements as with the prior two cross sections are observed, along with some capture of fault discontinuity features, though the resolution is relatively poor.

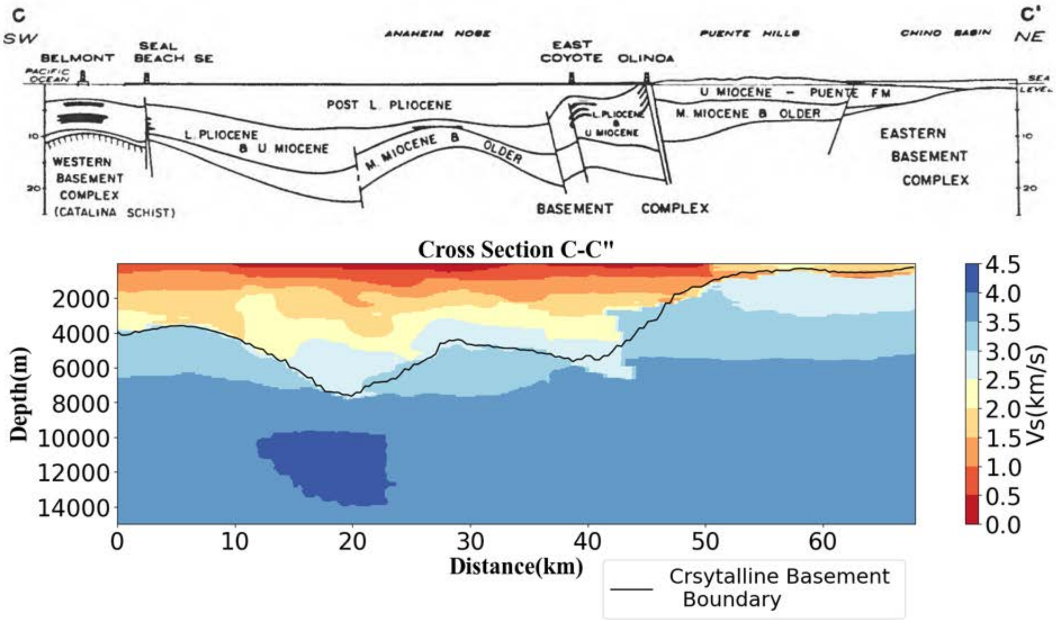

Figure 5.9: Comparison of geologic profile and velocity model profile for cross-section C-C’

Figure 5.10 compares a geologic profile from (Wright, 1987) with velocity profiles derived from CVM-H for cross section D-D’, which spans a distance of approximately 12 km and traverses the Santa Monica Fault and a section of the Santa Monica Mountains. The location of the crystalline basement depth is very roughly in agreement, but the description of the boundary shows a strong mismatch. The velocity model does not capture the “step” features induced by the Santa Monica fault which has been shown to significantly control site response in this area (Graves et al. 1998; Davis et al. 2000). This observation highlights a limitation of the velocity models and their representation of subsurface features, particularly, at shallower portions/locations (i.e., basin edges).

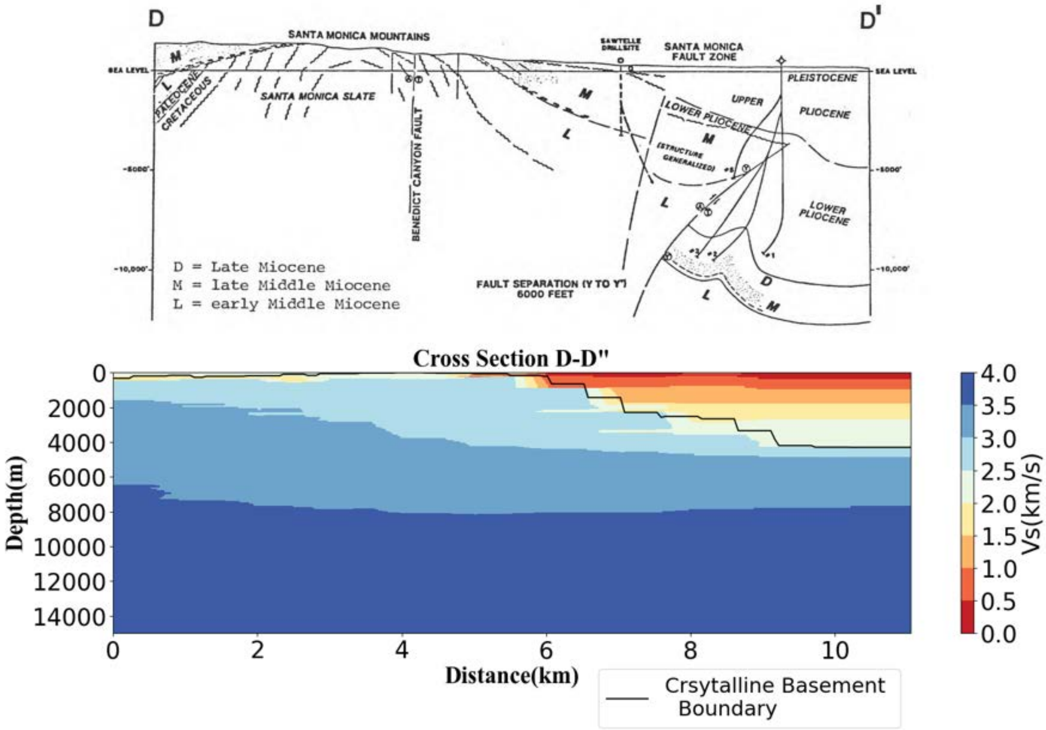

Figure 5.10: Comparison of geologic profile and velocity model profile for cross-section D-D'

Figure 5.11 compares a more recent geologic profile from Davis and Namson (1998) with velocity profiles derived from CVM-H for cross section E-E', which spans approximately 105 km and traverses' locations like thee Palos Verdes peninsula, Downtown Los Angeles, the San Gabriel Mountain and Sierra Madre Fault zone, the San Andreas Fault, and the City of Palmdale. The location of the crystalline basement rock depth is in good agreement and is now shown to align with the boundary between Fernando Formation (Tfl) and Puente Formation (Tp). A complete comparison of Figure 5.12 with the prior figures (Figure 5.7-5.10) led to the decision to adopt the boundary between the Fernando Formation and Puente Formation (Tfl-Tp) as the location of the stiffest sedimentary rock layer. This sediment rock boundary often aligns with significant seismic velocity changes, suggesting it may represent an important impedance contrast for site response. From the figures it corresponds to a velocity horizon of 1.5km/s and 2.3 km/s, which in depth terms is $z_{1.5}$ and $z_{2.3}$, respectively. These are the two values that could serve as a depth to stiffest sedimentary rock layers, z_{sb} and will be explored further in the subsequent chapter. Figures 5.12 and 5.13 show the spatial distribution of both z_{sb} for the Los Angeles Basin.

The results of this chapter are the establishment of the LAB basin shape via surface and subsurface (z_{cb}, z_{sb}) boundaries. This provides a solid foundation for developing geometric parameters that can capture the complex 3D structure of the LAB and its influence on seismic site response. In the next chapter, we will use this structural framework to explore and develop specific geometric parameters aimed at improving site response predictions in the Los Angeles Basin.

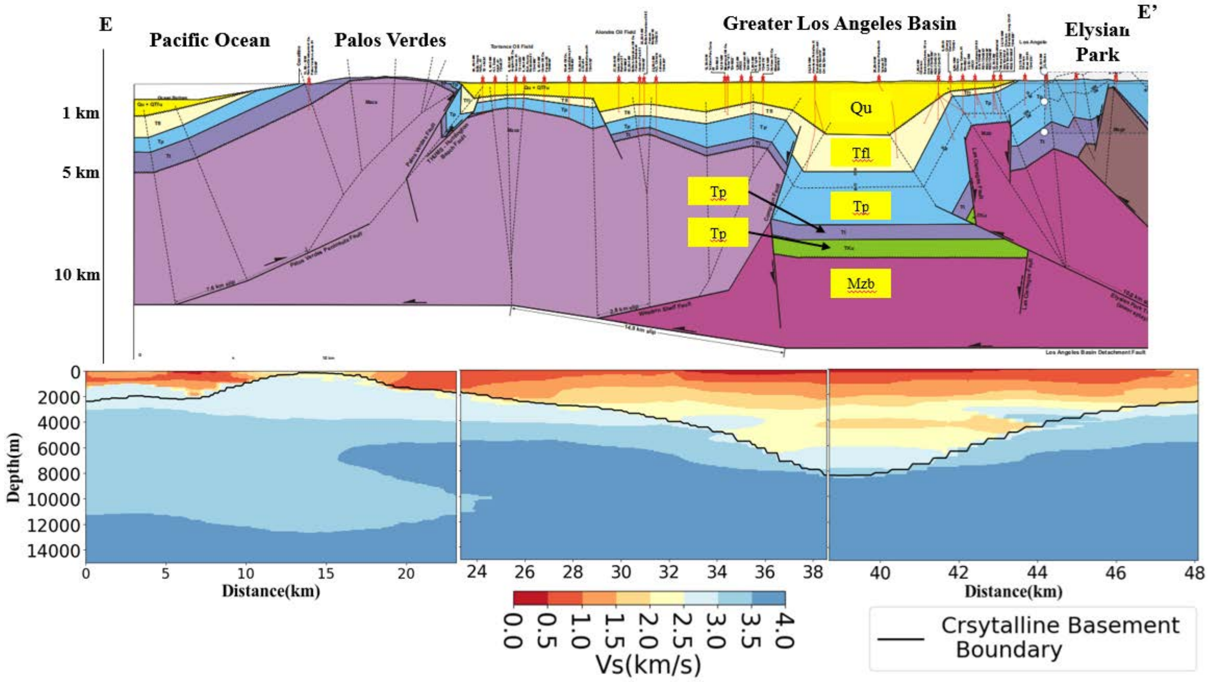

Figure 5.11: Comparison of geological cross section (E-E') from Davis and Namson (1998) with CVM-H velocity profile.

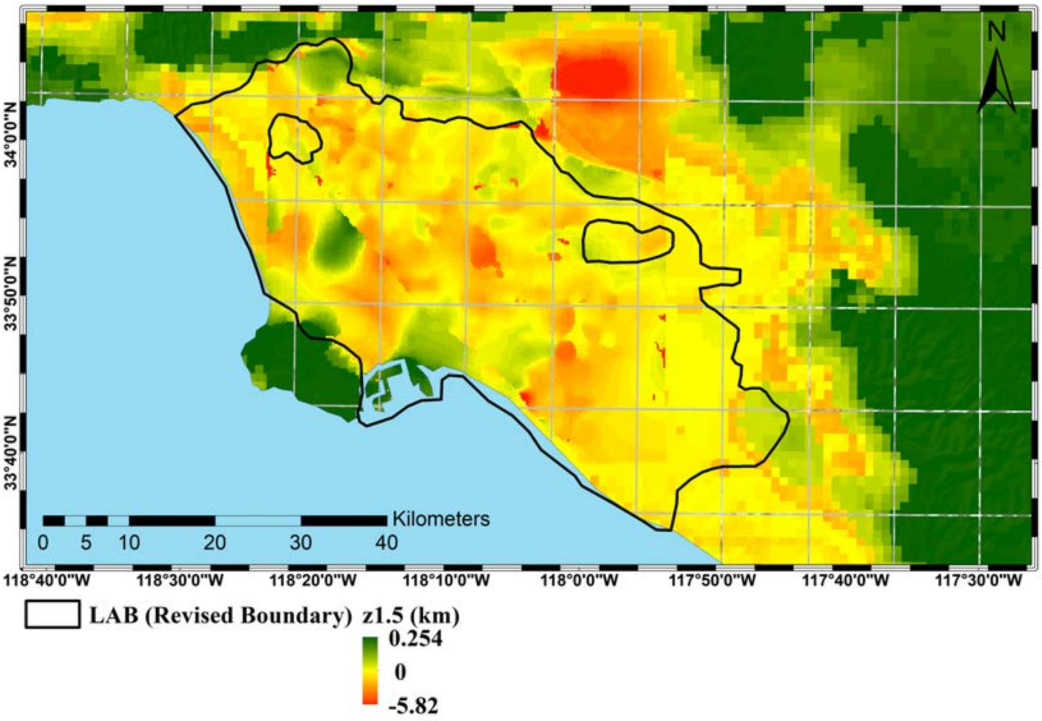

Figure 5.12: Map shows depth at Vs=1.5km/s surface from CVMH (Shaw et al. 2015) where black boundary represents LAB outline.

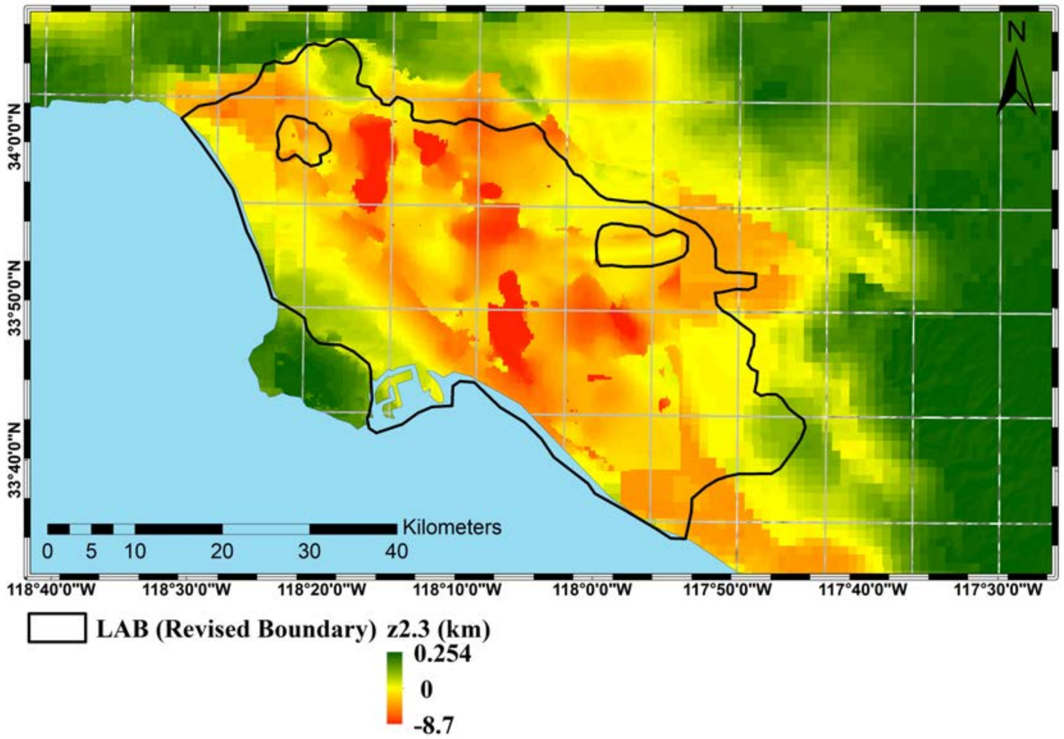

Figure 5.13: Map shows depth at Vs=2.3.km/s surface from CVMH (Shaw et al. 2015) where black boundary represents LAB outline.

Chapter 6: Geometric Parameters for Sedimentary Basins

6.1 Overview of Geometric Parameters

The complex three-dimensional structure of sedimentary basins plays a crucial role in modifying seismic waves, leading to significant variations in ground motion amplitudes and durations. While conventional site parameters such as V_{S30}, basin depth ($z_{1.0}$ or $z_{2.5}$), and basin category have been effective in capturing many aspects of site response, they are fundamentally one-dimensional and may not fully account for the three-dimensional effects within basins. This study explores a suite of geometric parameters designed to complement these conventional measures and capture more nuanced aspects of basin geometry that influence seismic wave propagation. These parameters have been selected based on their potential to represent various physical phenomena that affect site response, such as wave focusing (Gao et al. 1996), basin-edge generated surface waves, and resonance effects. The geometric parameters investigated in this study are categorized and summarized in the following table:

Table 1: Geometric Parameters explored for Los Angeles Basin (LAB)

Category	Parameter	Description
Depth-related	Depth to Crystalline Basement (z_{cb})	Depth to the interface between sedimentary and crystalline rock
	Standard Deviation of z_{cb} (SD_{zcb})	Measure of variability in crystalline basement depth
	Standard Deviation of Absolute Difference between $z_{1.5}$ and z_{cb}	Captures variability in sediment thickness
Distance-based	Distance from Basin Margin (R^b_{mar})	Distance from the edge of the basin
	Distance from Basin Centroid (C_b)	Distance from the center of the basin
	Distance from Steepest Basin-Bedrock Contact (R^b_{bbc})	Distance from areas of rapid change in basement depth
	Closest Distance from River (R_r)	Proximity to major river channels
	Closest Distance from a seismic discontinuity/fault (R_f)	Proximity to major faults
Surface and near surface (2D) related	Surface Texture (S_{t2500})	Measure of surface roughness and variability
	Spatial Area of Influence based on V_S slope (SAI_{VS})	Captures lateral variations in velocity profile structure
	Spatial Area of Influence based on Standard Deviation of V_{S30} (SAI_{VS30})	Represents variability in near-surface velocities over a range of space
Basin shape	Basin Eccentricity	Measure of basin elongation
	Slope of Basin (θ_b)	Gradient of the basin floor
	Aspect of z_{cb}	Orientation of the basin-bedrock interface slope

Each of these parameters is designed to capture specific aspects of basin geometry that may influence seismic wave propagation and site response. For instance, the standard deviation of z_{cb} aims to quantify the variability in basement depth, which could be indicative of focusing effects, while the distance from basin margin parameter is intended to capture basin-edge effects that occur as a result of "body" wave conversions to propagating surface waves. However, it is important to note that the derivation of these parameters relies on the availability and accuracy of underlying geological and geophysical data. As such, the applicability and effectiveness of these parameters may vary depending on the quality and resolution of available data for a given basin.

In the following sections, we will discuss each parameter in detail, including its physical basis, method of calculation, and potential implications for site response. We will also evaluate the performance of these parameters in capturing site effects not accounted for by conventional measures, with the ultimate goal of improving ground motion predictions in complex basin environments. This comprehensive approach allows us to systematically assess which geometric features of sedimentary basins are most influential in controlling site response, potentially leading to more accurate and physically based site amplification models.

6.2 Standard Deviation of z_{cb} (SD_{zcb})

The Standard Deviation of depth to crystalline basement (SD_{zcb}) is a geometric parameter designed to capture the lateral variability in basin depth, aiming to represent aspects of basin geometry that may influence seismic wave propagation and site response. This parameter potentially complements conventional one-dimensional parameters like Vs30 and z1.0 by accounting for lateral variations in basin structure. We compute SD_{zcb} using the Focal Statistics tool in ArcGIS, calculating the standard deviation of z_{cb} values within a circular moving window with a 2500 m radius for each point in the basin. This approach allows us to quantify local variations in basin depth, potentially indicating areas of complex subsurface structure. The variability in basement depth, as captured by SD_{zcb}, could influence seismic wave propagation in several ways. Areas with high SD_{zcb} may indicate rapid changes in basin depth, potentially leading to seismic wave focusing or defocusing effects. Sharp transitions in basin depth, resulting in high SD_{zcb} values, can contribute to the generation of surface waves at basin edges. Additionally, variability in basement depth can create intricate patterns of impedance contrasts, affecting wave propagation and amplification. By capturing these complex 3D effects, SD_{zcb} may provide insights into basin behavior not fully represented by existing parameters, potentially improving our understanding and prediction of site response in basin environments.

The spatial distribution of SD_{zcb} across the Los Angeles Basin, as illustrated in Figure 6.1, reveals several important patterns that provide insights into the basin's structural complexity. This figure, which shows the standard deviation of z_{cb} along with the basin outline and quaternary faults, highlights the relationship between SD_{zcb} and key geological features. Notably, higher SD_{zcb} values frequently align with known fault systems and basin edges, suggesting that this parameter effectively captures important geological discontinuities and the expected complexity in these transitional zones. In contrast, the central parts of the basin generally exhibit lower SD_{zcb} values, indicating a more uniform basement depth in these areas. These observations support the potential of SD_{zcb} as a parameter for quantifying local structural variability within the basin, particularly in areas of geological complexity that may significantly influence seismic wave propagation and site response.

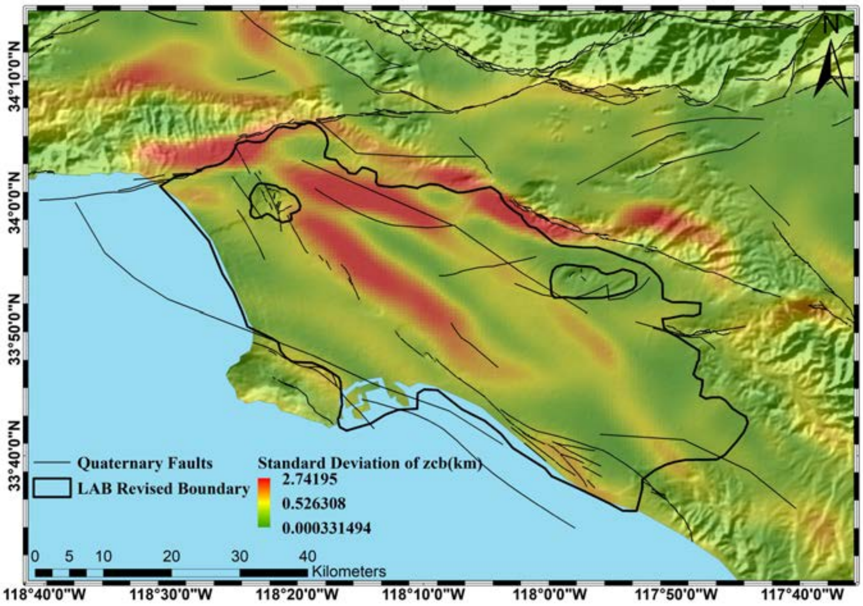

Figure 6.1: Standard deviation of z_{cb} (SD_{zcb}) along with basin outline for LAB (revised after Nweke et al. 2022) and quaternary faults.

To evaluate the effectiveness of SD_{zcb} in capturing site response characteristics, we investigated its relationship with site terms derived from our residual analysis as discussed in Chapter 3. We examined three different site terms:

1. η_s^r: Reference site conditions, which do not include any conventional site parameter features (i.e., V_{S30} = 760 m/s; Figure 6.2).

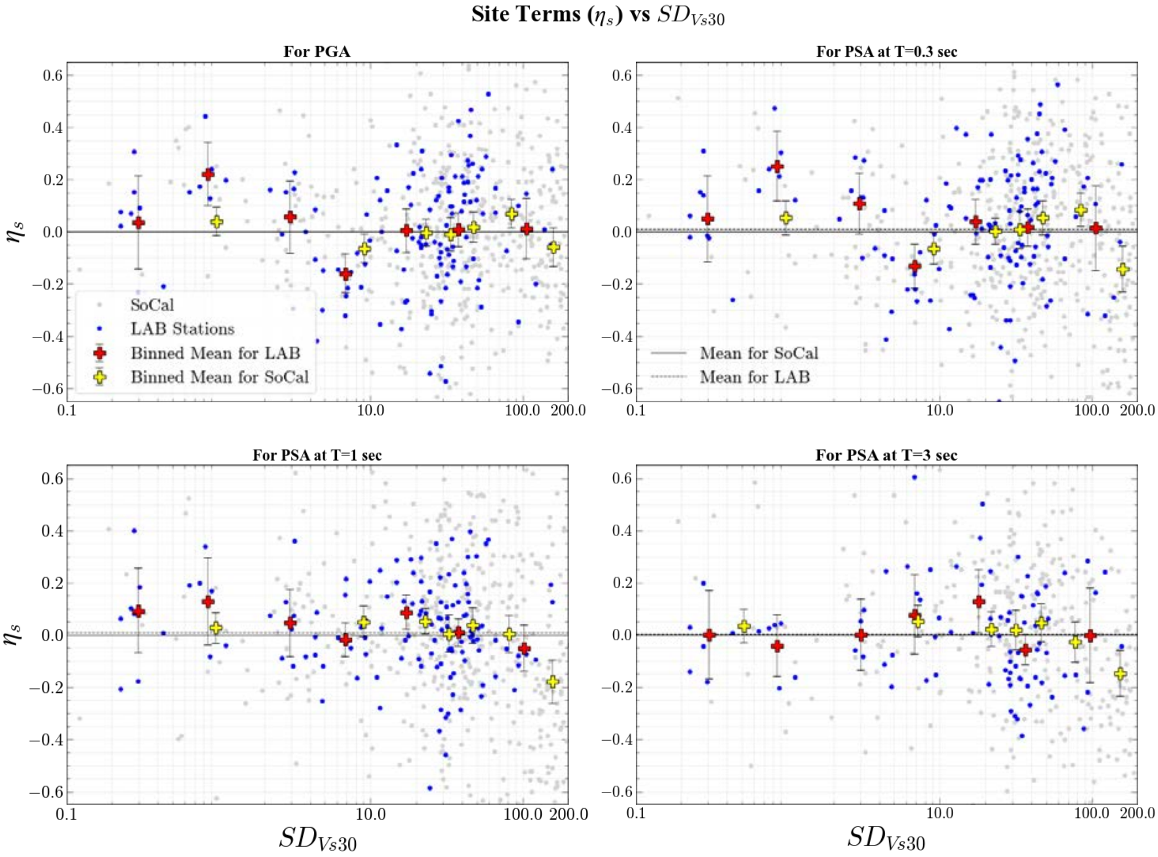

Figure 6.2: Reference Site Residuals η_s^r plotted against SD_{zcb} for LAB sites at different periods. Yellow markers show binned means.

2. η_s^v: V_{S30}-adjusted description, which includes only the V_{S30} scaling portion of the site response (i.e., using the site-specific V_{S30}; Figure 6.3).

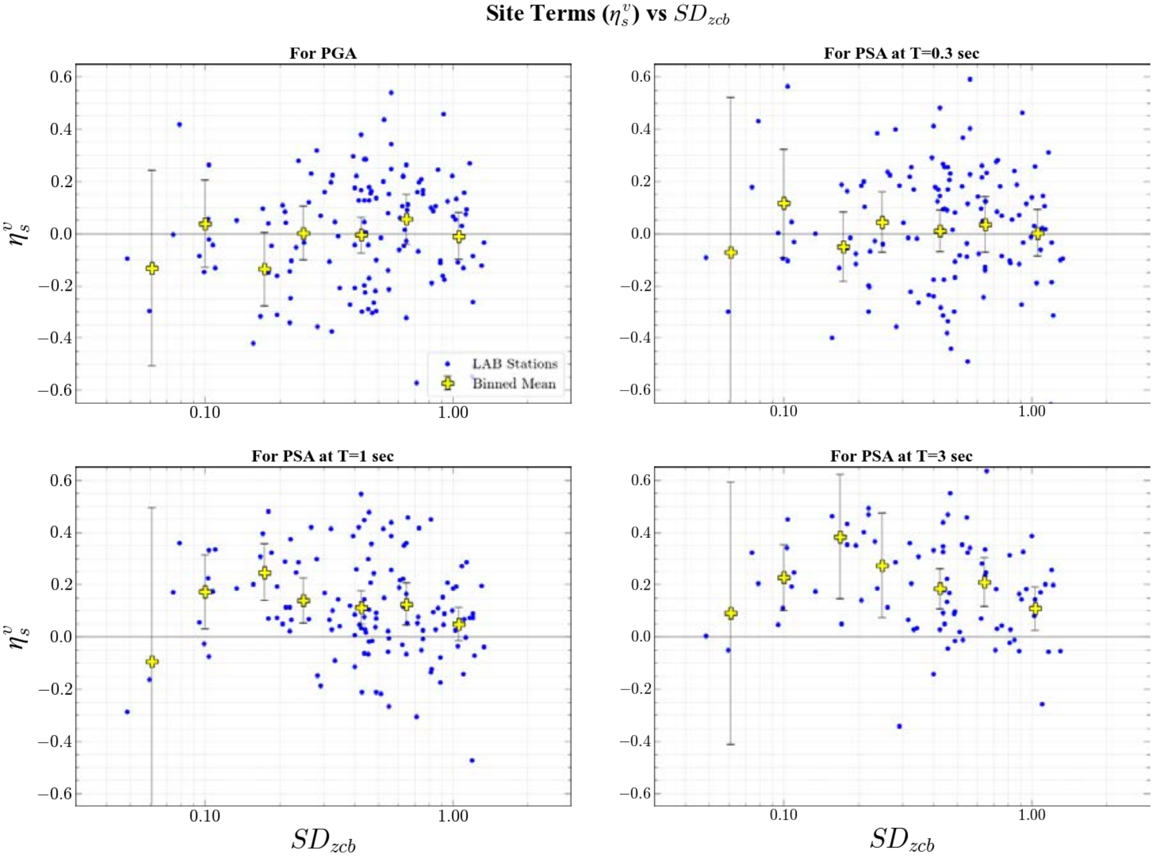

Figure 6.3: V_{S30}-adjusted Site Residuals η_s^v plotted against SD_{zcb} for LAB sites at different periods. Yellow markers show binned means.

3. η_s^b: Current full model, which incorporates V_{S30} scaling, basin depth, and basin category components of the site response, as per the Nweke et al. (2022) update (Figure 6.4).

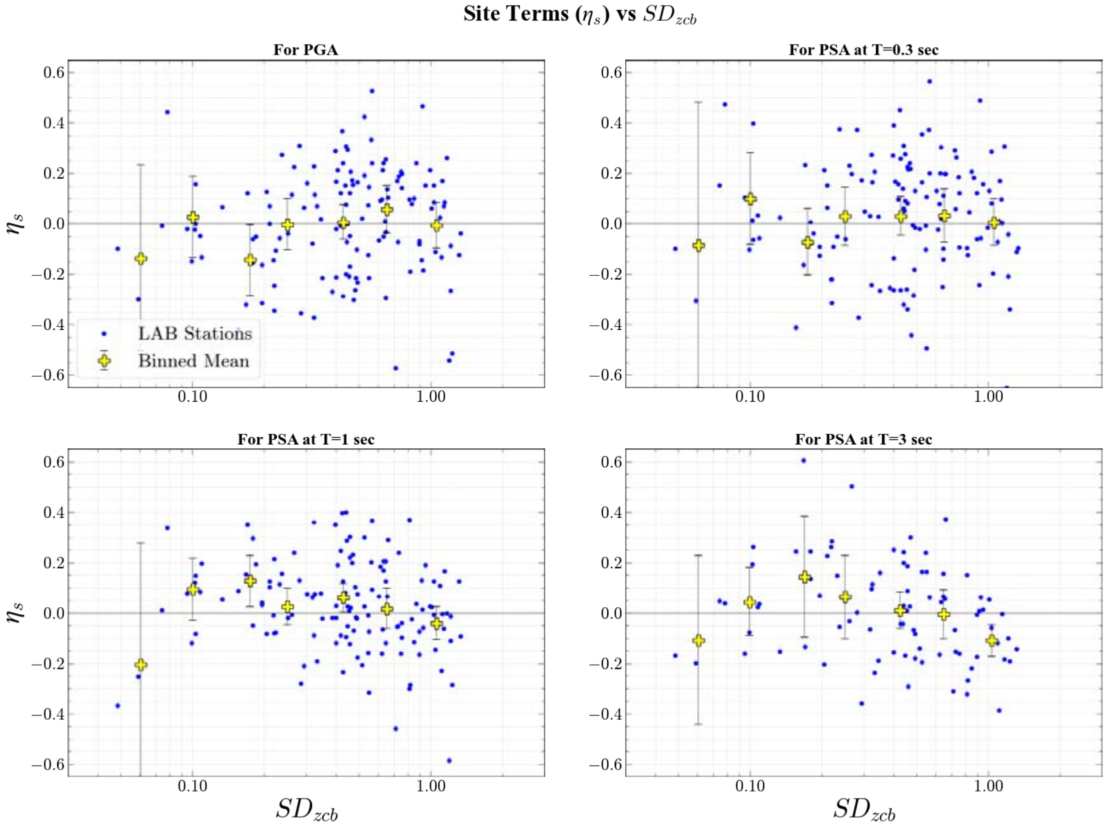

Figure 6.4: Basin- and V_{S30}-adjusted Site Residuals η_s^b plotted against SD_{zcb} for LAB sites at different periods. Yellow markers show binned means. **Note,** η_s^b is denoted as η_s for the the remainder of the chapter and report. This was done for simplicity in representing what is currently the full model site terms

Analysis of these figures reveals several noteworthy trends across the different site response model representation. For reference site conditions (η_s^r) in Figure 6.2, we observe a strong positive shift in the site terms (>0.5 ln units) that increases with period, which is expected as no site-specific representation is provided, indicating uncaptured site effects. The magnitude of this shift is so consequential that it masks any potential trends with SD_{zcb}. For the V_{S30}-adjusted site terms (η_s^v) in Figure 6.3, we see a significant improvement in describing site response, evident from the removal of the positive shift seen in Figure 6.2. However, V_{S30} alone does not fully capture the site response, as an increasing positive shift remains at long periods (T = 1 sec and T = 3 sec). In addition, an observable trend with SD_{zcb} emerges, which was initially masked in the reference condition. Finally, in the full model (η_s) shown in Figure 6.4, which incorporates an updated V_{S30} scaling and basin adjustments (basin depth and basin category) as per Nweke et al. (2022), we note that the positive shift at long periods observed in Figure 6.3 has been removed. However, negative trends at long periods still persist with SD_{zcb}.

These observations demonstrate the potential of SD_{zcb} to capture basin effects beyond those represented by conventional parameters like V_{S30}, basin depth, and basin category. The persistence of trends with site terms derived from the full model, particularly at longer periods, indicates that SD_{zcb} provides additional information about basin structure and its influence on site response. This suggests that SD_{zcb} could enhance site response predictions in basin environments, especially for effects related to basin-edge wave generation and complex wave propagation patterns in areas of variable basin depth, albeit implicitly. By providing an enhanced representation of these 3D basin effects not fully represented by 1D parameters, SD_{zcb} shows promise as a complementary component to existing site response models, potentially improving our understanding and prediction of seismic behavior in complex basin settings.

While SD_{zcb} shows promise as a geometric parameter for capturing basin effects, several limitations warrant consideration. For instance, the choice of using a 2500 m window size for its calculation is somewhat arbitrary[1] and may not be optimal for all basin settings, potentially affecting the parameter's effectiveness across different geological contexts. Additionally, the accuracy of SD_{zcb} calculations is inherently dependent on the reliability of the underlying z_{cb} model, introducing a potential source of uncertainty. Near the basin boundaries, edge features may exist that the full circular window does adequately capture, potentially compromising the parameter's accuracy in these areas. Despite these limitations, SD_{zcb} represents a promising approach to quantifying aspects of basin geometry that may influence site response. Further investigation is conducted in Chapter 8 to determine the most effective ways to incorporate it into seismic hazard analyses and ground motion prediction equations.

6.3 Distance from Basin Margin (R_b^{mar})

The Distance from Basin Margin (R_b^{mar}) is a geometric parameter designed to capture possible basin-edge effects in seismic response. These effects, which include the generation of surface waves that amplify of ground motions, play a crucial role in modifying seismic waves and can significantly impact the intensity and duration of ground shaking. The importance of basin-edge effects has been highlighted by several historical earthquakes, notably the 1994 Northridge earthquake in Los Angeles and the 1995 Kobe earthquake in Japan, where substantial damage was observed in areas near the basin edges (Graves et al., 1998; Kawase, 1996). The physical basis for these basin-edge effects lies in the complex interaction of seismic waves with abrupt changes in sediment thickness at basin boundaries. As seismic waves propagate from bedrock into the basin, they encounter a significant impedance contrast. This contrast, combined with the unique geometry of the basin edge, can lead to wave trapping. Moreover, the interaction between direct body waves entering the basin from below and surface waves generated at the basin edge can result in constructive interference, further amplifying ground motion amplitudes (Bard and Bouchon, 1985).

To quantify these effects, we introduce R_b^{mar}, calculated as the shortest distance from each site within the basin to the defined basin boundary. For the Los Angeles Basin (LAB), we use the revised basin outline described in Section 5.2 as our reference boundary. By analyzing the relationship between R_b^{mar} and site response characteristics, we aim to assess its effectiveness in capturing unresolve site amplification features, including basin-edge effects, and its potential to complement existing site response parameters in ground motion prediction equations. To evaluate the effectiveness of R_b^{mar} in capturing site response characteristics, we analyzed its relationship with site terms derived from our residual analysis, similar to the approach used for SD_{zcb}. Figures 6.5-6.7 present these relationships for different spectral periods and site response model representations.

---

[1] The choice of 2500 m for the radius is motivated by prior research endeavors related to basin classification algorithm development using surface texture. The details are provided in Nweke et al. 2020 and in the upcoming Nweke and Shams 202X.

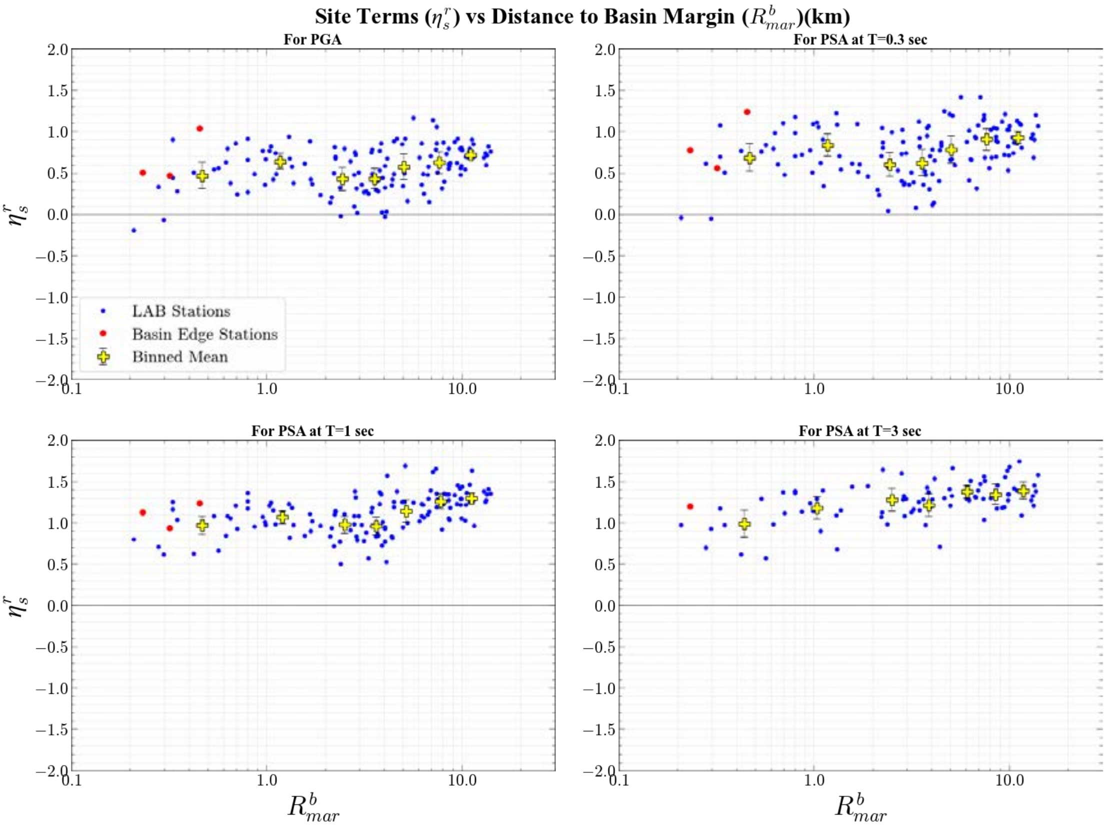

Figure 6.5: Site Residuals (η_s^r) plotted against R_b^{mar} (km) for LAB where red markers represent basin margin sites defined in Nweke et al. (2022) and yellow markers are binned means for all sites shown.

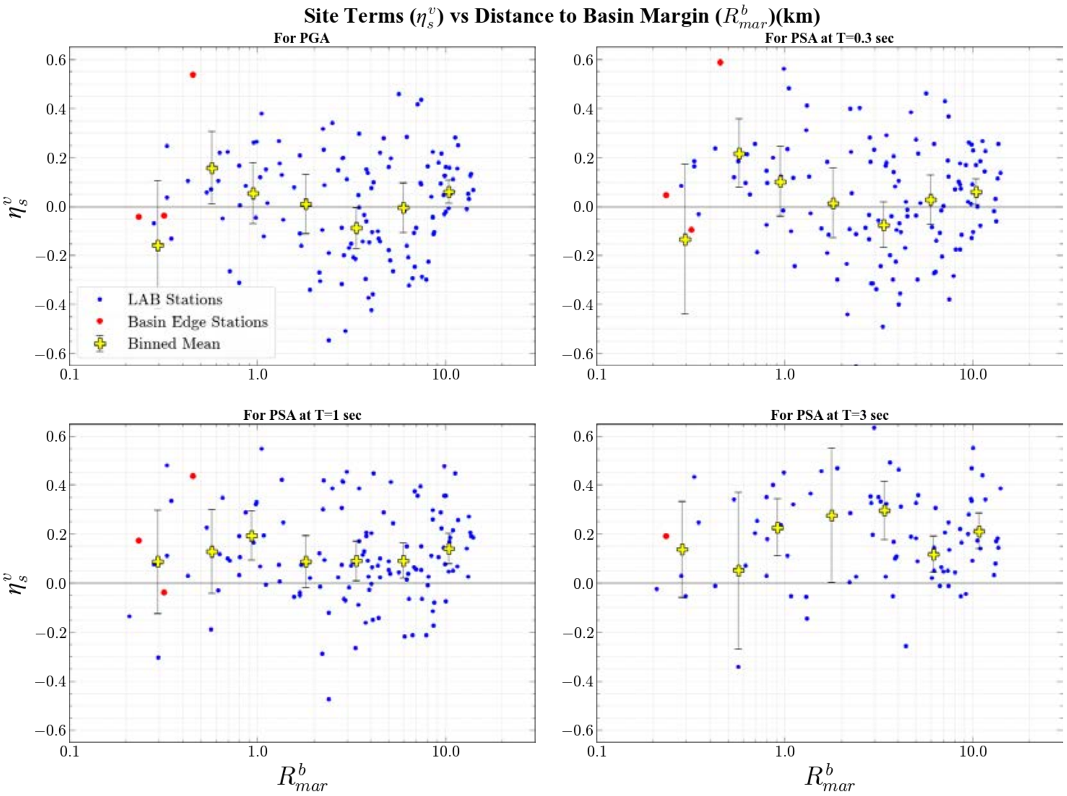

Figure 6.6: Site Residuals (η_s^v) plotted against $R_b{}^{mar}$ (km) for LAB where red markers represent basin margin sites defined in Nweke et al. (2022) and yellow markers are binned means for all sites.

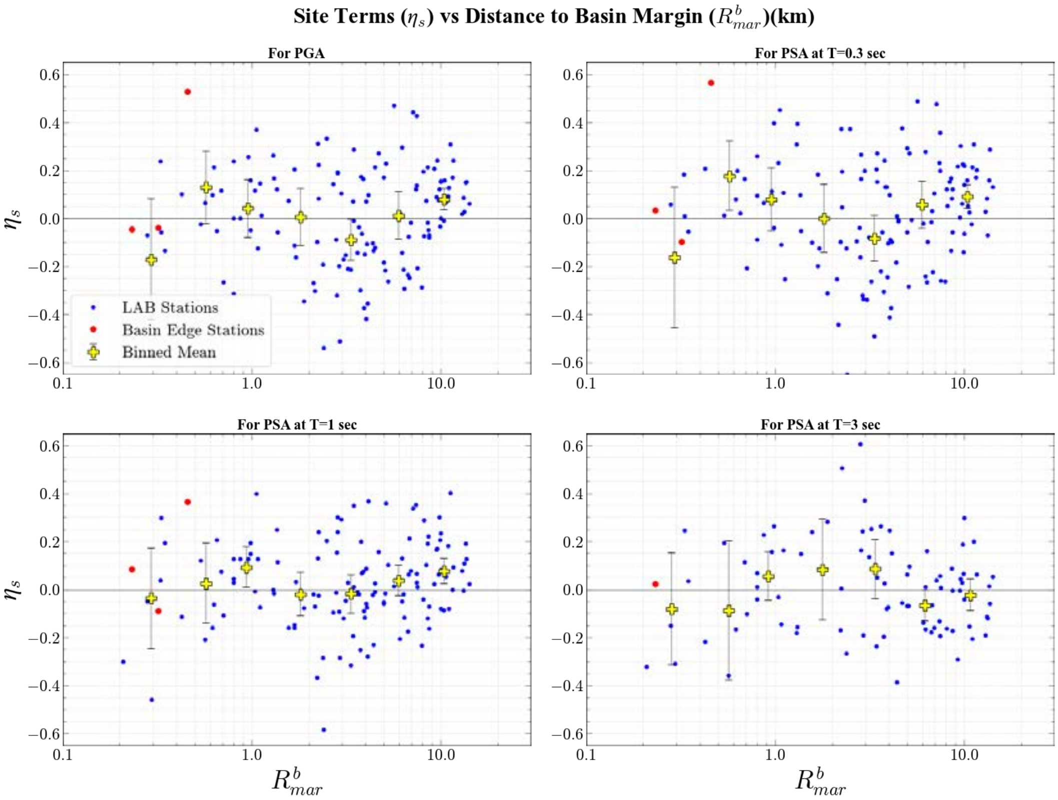

Figure 6.7 Site Residuals (η_s) plotted against $R_b{}^{mar}$ (km) for LAB where red markers represent basin margin sites defined in Nweke et al. (2022) and yellow markers are binned means for all sites.

Analysis of the relationship between $R_b{}^{mar}$ and the derived site terms reveals several key observations across different site response model representations. For the reference site terms (η_s^r, Figure 6.5), we observe a significant positive bias, indicating that site response is not considered when V_{S30} is set to the reference condition (760 m/s). This positive bias is largely removed when the V_{S30} adjustment is incorporated (η_s^v, Figure 6.6), although some positive bias remains at longer periods (T = 1 sec& T = 3 sec). In the full model (η_s, Figure 6.7), both V_{S30} and basin-based adjustments are introduced, and the remnant positive bias is completely eliminated. Notably, across all periods in the full model there are minimal observable trends in the site terms when considering $R_b{}^{mar}$ as the independent variable, with most of the binned means hovering around or close to zero, and their confidence intervals encompassing or approaching the zero line. Moreover, close inspection shows that the trends are non-unique (the cross the zero line at multiple values of $R_b{}^{mar}$. This lack of trend (or unorthodox relationship) in the full model suggests that $R_b{}^{mar}$ does not provide additional predictive capabilities beyond what is already offered by the conventional site parameters (V_{S30}, basin depth, and basin category). These observations indicate that while $R_b{}^{mar}$ exhibits some correlation with site response characteristics, these effects are largely captured by existing parameters in current ground motion models.

While $R_b{}^{mar}$ does not offer significant predictive power beyond existing site response parameters, it shows promise as a tool for identifying basin edge sites. Closer inspection of Figures 6.5-6.7 reveals an interesting pattern within approximately 2 km of the basin edge. This pattern is particularly evident in Figure 6.8 (at all periods), which highlights the observed 2 km threshold in the Los Angeles Basin as a quantitative basis for distinguishing between basin edge and basin interior locations. This distinction could be valuable for various applications in seismic hazard analysis and ground motion studies, and a spatial representation of the R_b^{mar} threshold in LAB is shown in Figure 6.9.

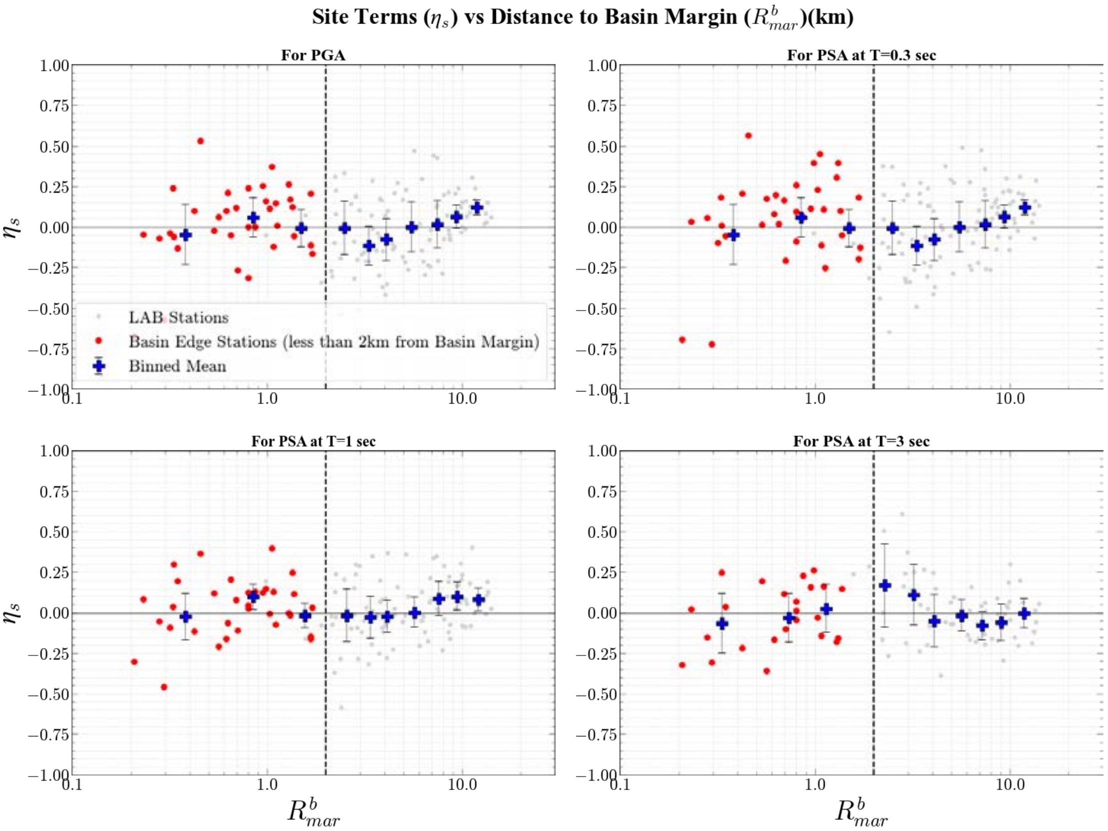

Figure 6.8: Site Residuals (η_s) plotted with R_b^{mar} (km) for LAB where red markers represent newly defined basin margin and blue markers are binned means for all sites.

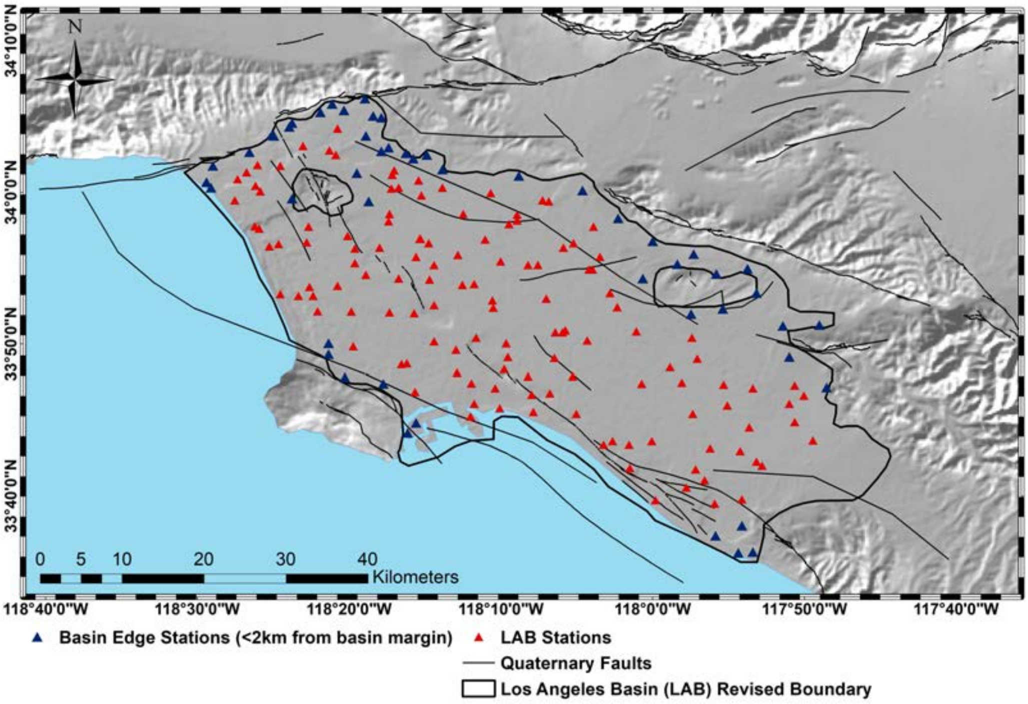

Figure 6.9: Map shows newly defined basin edge sites in LAB (blue triangles) and remaining sites (basin interior) in LAB are shown in red.

However, a preliminary extension of our analysis to other sedimentary basins in Southern California reveals that the threshold representing basin edge classification as described by R_b^{mar} may vary across different geological settings. For instance, when examining the inland basins (San Bernardino, Chino, and San Gabriel) as a group (due to lack of stations), we observed erratic patterns that vary with period (inconsistent thresholds; Figure 6.10). Here the threshold is determined as the breakpoint location in a piecewise curve estimated using a genetic algorithm-based fit. It is important to note that slightly erratic patterns in the threshold was observed when the coastal basin were combined (Los Angeles, San Fernando, and Ventura; Figure 6.11). This threshold pattern was different than the LAB results even though the coastal group included LAB sites and LAB dominates the data population. This erratic nature was also observed for pull-apart basins (Coachella Valley and Imperial Valley; Figure 6.12). These differences underscore the complexity of basin edges and highlight the need for basin-specific considerations in seismic hazard assessments. The variation in R_b^{mar} thresholds across different basin types suggests that a one-size-fits-all approach to defining basin edges may not be appropriate. Instead, a more nuanced, basin-specific approach might be the appropriate choice.

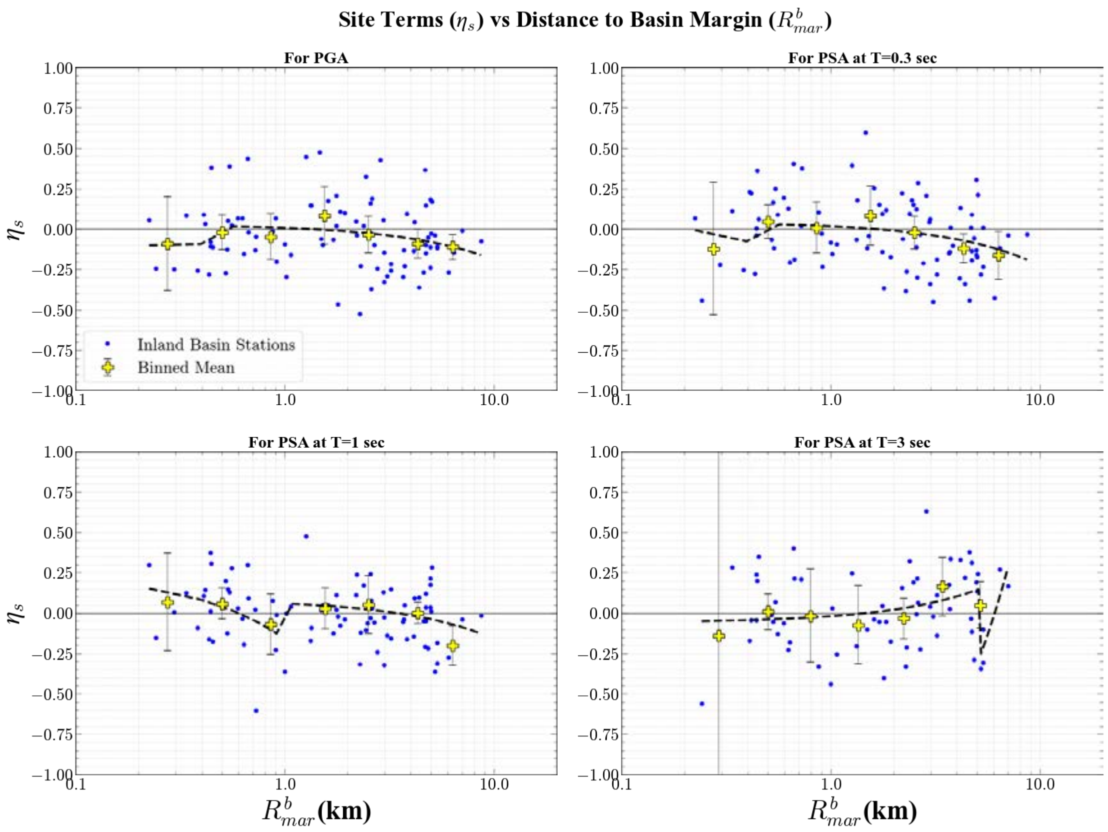

Figure 6.10: Site Residuals (η_s) plotted with R_b^{mar} (km) for sites in inland basins (SBB, CB and SGB) where yellow markers are binned means for all sites. The black dashed line indicates fit for the trend.

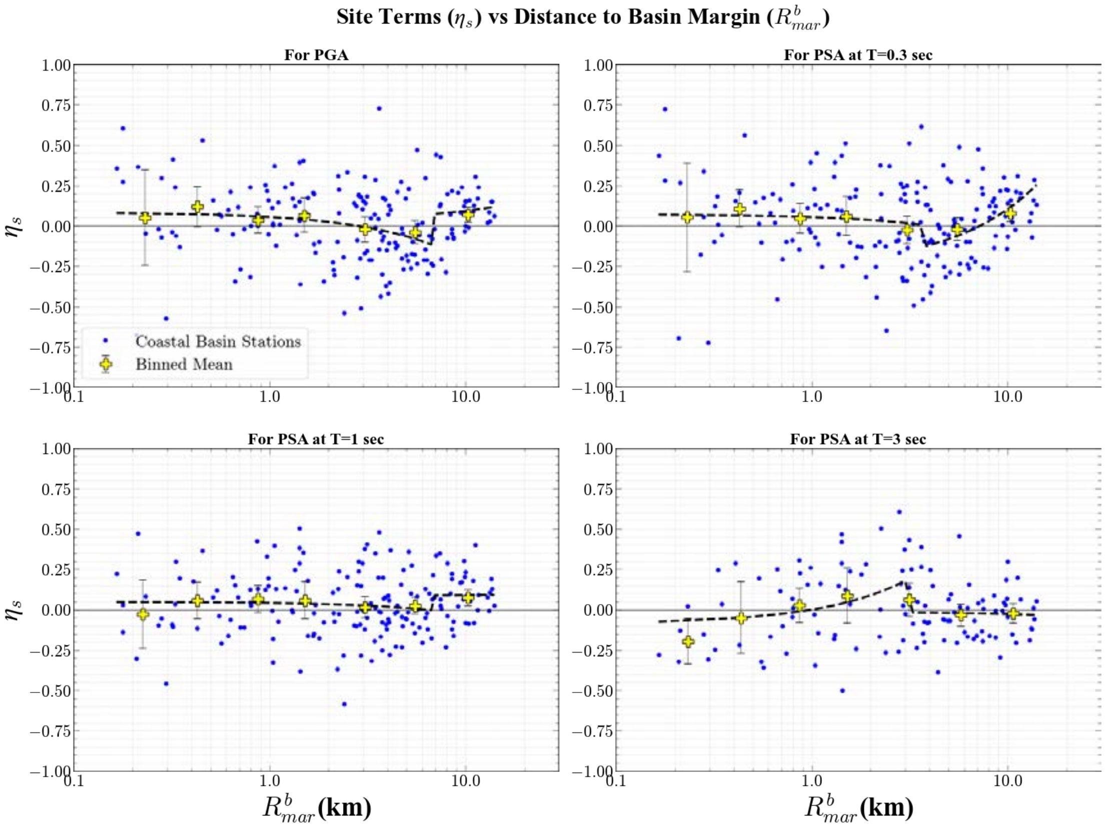

Figure 6.11: Site Residuals (η_s) plotted with $R_b{}^{mar}$ (km) for sites in coastal basins (LAB, SFB and VB) where yellow markers are binned means for all sites. The black dashed line indicates fit for the trend.

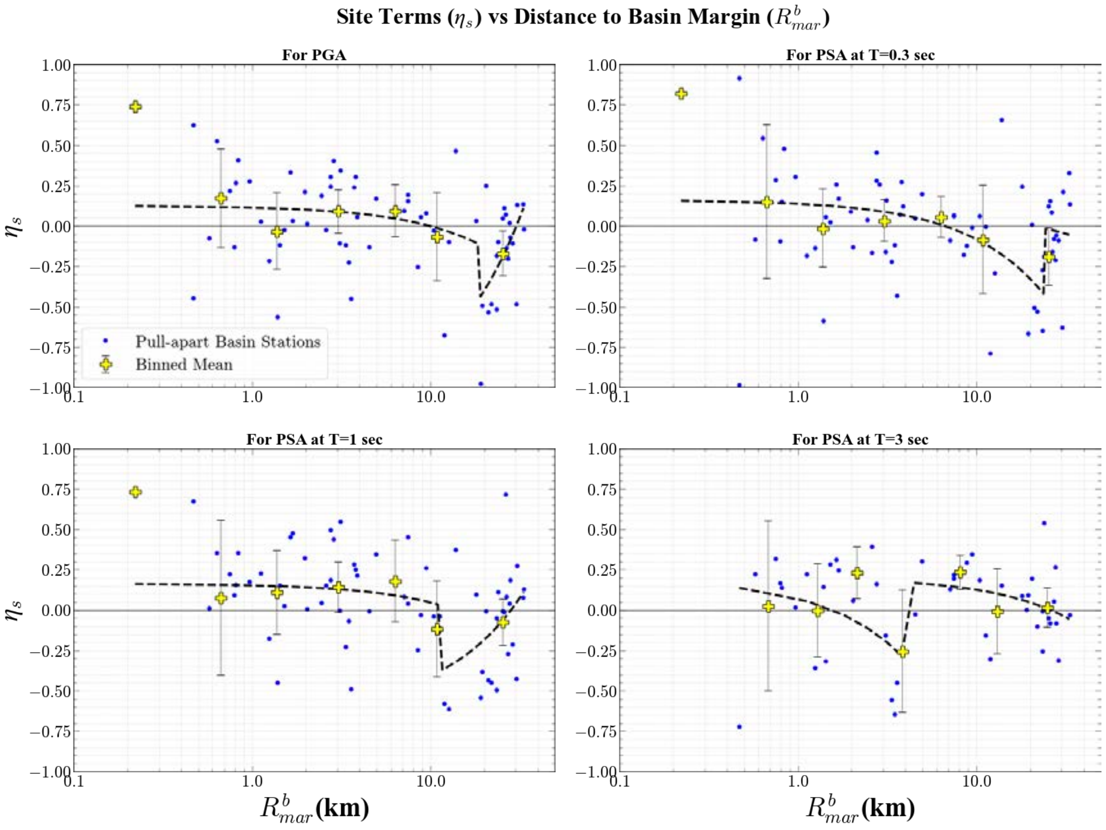

Figure 6.12: Site Residuals (η_s) plotted with R_b^{mar} (km) for sites in pull-apart basins (CVB and IVB) where yellow markers are binned means for all sites. The black dashed line indicates fit for the trend.

Despite the limited potential of R_b^{mar} as a predictive parameter for forward modeling via ground motion models, its value is exuded in its ability to identify and distinguish basin edge zones where complex seismic site response is likely to occur. This analysis of R_b^{mar} reveals its potential as a tool for refining seismic hazard assessments in basin environments. By quantifying the distance from basin margins, R_b^{mar} offers a method to distinguish between "basin edge" and "basin interior" sites, enabling a more nuanced classification system for sedimentary basins. This refined classification may not only guide focused studies on basin edge effects, but it may also aid in identifying areas where these effects are most significant. Such insights can be incorporated into seismic hazard maps, facilitating targeted risk mitigation strategies. Furthermore, the observed R_b^{mar} relationships may provide valuable benchmarks for validating and enhancing physics-based ground motion simulation methods, particularly in their ability to capture complex basin edge effects. Future research investigations will focus on validating and refining R_b^{mar} thresholds across a diverse range of global sedimentary basins, while delving into the physical mechanisms underlying variations in basin edge effects. These efforts promise to advance our understanding and improve the accuracy of seismic hazard assessments in complex basin environments.

6.4 Standard Deviation of Absolute Difference between $z_{1.5}$ and z_{cb} ($SD_{|zcb-z1.5|}$)

The Standard Deviation of the Absolute Difference between $z_{1.5}$ and z_{cb} ($SD_{|z1.5-zcb|}$) is a novel geometric parameter designed to capture the combined variability of potential impedance contrasts between sedimentary and crystalline basement depths. This parameter aims to quantify the complexities associated with the internal structure of a basin, particularly focusing on the transition zone between soft/stiff sediments, sedimentary rocks, and crystalline basement rocks.

The rationale behind $SD_{|z1.5-zcb|}$ lies in its potential to represent significant impedance contrasts within the basin structure. The $z_{1.5}$ surface often corresponds to the boundary between softer, near-surface sediments and more consolidated sedimentary rocks, while z_{cb} represents the interface with the crystalline basement. The variability in the difference between these surfaces may indicate complex basin geometry with varying sediment thickness and areas of strong velocity gradients that could affect site response. To compute $SD_{|z1.5-zcb|}$, we first calculate the absolute difference between $z_{1.5}$ and z_{cb} surfaces. We then apply a moving window with a 2500m radius to compute the standard deviation of this difference across the basin. This approach allows us to capture local variations in basin structure that may influence seismic wave propagation and amplification. To evaluate the effectiveness of $SD_{|z1.5-zcb|}$ in capturing site response characteristics, we analyzed its relationship with site terms derived from our residual analysis (Chapter 3). Figures 6.13-6.15 present these relationships for different spectral periods and site response model representations.

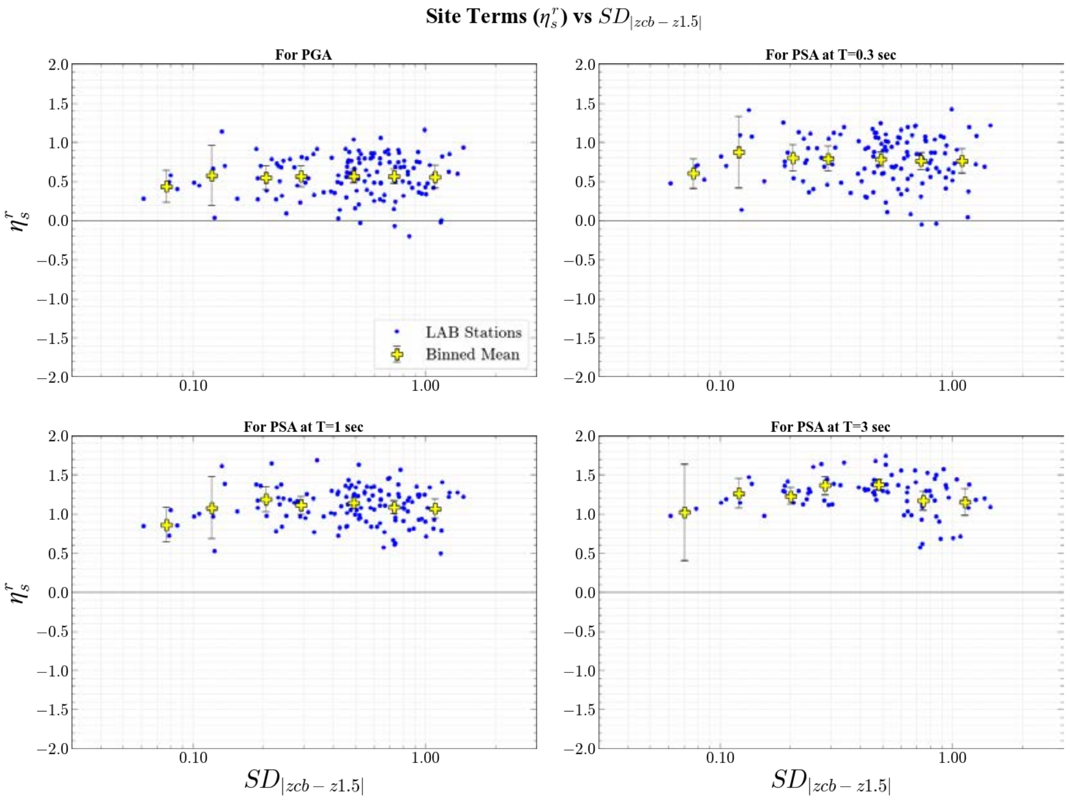

Figure 6.13: Site Residuals (η_s^r) plotted against $SD_{|zcb\text{-}z1.5|}$ for LAB where yellow markers are binned means for all sites.

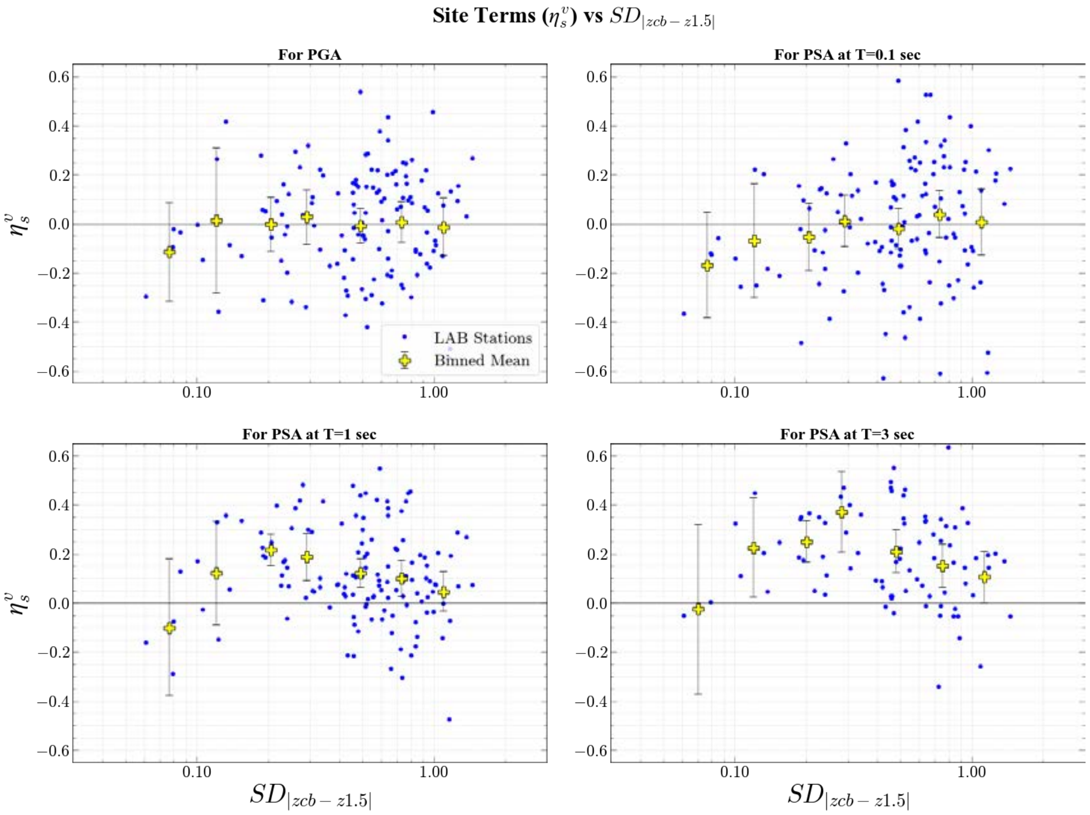

Figure 6.14: Site Residuals (η_s^v) plotted against $SD_{|zcb\text{-}z1.5|}$ for LAB yellow markers are binned means for all sites.

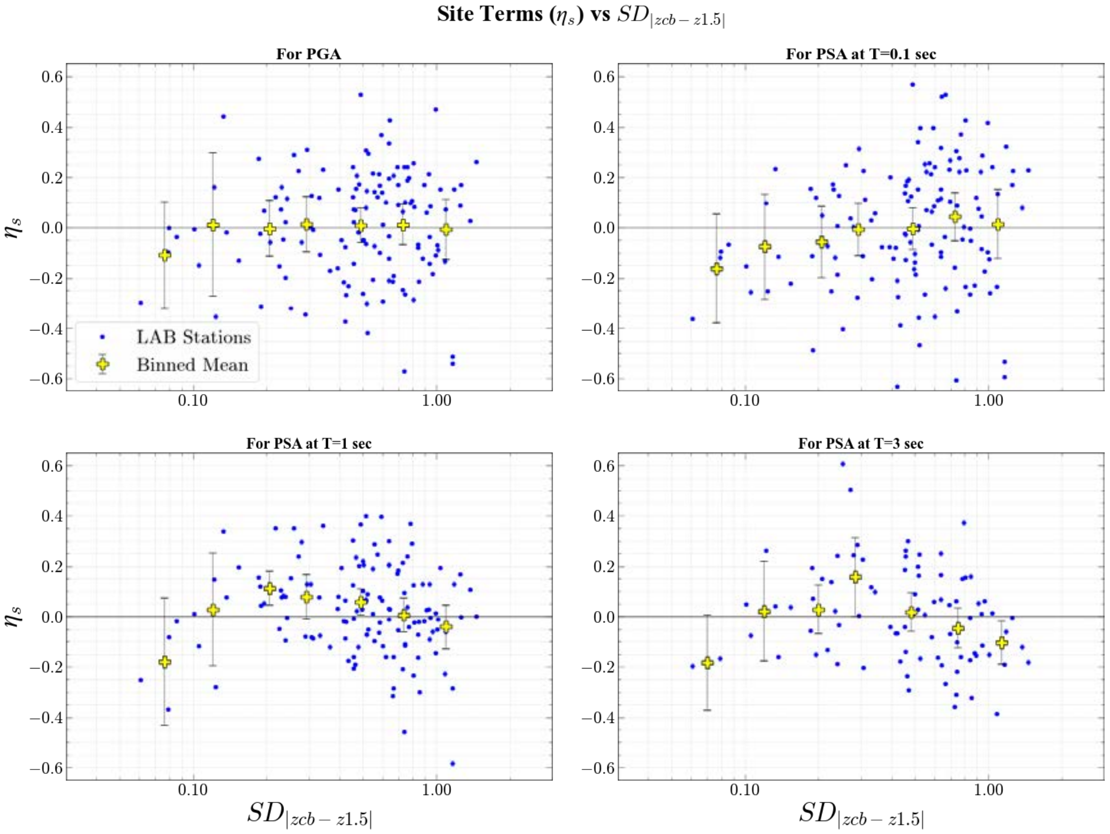

Figure 6.15: Site Residuals (η_s) plotted against $SD_{|zcb\text{-}z1.5|}$ for LAB where yellow markers are binned means for all sites.

Our analysis reveals that the reference site response model representation (η_s^r, Figure 6.13) shows significant positive bias (shift up in the site term/y-axis) for all periods, which is expected and similar to all previous cases where the geometric parameters are assessed under reference site conditions (V_{S30} = 760m/s). The V_{S30}-adjusted site terms (η_s^v, Figure 6.14) shows that this positive bias has been largely removed, except for some remnants at long periods (T = 1 sec and T = 3 sec). Additionally, the V_{S30}-adjusted site terms reveal negative trends with site terms for $SD_{|z1.5\text{-}zcb|} > (0.2 - 0.3)$ at long periods, and a positive trend for low-intermediate periods (T = 0.1 sec) starting around $SD_{|z1.5\text{-}zcb|} < 0.3$. In the full model ($\eta_s$, Figure 6.15), we observe further reduction in the bias/shift, but persistent trends remain, especially for longer periods. The complete removal of the positive bias now emphasizes the trends seen in the V_{S30}-adjusted site terms.

These findings suggest that $SD_{|z1.5\text{-}zcb|}$ captures aspects of basin response not fully accounted for by existing parameters, particularly for intermediate and longer period ground motions. Figure 6.16 illustrates the spatial variation of $SD_{|z1.5\text{-}zcb|}$ across the Los Angeles Basin. The map reveals higher values of $SD_{|z1.5\text{-}zcb|}$ along known fault lines and near basin edges, suggesting that this parameter effectively captures areas of complex basin geometry. This spatial distribution aligns with our understanding of where we might expect more complex seismic response due to basin structure.

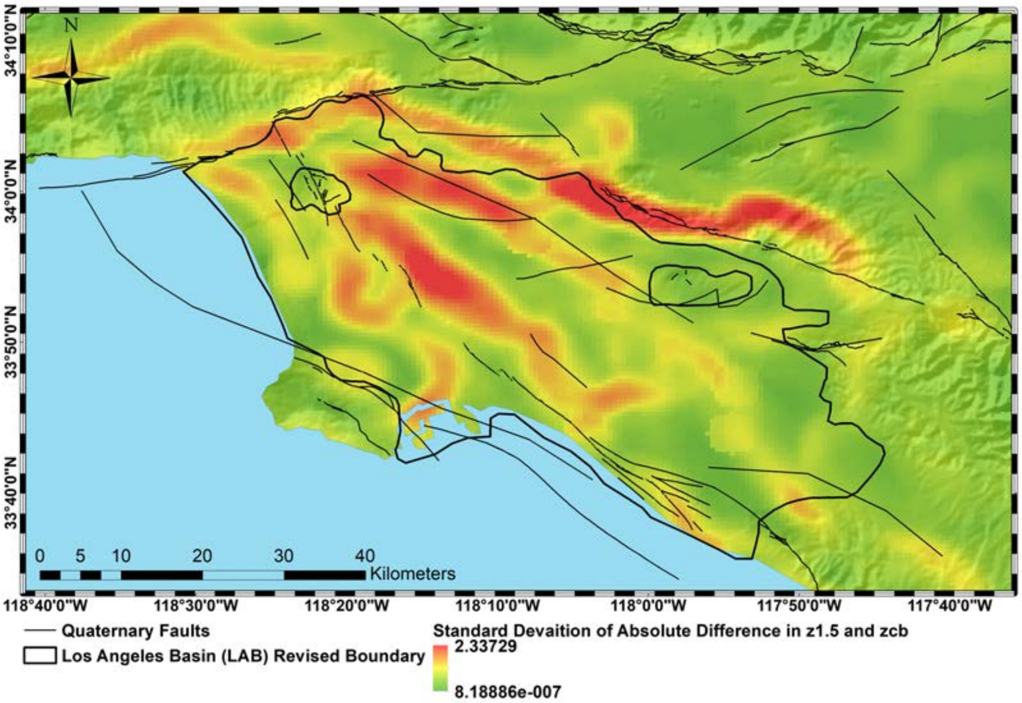

Figure 6.16: Spatial variation of $SD_{|z1.5\text{-}zcb|}$ along with basin outline for LAB (revised after Nweke et al. 2022) and surrounding quaternary faults.

The observed relationships between $SD_{|z1.5\text{-}zcb|}$ and site terms suggest that this parameter could improve site response predictions, particularly for intermediate and longer period ground motions. It could be incorporated into ground motion models as an additional predictor variable, potentially using a functional form that considers its stronger influence at longer periods. However, several limitations and considerations should be noted. For example, the effectiveness of $SD_{|z1.5\text{-}zcb|}$ depends on the accuracy and resolution of both $z_{1.5}$ and z_{cb} models for the basin of interest. Additionally, the 2500m window size used for estimating the parameter may not be optimal for all basin settings and should be further investigated. Still, $SD_{|z1.5\text{-}zcb|}$ shows promise as a parameter for capturing basin structure effects not fully addressed by conventional site response parameters. Its incorporation into ground motion models could potentially improve ground motion predictions in complex basin environments. In the subsequent chapters, we will develop a model using this parameter to further explore its potential in characterizing site response.

6.5 Surface Texture (S_{t2500})

Surface Texture (S_{t2500}) quantifies the variability of ground slope over a defined area, aiming to capture near-surface geological complexity that might influence seismic wave propagation. This parameter is calculated as the standard deviation of surface slope within a moving circular window of 2500 meters radius. The physical basis for considering surface texture in site response analysis stems from the idea that surface roughness might correlate with underlying geological structures or sediment distributions. Areas with high surface texture might indicate regions of complex topography associated with fault systems, basin edges, or mountainous terrain, which could potentially influence seismic wave behavior.

Prior analysis revealed that S_{t2500} shows some promise as a classifier between basin and non-basin regions, performing more effectively in this regard than other topographic parameters such as elevation, slope, or curvature (Nweke and Shams, 202x). This suggests that S_{t2500} may capture some aspects of basin geometry. However, when we examined the relationship between

S_{t2500} and site terms (η_s) derived from our residual analysis, we found that S_{t2500} did not show significant predictive capabilities. Figure 6.17 illustrates the relationship between S_{t2500} and site terms (η_s) for the full model, which includes V_{S30} scaling and basin effects.

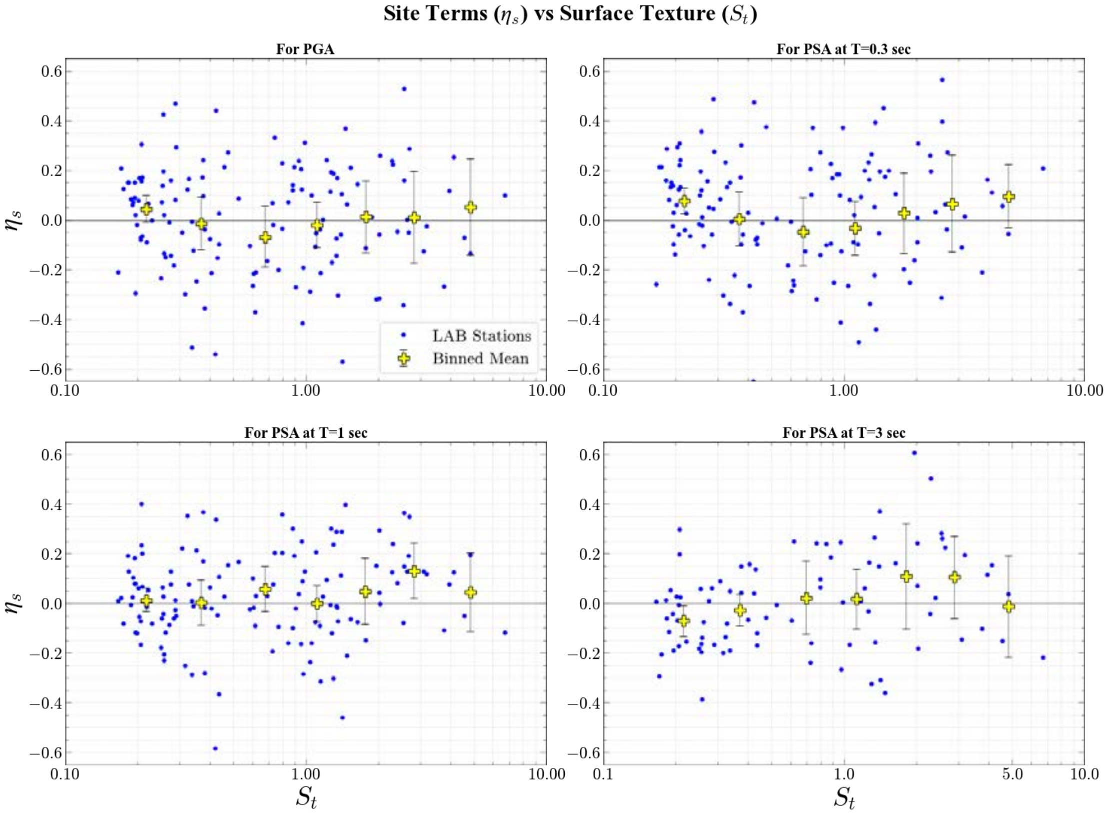

Figure 6.17: Site Residuals (η_s) plotted with S_{t2500} for LAB where yellow markers are binned means for all sites.

As evident from Figure 6.17, there are no clear trends between S_{t2500} and site terms across different periods. The binned means (yellow markers) hover around zero, indicating that S_{t2500} does not provide additional predictive power beyond what is already captured by conventional parameters in current ground motion models. This result underscores the challenge of developing new predictive parameters for site response and highlights the need for continued focus on subsurface characteristics in seismic hazard assessment. Future research could explore S_{t2500}'s potential indirect applications, such as guiding the selection of areas for detailed subsurface investigations or contributing to a more complex, multi-parameter model of basin effects.

6.6 Spatial Area of Influence for Seismic Site Response

Site response is influenced by the complex interactions between seismic waves and both surface and subsurface conditions, which extend beyond the immediate vicinity of a site. However, traditional one-dimensional (1D) site response analyses struggle to capture these multidimensional effects, often leading to inadequate estimation of ground motions during significant seismic events. This limitation has been evident in several earthquakes, including the Loma Prieta earthquake (Kiureghian and Neuenhofer 1992), the Kobe earthquake (Kawase 1996), the 1995 Dinar earthquake (Bakır et al. 2002), and the Christchurch earthquake (Chouw and Hao 2012), where 1D approaches failed to fully explain observed damage patterns. These shortcomings underscore the need for a more comprehensive approach that considers the three-dimensional nature of seismic wave propagation and site amplification.

Similarly, current ground motion model site response parameters provide only a limited, one-dimensional representation of site conditions. V_{S30}, for instance, represents an average of shear wave velocities in just the upper 30 meters of the soil profile, neglecting deeper velocity structures that can significantly influence ground motions, particularly at longer periods. Basin depth parameters (e.g., $z_{1.0}$, $z_{2.5}$) estimate sediment thickness but fail to account for lateral variations in basin geometry or internal structure. Basin category designations (i.e., basin and basin edge, valley, mountain-hill) attempt to capture some lateral variation but provide no information about basin shape or other 2D characteristics affecting wave propagation. These simplified 1D parameters, while useful for certain applications, are inherently limited in their ability to represent the complex 3D environments in which seismic waves propagate.

To address these shortcomings, we introduce the concept of Spatial Area of Influence (SAI) for seismic site response. SAI aims to quantify the extent of both lateral and vertical variability in site properties that contribute to the observed ground motion at a given location. This approach recognizes that seismic waves can deviate from vertical propagation due to scattering, focusing, and other 3D effects. For example, the trapping and amplification of seismic waves at the margins of sedimentary basins demonstrate how lateral heterogeneity can significantly impact site response due to basin edge effects. Similarly, buried topography or deep velocity contrasts can create complex wave propagation patterns that are not captured by traditional 1D methods. By incorporating both lateral and vertical variability, SAI offers a more nuanced representation of the geological factors that influence site response, potentially improving our ability to predict and understand complex ground motion behaviors in seismically active regions.

6.6.1 Spatial Area of Influence based on V_S Slope (SAI_{Vs})

The Spatial Area of Influence based on the slope of the shear wave velocity profile (SAI_{Vs}) quantifies both lateral and vertical variability in site conditions, aiming to capture complex 3D site characteristics that influence seismic wave propagation. SAI_{Vs} integrates surface texture, representing horizontal variability, with the standard deviation of the slope of the shear wave velocity profile between the crystalline basement (z_{cb}) and the 1.5 km/s velocity horizon ($z_{1.5}$), reflecting vertical variability. This approach recognizes that seismic site response is influenced by both near-surface heterogeneity and deeper velocity structures, potentially providing a more comprehensive representation of site conditions compared to traditional 1D parameters like V_{S30} or basin depth.

We compute SAI_{Vs} through a multi-step process that integrates both surface and subsurface characteristics. First, we calculate surface texture (S_{t2500}) using a 2500m radius moving window, which captures the local variability in surface slope. Next, we compute the shear wave velocity gradient (V_{S_slope}) between the crystalline basement (z_{cb}) and the 1.5 km/s velocity horizon ($z_{1.5}$) using Equation 5:

$$Slope\ of\ Vs\ between\ \text{zcb and z1.5} = \frac{abs(z_{cb} - z_{1.5})}{abs(Vs_{zcb} - Vs_{z1.5})} \tag{5}$$

This step quantifies the vertical velocity gradient in the deeper basin structure. We then determine the standard deviation of this velocity gradient (SD_{Vs_slope}) using another 2500m radius moving window, capturing the spatial variability in the velocity structure. Finally, we calculate SAI_{Vs} as the average of S_{t2500} and SD_{Vs_slope} using Equation 6:

$$SAI_{Vs} = average\left(S_{t2500}, SD_{V_{S\_slope}}\right) \tag{6}$$

This combination allows SAI_{Vs} to represent both surface and subsurface variability in a single parameter. A higher value of SAI_{Vs} would mean that site is in a more heterogenous regime. This heterogeneity could be present in either the lateral or vertical domain extents at the site

To evaluate the effectiveness of SAI_{Vs}, we analyzed its relationship with site terms (η_s) derived from our residual analysis. Figures 6.18 illustrates the relationship between the velocity gradient and the site terms while Figure 6.19 illustrate these relationships for SAI_{Vs}, both for different spectral periods.

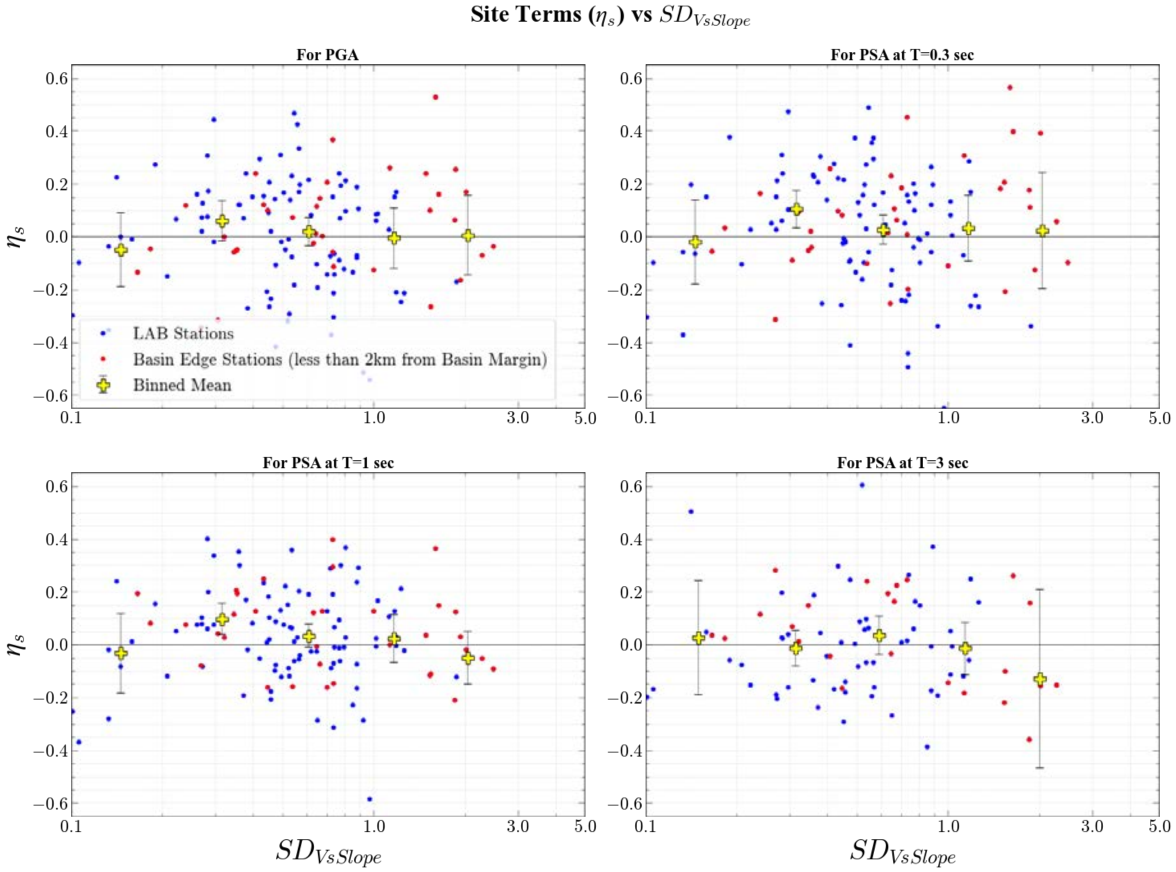

Figure 6.18: Site Residuals (η_s) plotted with $SD_{V_{S\_slope}}$ for LAB where yellow markers are binned means.

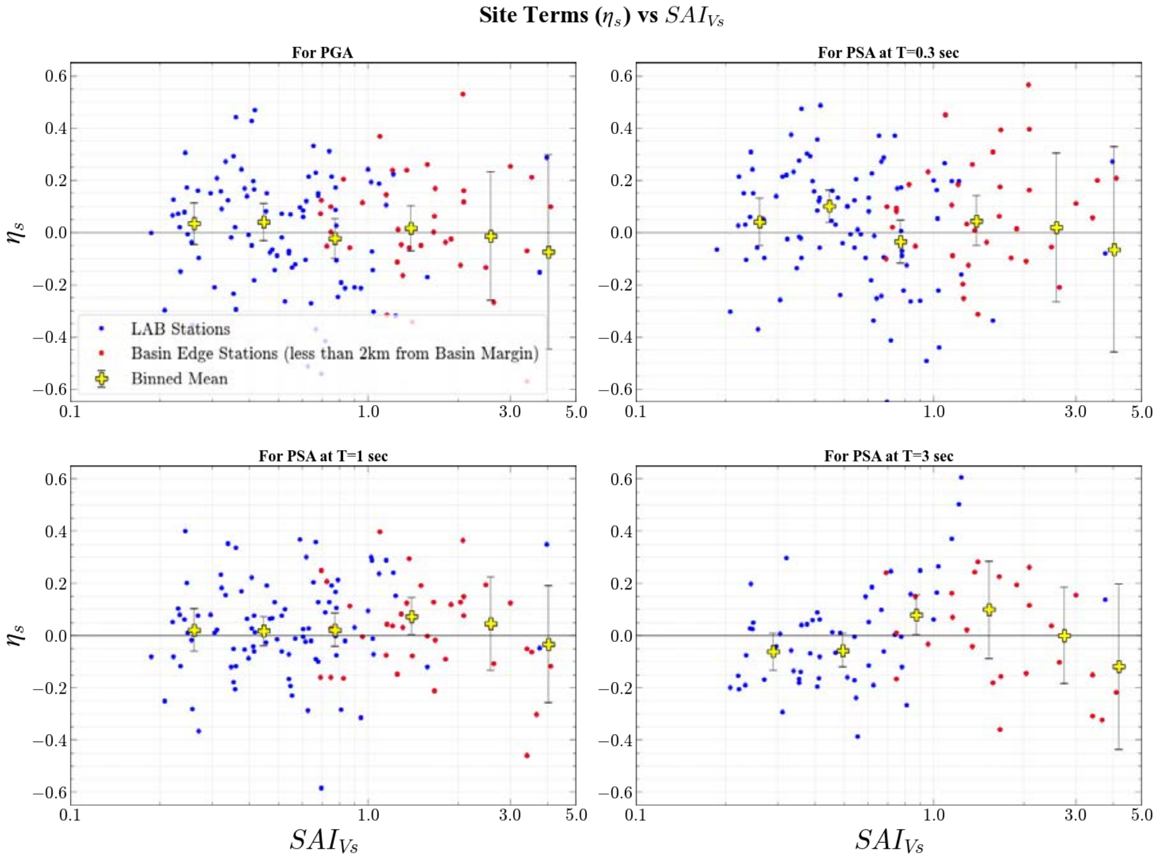

Figure 6.19: Site Residuals (η_s) plotted with SAI_{Vs} for LAB where yellow markers are binned means for all sites and red markers show newly defined basin margin sites in LAB.

Comparing Figures 6.18 and 6.19 reveals important insights. Figure 6.18, showing the relationship between $SD_{V_{S\_slope}}$ and site terms, exhibits minimal trends and does not discern between basin interior and basin edge sites. In contrast, Figure 6.19, which illustrates the full SAI_{Vs} (combining $SD_{V_{S\_slope}}$ and S_{t2500}), demonstrates a clear distinction between basin interior and edge sites. Moreover, patterns begin to emerge in the relationship between SAI_{Vs} and site terms, particularly at longer periods (positive bias "hump" at $1 < SAI_{Vs} < 2$). These observations suggest that SAI_{Vs} captures aspects of site response not fully accounted for by existing parameters, especially for longer period ground motions and basin edge effects. The enhanced performance of SAI_{Vs} compared to $SD_{V_{S\_slope}}$ alone underscores the importance of considering both lateral and vertical variability in site response analysis.

Despite its promising results, several limitations of SAI_{Vs} should be considered. The effectiveness of this parameter heavily depends on the accuracy of both surface elevation data and velocity models, which may vary across different regions. Additionally, the 2500m window size used in our calculations may not be optimal for all geological settings, potentially affecting the parameter's performance in areas with significantly different spatial scales of variability. Furthermore, the calculation of SAI_{Vs} may pose challenges in areas with limited subsurface data, potentially restricting its applicability in less-studied regions. Acknowledging these limitations, in subsequent chapters, we will develop a model using SAI_{Vs} to further explore its potential in improving site response predictions, particularly for intermediate and longer period motions in complex basin environments.

6.6.2 Spatial Area of Influence (SAI) based on Standard Deviation of V_{S30}

Building upon the concept introduced in Section 6.6.1, we explore another variant of the Spatial Area of Influence, this time focusing on a parameter related to the standard deviation of V_{S30} ($SAI_{V_{S30}}$). While SAI_{Vs} aims to capture variability in the deeper basin structure, $SAI_{V_{S30}}$ concentrates on near-surface conditions, potentially providing insights into the effects of shallow heterogeneity on site response and its implicit correlation with effects from the deeper basin structure. The computation of $SAI_{V_{S30}}$ follows a similar process to SAI_{V_S}, but replaces the standard deviation of velocity gradient ($SD_{V_{S\_slope}}$) with the standard deviation of V_{S30} ($SD_{V_{S30}}$). We use the Wills et al. (2015) V_{S30} map as the basis for this calculation shown in Figure 6.20. The final $SAI_{V_{S30}}$ parameter is then computed as the average of surface texture (S_{t2500}) and the standard deviation of V_{S30} ($SD_{V_{S30}}$) as shown in Equation 7:

$$SAI_{Vs30} = average(S_{t2500}, SD_{V_{S30}}) \tag{7}$$

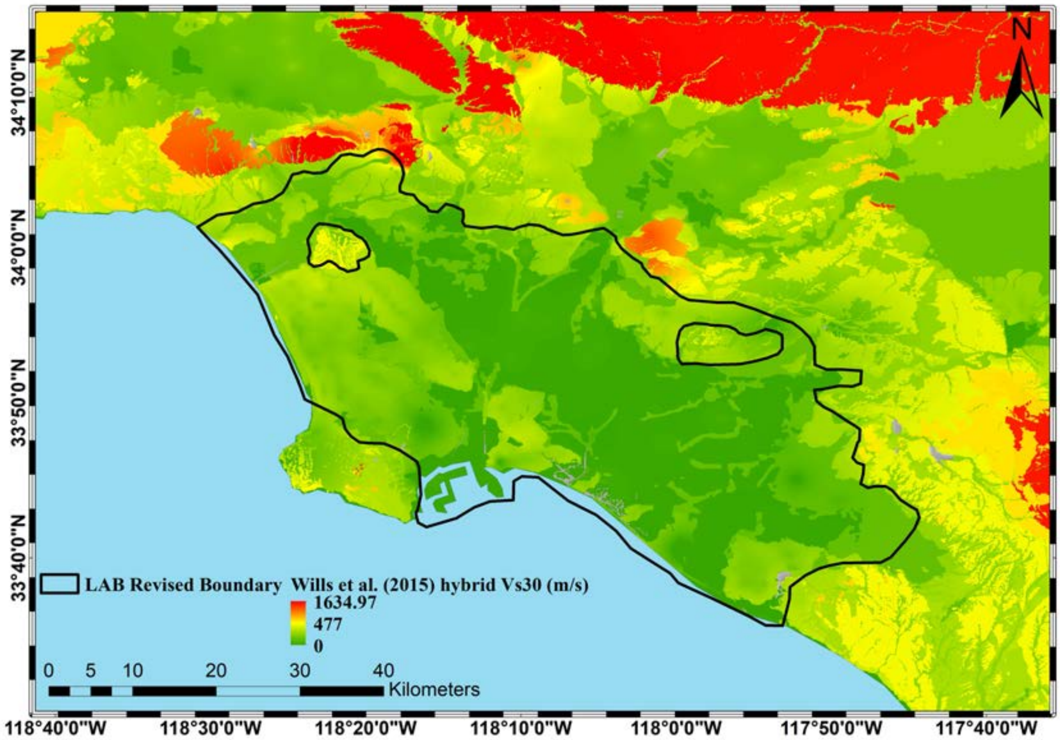

Figure 6.20: Spatial distribution of V_{S30} for LAB based on Wills et al. (2015)-hybrid, where green colour represents softer deposits while red colour represents stiffer deposits.

To evaluate the effectiveness of $SAI_{V_{S30}}$, we analyzed its relationship with site terms derived from our residual analysis, comparing it with the performance of $SD_{V_{S30}}$ alone. Figures 6.21 illustrates the relationship between and $SD_{V_{S30}}$ and site terms that have been adjusted using V_{S30}, $z1.0$, and basin category (the current full site response GMM). Figure 6.22 illustrate the relationships between $SAI_{V_{S30}}$ and V_{S30}-adjusted site terms, while Figure 6.23 does the same but for site terms that have been adjusted for the current full site response parameters. All three figures (6.21-6.23) show the variation of the respective relationships for different spectral periods for both Southern California (SoCal) and the Los Angeles Basin (LAB).

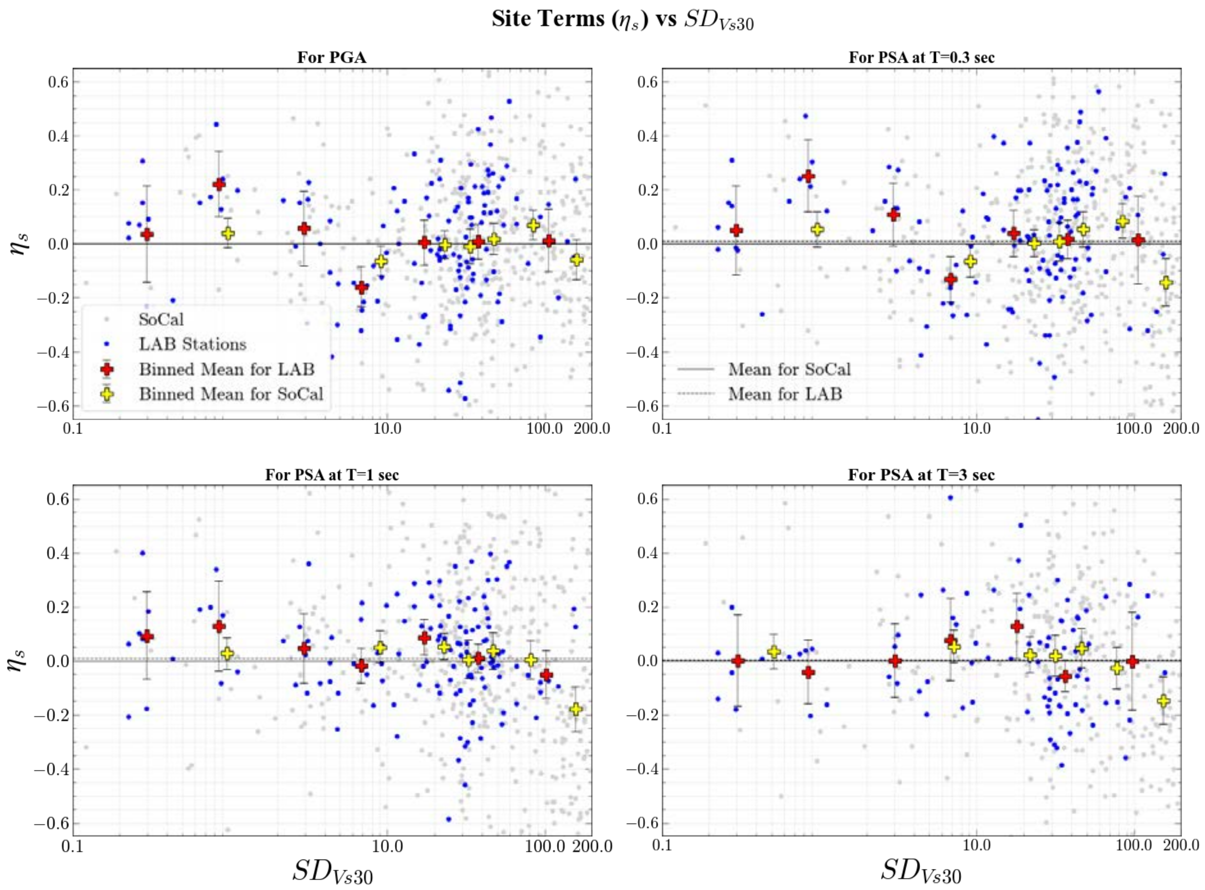

Figure 6.21: Site Residuals (η_s) plotted with Standard deviation of V_{S30} for LAB (blue markers) where yellow markers are binned means for LAB sites.

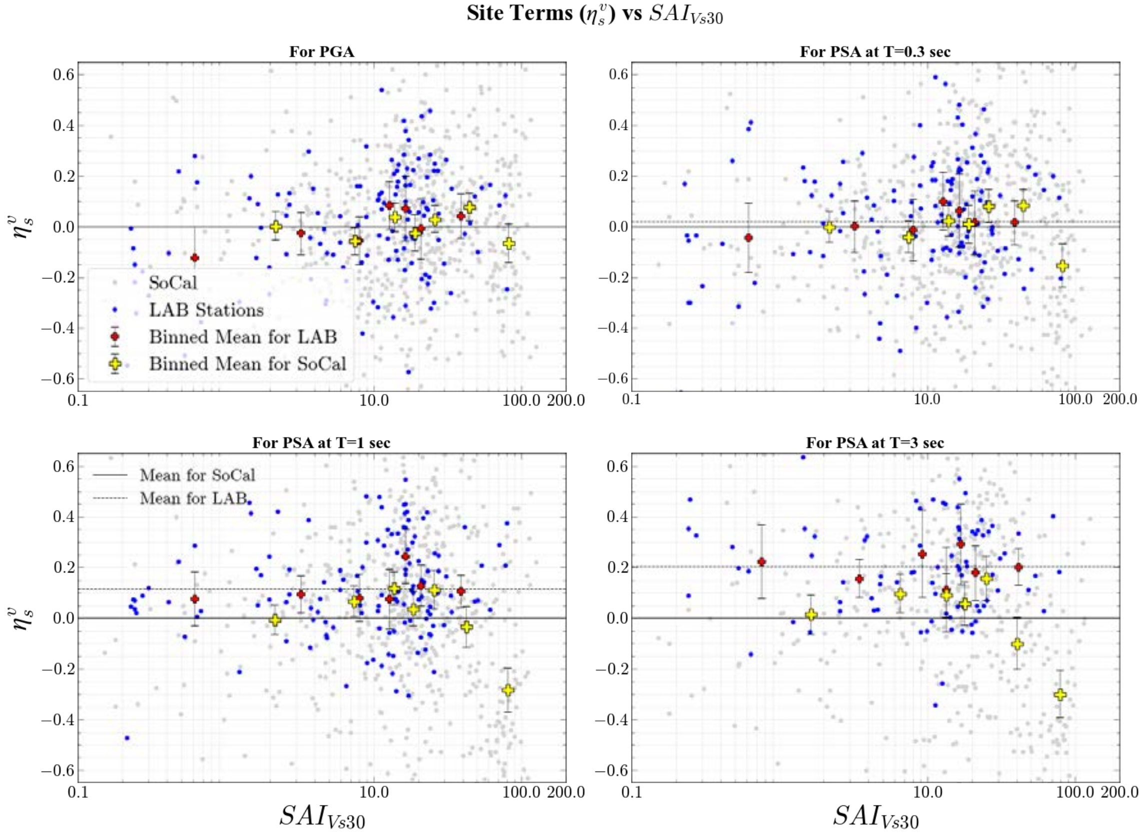

Figure 6.22: Site Residuals (η_s^v) plotted with $SAI_{V_{S30}}$ for SoCal (grey markers) and LAB (blue markers) where yellow and red markers are binned means for SoCal and LAB sites, respectively.

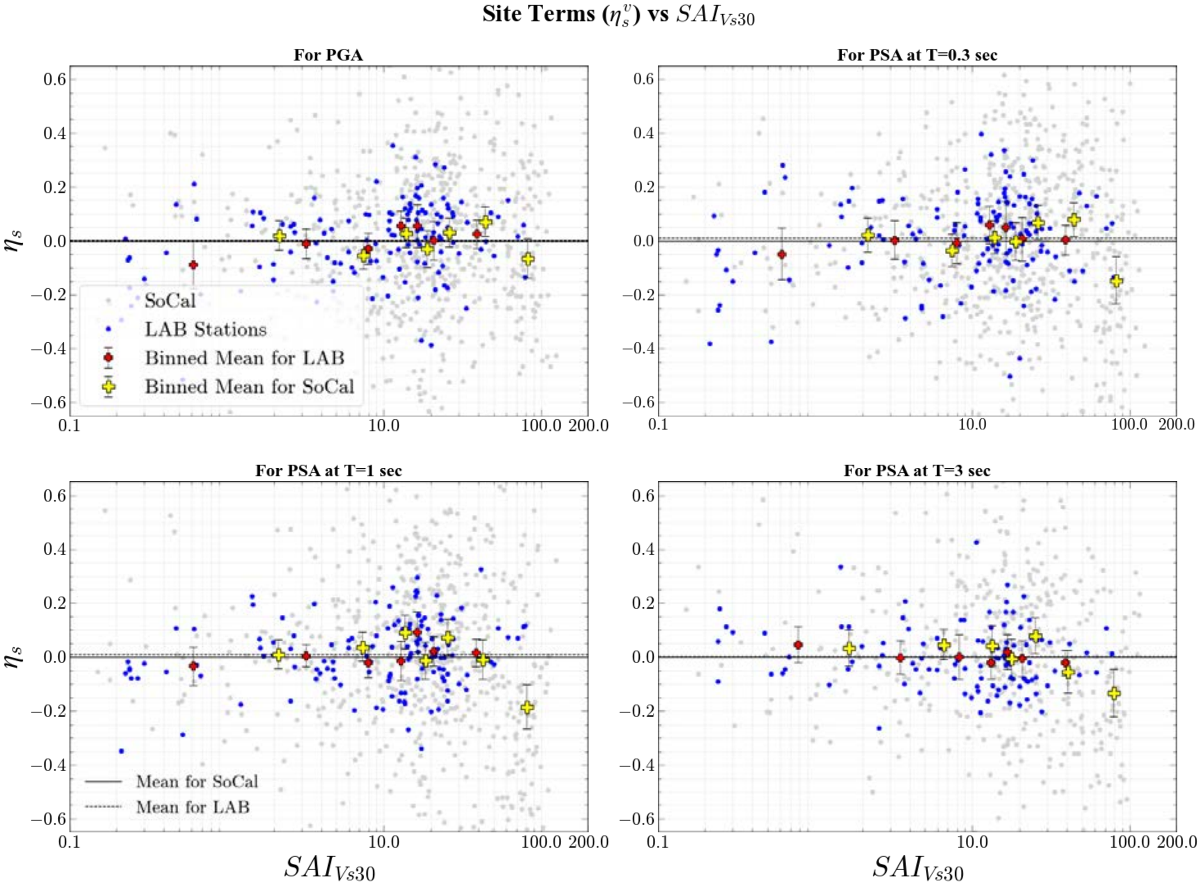

Figure 6.23: Site Residuals (η_s) plotted with $SAI_{V_{S30}}$ for SoCal (grey markers) and LAB (blue markers) where yellow and red markers are binned means for SoCal and LAB sites, respectively.

Analysis of Figure 6.21 reveals that $SD_{V_{S30}}$ alone does not provide significant benefits compared to the combination of V_{S30}, $z_{1.0}$, and basin categories. However, it exposes an interesting pattern of positive bias for low $SD_{V_{S30}}$ that diminishes with increasing period. When $SD_{V_{S30}}$ is combined with surface texture to form $SAI_{V_{S30}}$, we observe positive bias for LAB at long periods compared to SoCal (blue dots on average are higher than the gray dots) for V_{S30}-adjusted site terms, shown in Figure 6.22. This bias is removed when basin depth and basin category adjustments are applied, shown in Figure 6.23. In these fully adjusted site terms, $SAI_{V_{S30}}$ exhibits a trend of negative site terms at high $SAI_{V_{S30}}$ values ($SAI_{V_{S30}} > 20$) for long periods, indicating an overestimation (i.e., deamplification) of ground motion estimates for high variability sites. Interestingly, the pattern of positive bias at low variability sites observed in the $SD_{V_{S30}}$ plots (Figure 6.21) persist Figure 0.1 in the V_{S30}-adjusted site terms for $SAI_{V_{S30}}$ (Figure 6.22). However, this feature changes in the fully adjusted site terms (Figure 6.23), showing a positive bias at low $SAI_{V_{S30}}$ regions that slightly increases with period.

These observations suggest that $SAI_{V_{S30}}$ captures aspects of site response not fully accounted for by existing parameters, particularly for longer period ground motions in SoCal. The differing patterns between LAB and SoCal highlight the potential importance of regional geological context in interpreting these parameters. As with SAI_{V_S}, several limitations should be considered when deriving $SAI_{V_{S30}}$, including its dependence on data accuracy and resolution, and the potential influence of the chosen window size. In subsequent chapters, we will develop models using both SAI_{V_S} and $SAI_{V_{S30}}$ to further explore their potential in improving site response predictions, particularly for intermediate and longer period motions in complex basin environments.

6.7 Basin Eccentricity or Distance from Basin Centroid (C_b)

Basin Eccentricity, represented by the Distance from Basin Centroid (C_b), is a geometric parameter that aims to quantify the potential influence of a site's relative position within a basin on its seismic response. This parameter is calculated as the Euclidean distance between each site and the geometric center (centroid) of the basin, using the revised Los Angeles Basin outline discussed in Section 5.2. Figure 6.24 shows a schematic representation of in the Los Angeles Basin. The physical basis for considering C_b stems from the understanding that seismic wave propagation and amplification can vary significantly across a basin due to factors such as wave focusing, basin-edge effects, and resonance patterns. Sites closer to the basin center may experience different amplification patterns compared to those near the edges, due to the cumulative effects of the basin structure on wave propagation.

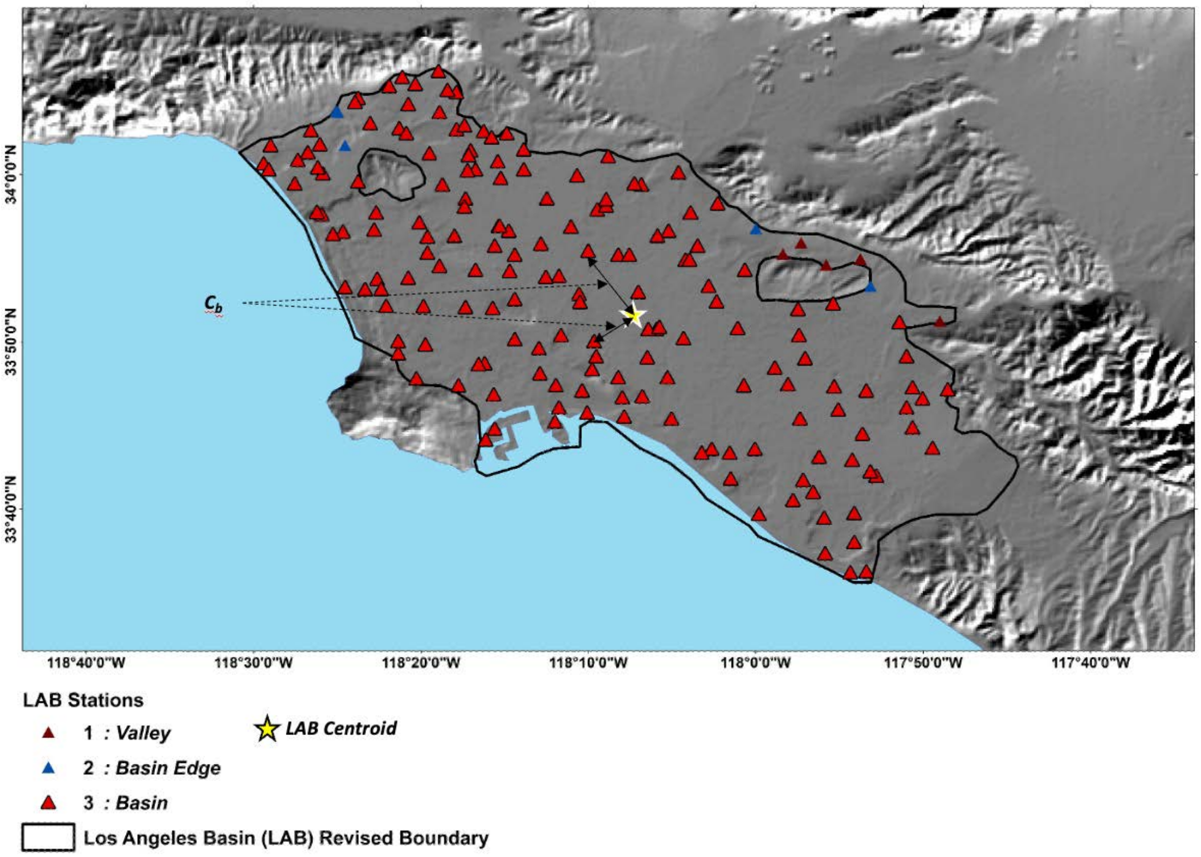

Figure 6.24: Schematic representation of basin eccentricity in the LAB region.

To evaluate the effectiveness of C_b in capturing site response characteristics, we analyzed its relationship with site terms derived from our residual analysis. The relationship with unadjusted site terms (η_S^r; V_{S30} = 760 m/s) exhibited a positive shift in site terms, as was observed in all other parameters investigated so far. In adherence to the pattern, the vs30-adjusted site terms showed a significant reduction in this shift, indicating that V_{S30}'s effectiveness as a1D descriptive parameter. However, a negative trend persisted showing positive site terms on average for sites closer to the basin centroid that decreases and eventually becomes a negative site term at sites that have large distances relative to the basin centroid. In addition, this effect diminishes with increasing period and is no observed for periods greater than T = 3 seconds. Figure 6.25 illustrates these trends persist in the relationship between C_b and fully adjusted site terms, indicating that there are remnant features of site response at short to intermediate periods that C_b captures beyond what current parameters describe.

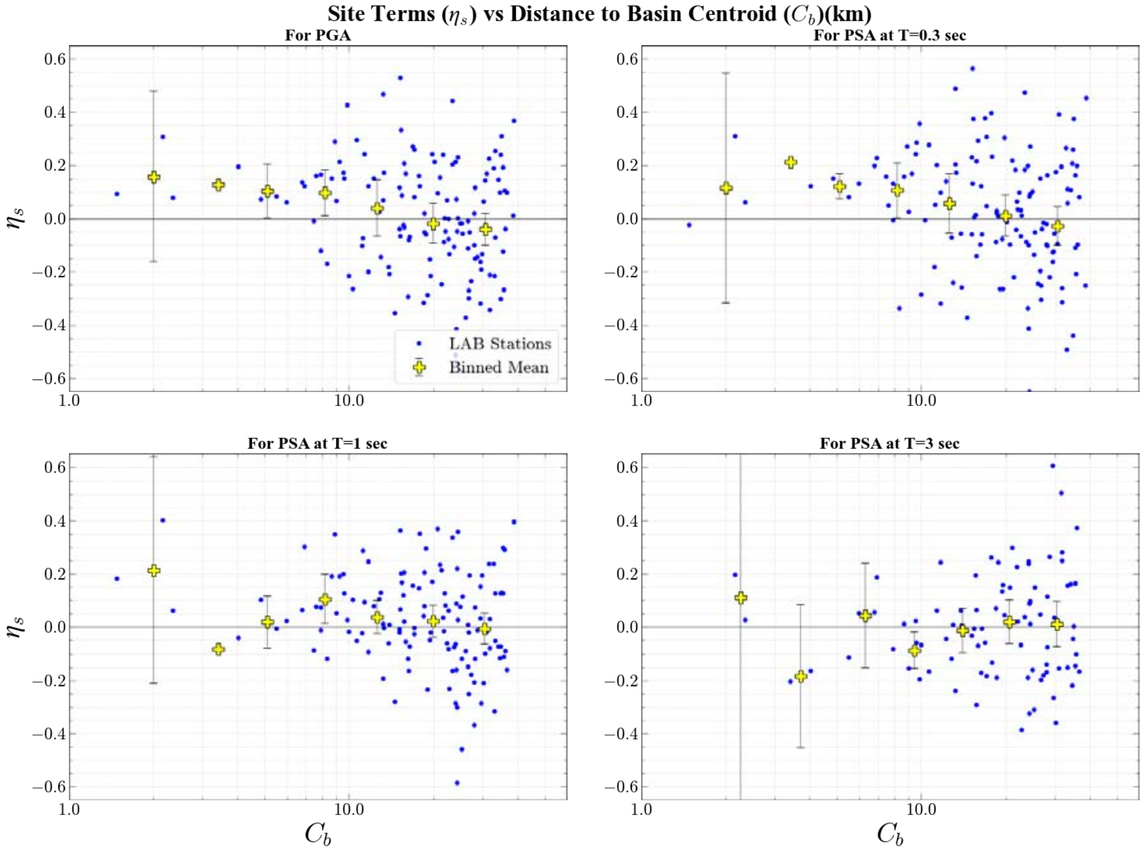

Figure 6.25: Site Residuals (η_s) plotted with C_b (in km) for LAB (blue markers) where yellow markers are binned means for LAB sites.

However, several limitations should be considered. The effectiveness of C_b may vary for differently shaped basins, with different efficacies expected for different elongation and aspect ratios. Additionally, C_b does not account for variations in basin depth or edge effects, which may be significant factors in site response. The definition of the basin centroid can also be challenging for complex basin geometries and may affect the parameter's performance. In Chapter 8, we will develop models using C_b to explore its potential in improving site response predictions, particularly for low to intermediate period motions in basin environments.

6.10 Additional Geometric Parameters

In our quest to capture complex basin effects, we explored several additional geometric parameters beyond those previously discussed. These parameters include the Slope of Velocity Iso-surface within a Basin (θ_{z_x}, where $x = 1.0$, 1.5, 2.3, or cb), Distance from Steepest Basin-Bedrock Contact (R_{bbc}), Aspect of z_{cb}, Closest Distance from River (R_r), and Closest Distance from a seismic discontinuity/fault (R_f). Each of these parameters aimed to quantify different aspects of basin geometry that might influence seismic response.

θ_{z_x} was calculated for the z_{cb}, $z_{1.5}$, and $z_{2.3}$ surfaces, representing the gradient of the impedance contrasts interfaces. We hypothesized that areas with stronger gradients might correlate with amplification patterns. R_{bbc} measured the distance from each site to the point of maximum slope within a 2 km radius, potentially capturing near-site variability effects. The Aspect of z_{cb} identified the variability of the orientation of the crystalline basement interface, which we thought might relate to directional site effects. R_r and R_f measured the proximity of sites to major rivers and faults, respectively, based on the assumption that these features might influence local site response.

Despite the theoretical basis for each of these parameters, our analysis revealed that none showed significant predictive power for site response when examined against the full model-derived site terms. Figures 6.26-6.36 illustrate the relationships between these parameters and site terms (η_s) for different spectral periods. In all cases, we observed no clear trends or patterns that would suggest these parameters capture site effects beyond what is already accounted for by conventional parameters like V_{S30} and basin depth.

The lack of predictive power in these parameters underscores the complexity of basin effects and the challenge of capturing them with simple geometric measures. It also highlights the robustness of existing parameters in accounting for many aspects of site response. However, the exploration of these parameters provides valuable insights into the nature of basin geometry and its relationship to seismic response. These findings suggest that future efforts to improve site response predictions in basin environments may need to focus on more complex, multi-dimensional parameters or combinations of parameters. Alternatively, they may need to consider dynamic properties of the basin beyond static geometric measures.

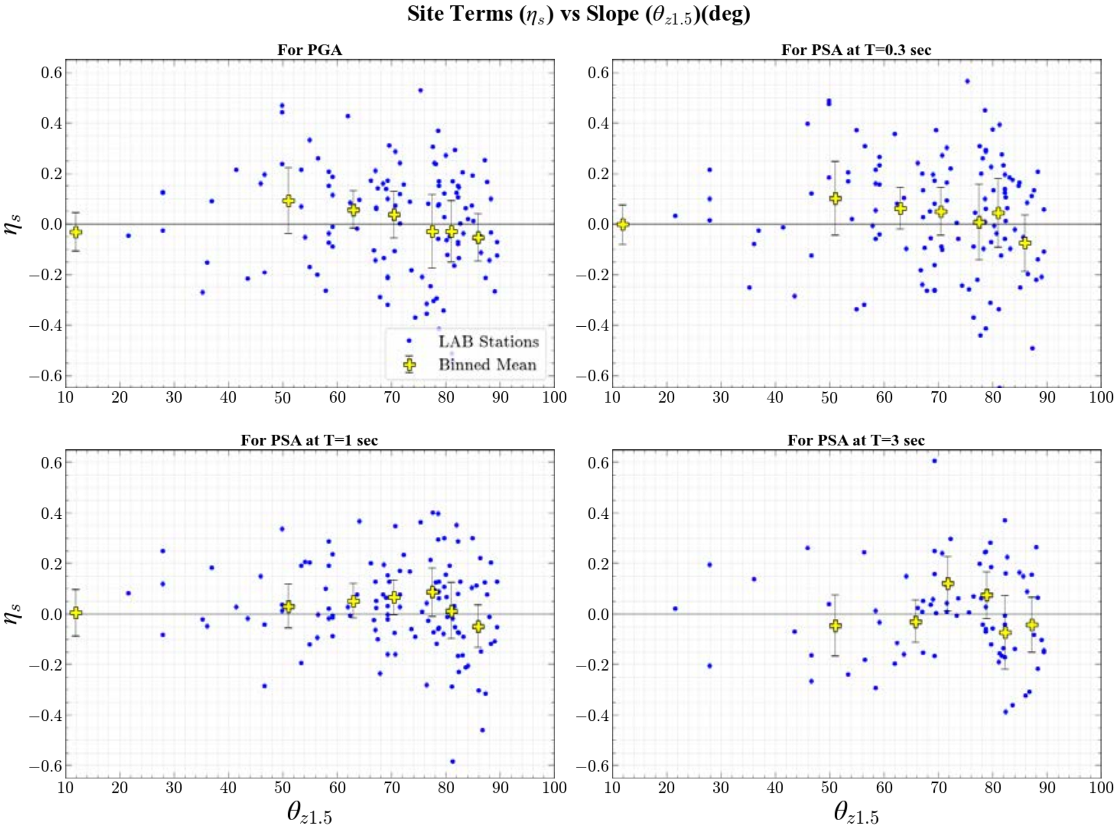

Figure 6.26: Slope of $z_{1.5}$ plotted against site terms (η_s).

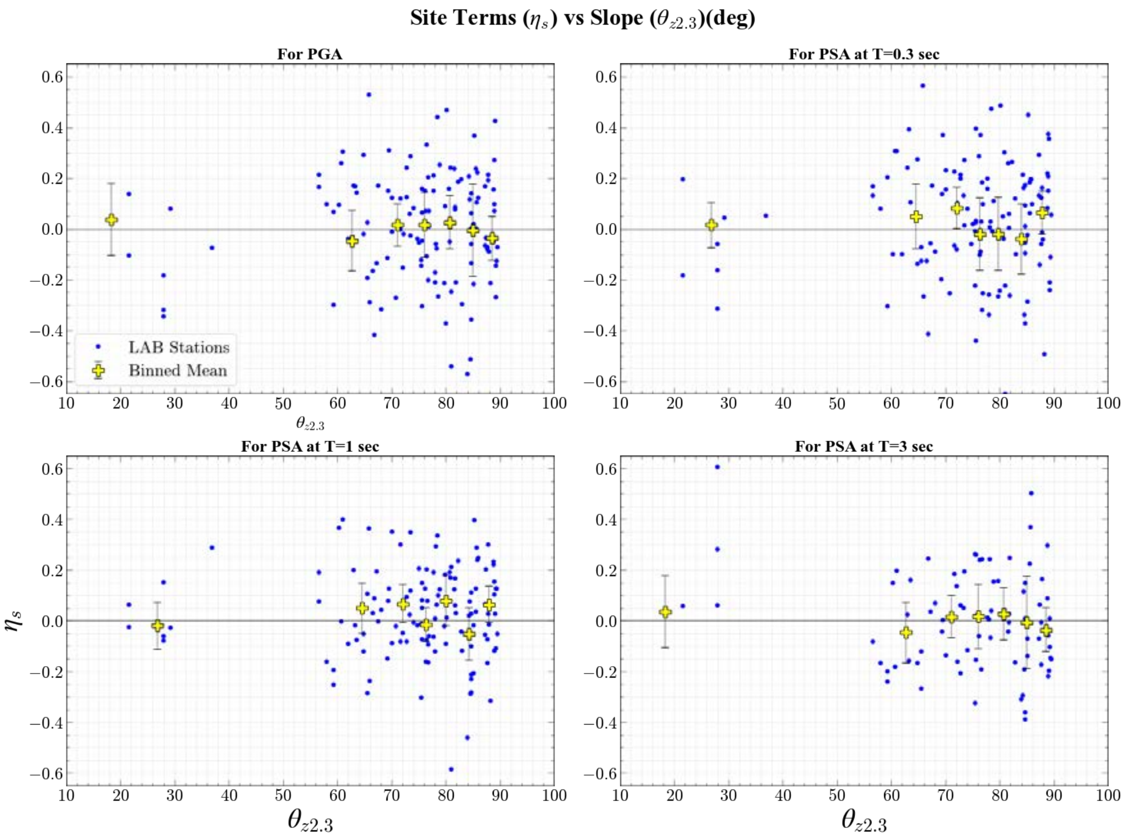

Figure 6.27: Slope of $z_{2.3}$ plotted against site terms (η_s).

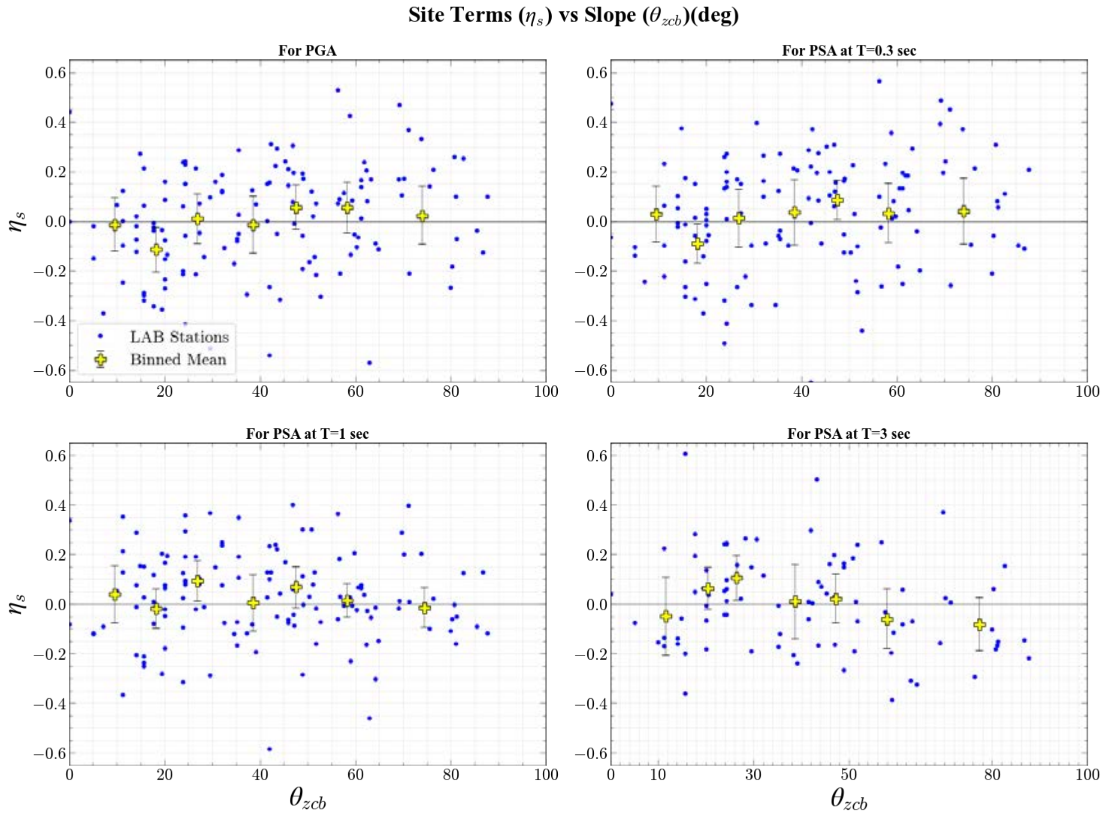

Figure 6.28: Slope of z_{cb} plotted against site terms (η_s).

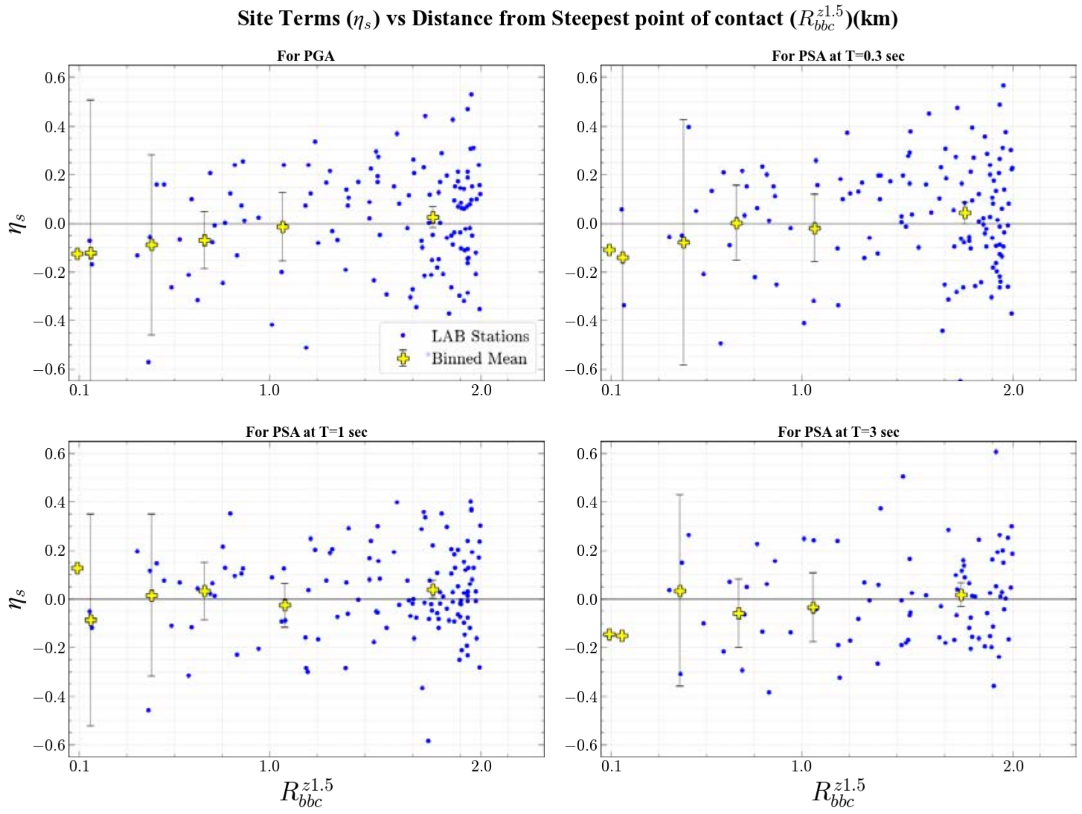

Figure 6.29: Site Residuals (η_s) plotted with $R^{z1.5}{}_{bbc}$ for LAB (blue markers) where yellow markers are binned means for LAB sites.

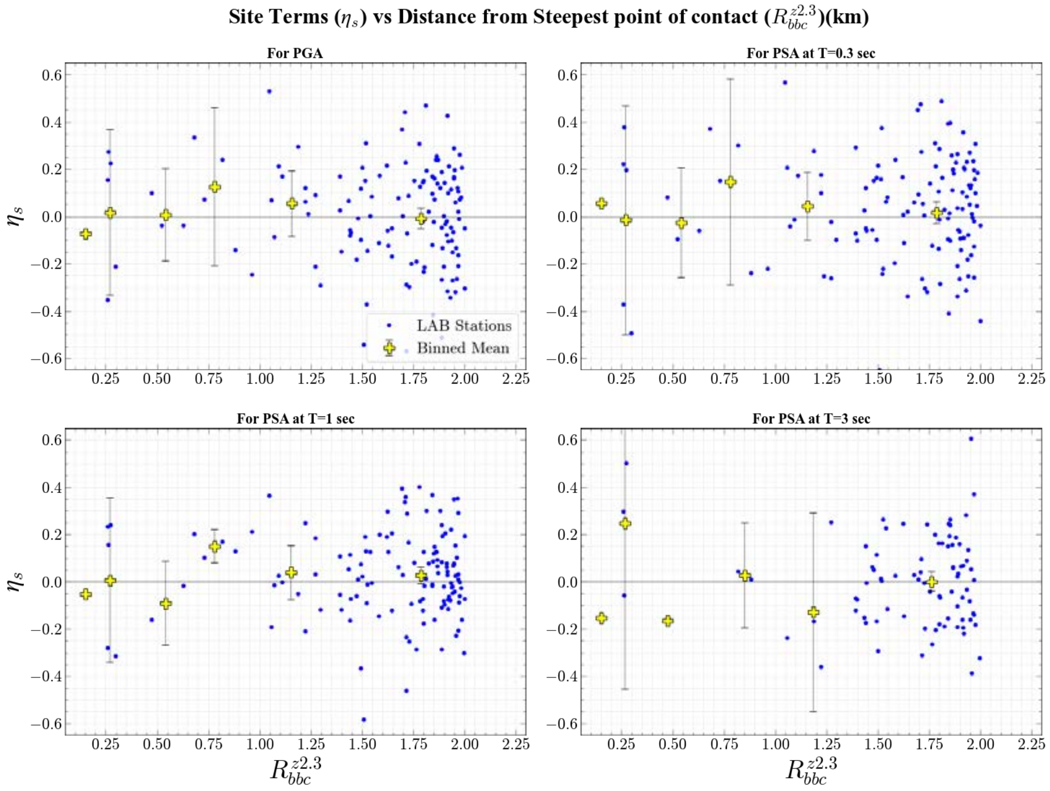

Figure 6.30: Site Residuals (η_s) plotted with $R^{z2.3}{}_{bbc}$ for LAB (blue markers) where yellow markers are binned means for LAB sites.

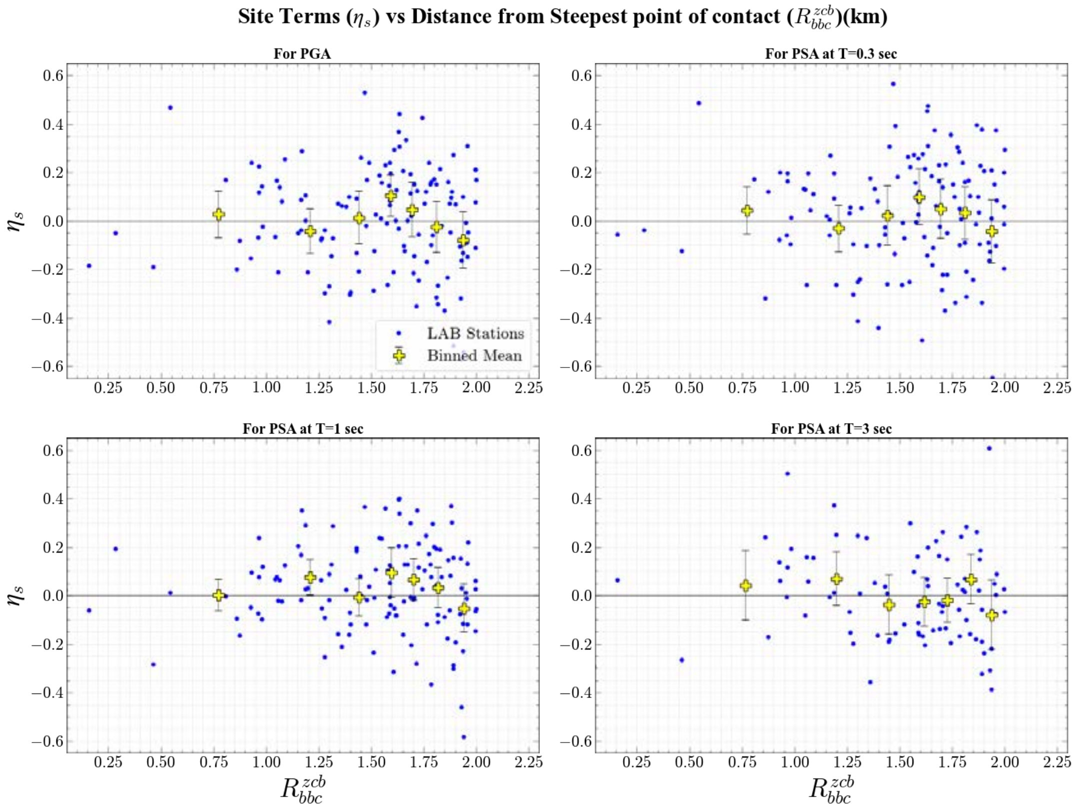

Figure 6.31: Site Residuals (η_s) plotted with $R^{zcb}{}_{bbc}$ for LAB (blue markers) where yellow markers are binned means for LAB sites.

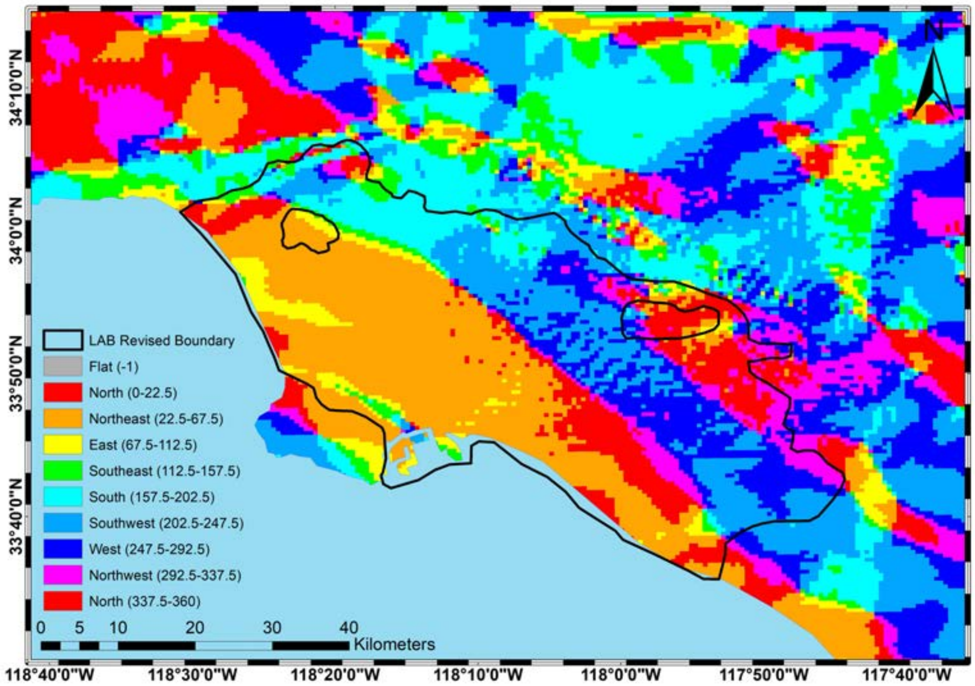

Figure 6.32: Map shows Aspect of z_{cb} where black outline represents LAB boundary.

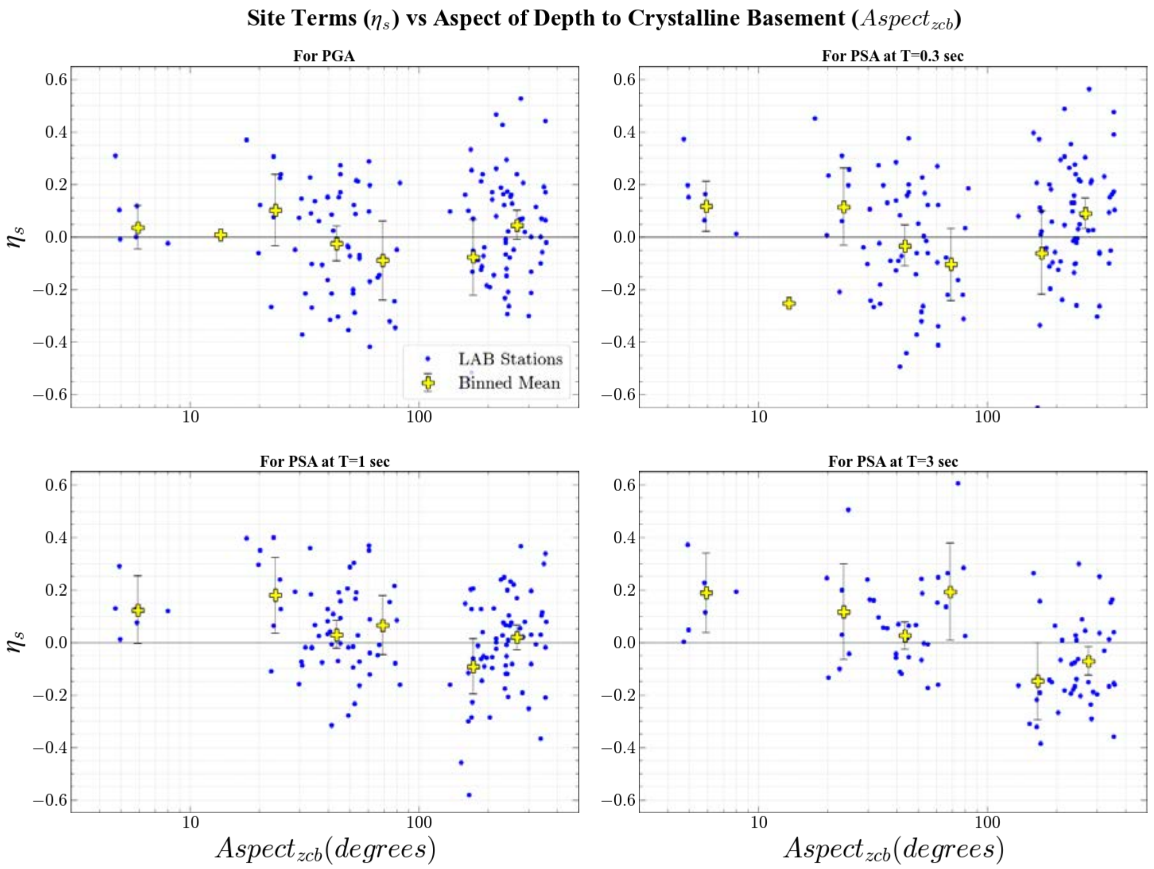

Figure 6.33: Site Residuals (η_s) plotted with Aspect of z_{cb} for LAB (blue markers) where yellow markers are binned means for LAB sites.

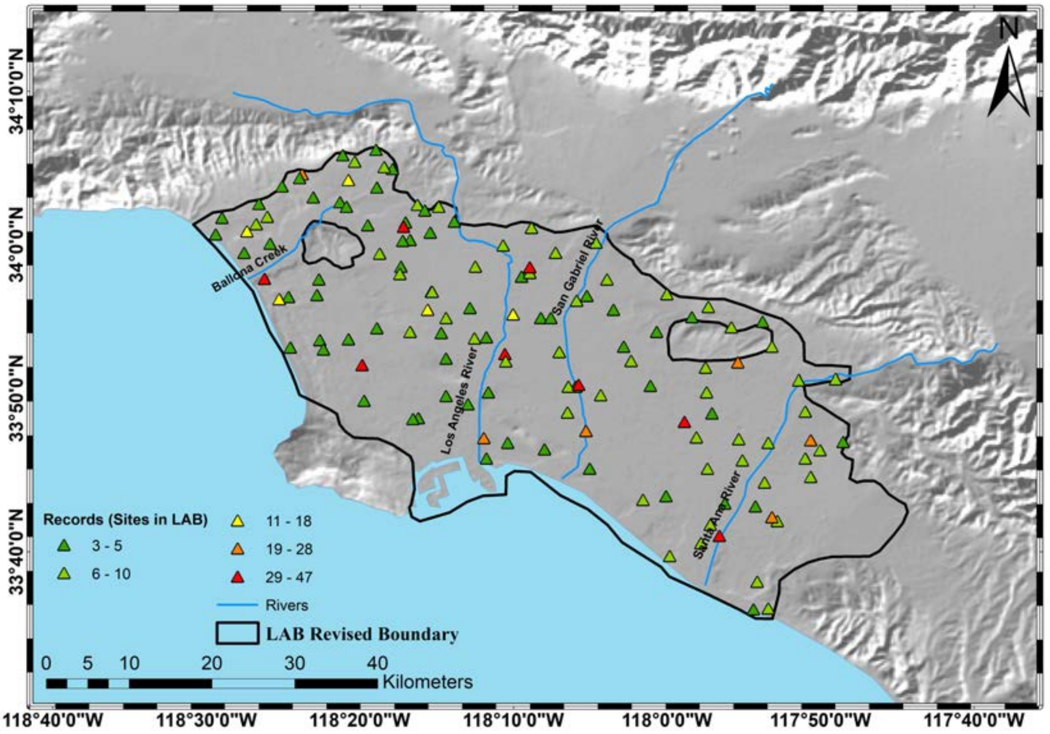

Figure 6.34: Map shows major drainage channels in LAB with sites under investigation (coloured by number of recordings).

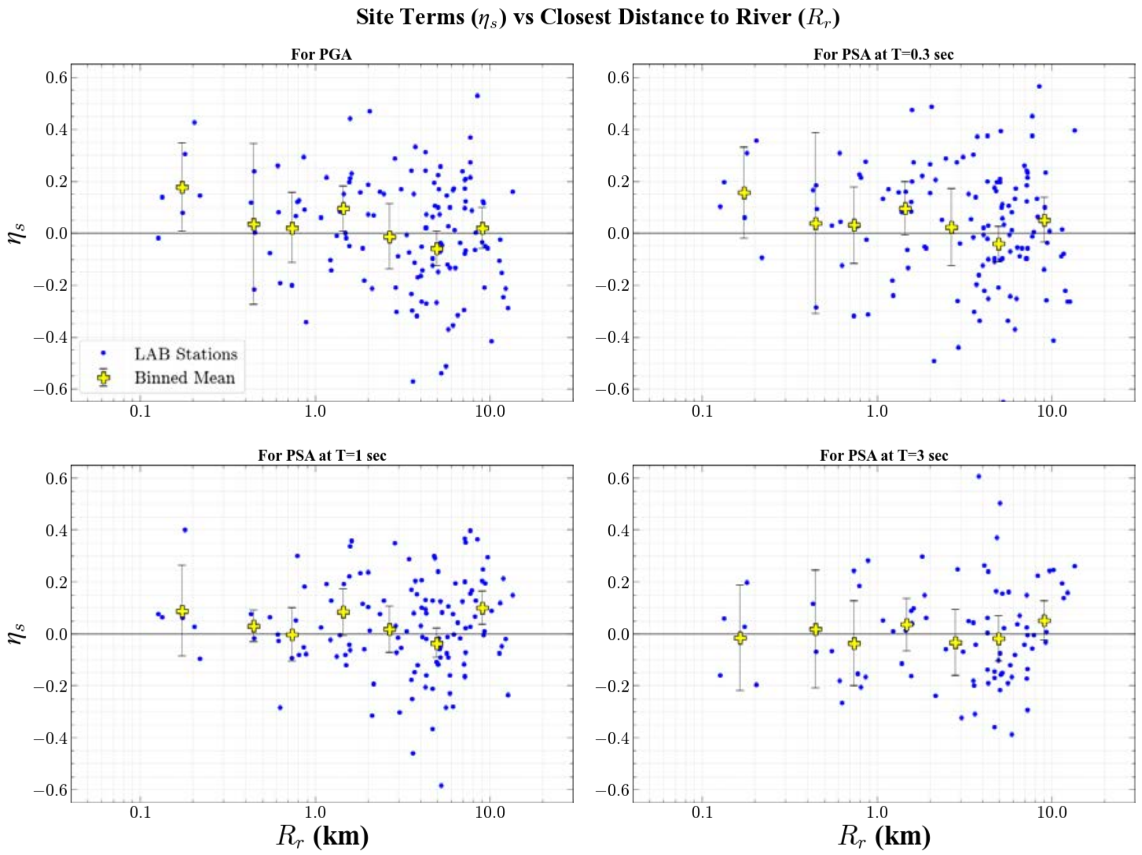

Figure 6.35: Site Residuals (η_s) plotted with R_r for LAB (blue markers) where yellow markers are binned means for LAB sites.

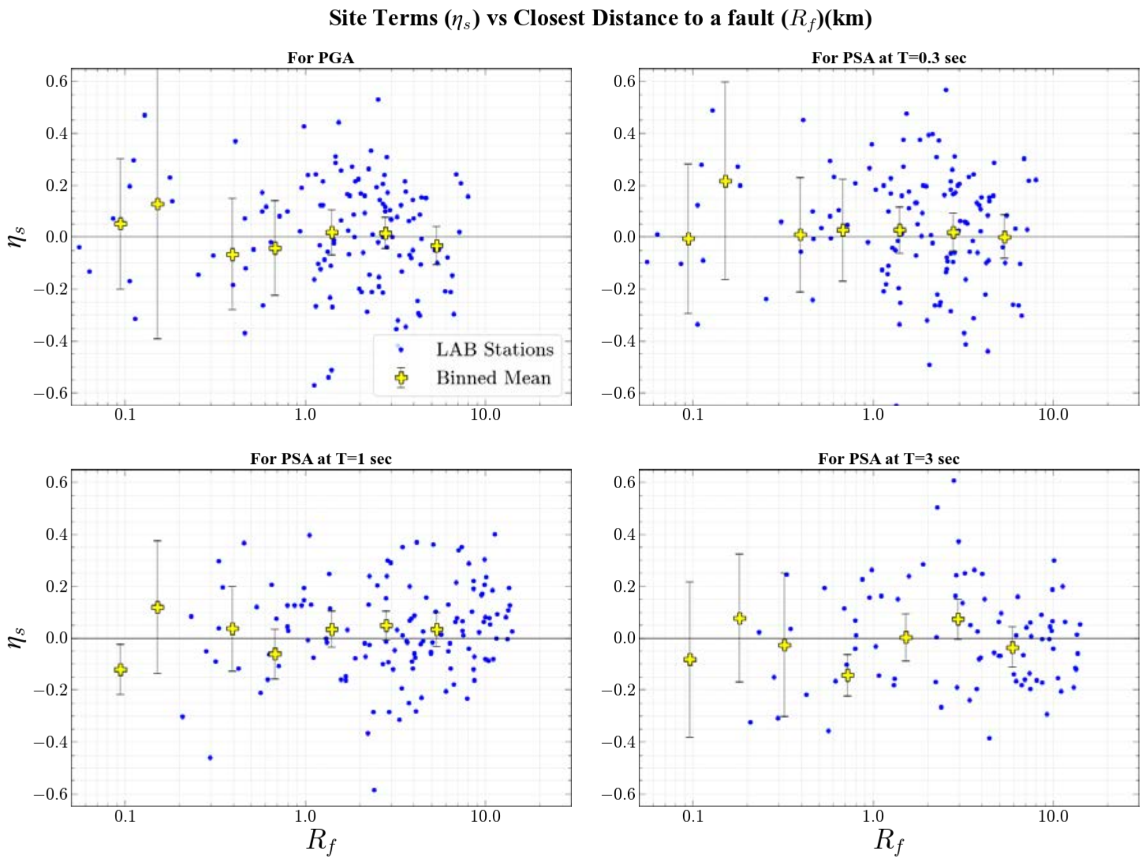

Figure 6.36: Site Residuals (η_s) plotted with R_f in km for LAB (blue markers) where yellow markers are binned means for LAB sites.

Chapter 7: V_{S30}-Scaling Models for Sedimentary Basins in Southern California (SoCal)

7.1 Introduction

Ground Motion Models (GMMs) typically employ V_{S30}-scaling relationships to capture site response across diverse geological conditions (Seyhan and Stewart 2014; SS14). However, applying a single, region-wide V_{S30}-scaling model may not fully account for the unique characteristics of individual sedimentary basins. This chapter investigates potential discrepancies between basin-specific V_{S30}-scaling and the overall Southern California (SoCal) V_{S30}-scaling model, aiming to identify limitations in current GMMs and guide future improvements.

7.2 V_{S30}-Scaling Model Development Methodology

Our investigation builds upon and emulates the work of Nweke et al. (2022), which updated the V_{S30}-scaling model for SoCal. We employ a two-step linear mixed-effect regression approach to partition the reference-rock residuals (R_{ij}^{r}) and extract the within-event rock residuals (δW_{ij}^{r}) and inevitably, the reference rock site terms ($\eta_{S,j}^{r}$). This stepwise process is describe in Equation 7.1 & 7.2:

$$R_{ij}^{r} = \ln\left(Y_{ij}\right) - \left[\mu_{ln,ij}^{r} + F_{nl,ij}\right] = \eta_{E,i} + \delta W_{ij}^{r} \tag{7.1}$$

$$\delta W_{ij}^{r} = R_{ij}^{r} - \eta_{E,i} = \eta_{S,j}^{r} + \varepsilon_{ij} \tag{7.2}$$

Here, $\mu_{ln,ij}^{r}$ is the BSSA14 GMM estimate calculated using V_{S30} = 760 m/s, thus excluding site response. $F_{nl,ij}$ is the non-linear site effect model component that is removed to isolate the linear site effect (the model from SS14 is adopted), and $\eta_{E,i}$ is the event term. ε_{ij} is the remnant residual as describe in Chapter 3. This study focuses on estimating the scaling slope of $\eta_{S,j}^{r}$ binned by specific basins, extending the analysis to examine deviations from the regional scaling for individual sedimentary basins in SoCal. There are eight major sedimentary basins in southern California that have been identified by Nweke et al. (2022), which includes the Los Angeles basin (LAB), the San Fernando basin (SFB), Ventura basin (VB), San Gabriel basin (SGB), Chino basin (CB), San Bernardino basin (SBB), Coachella Valley basin (CVB), and the Imperial Valley basin (IVB). It's important to note that while the Nweke et al. (2022) model employed a trilinear form with plateaus at very low and very high V_{S30} values, our individual basin V_{S30}-scaling is constrained to a linear form due to the limited V_{S30} range within each basin. Figure 7.1 shows the comparison for PGA.

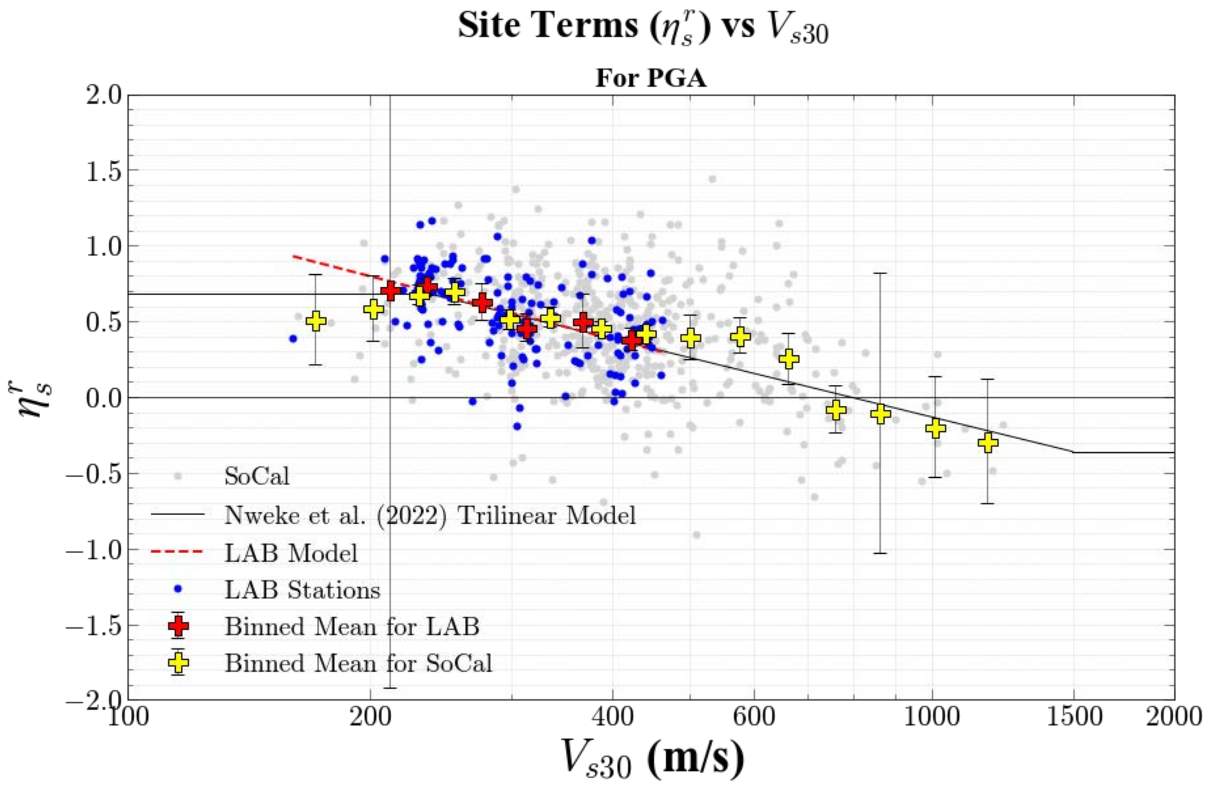

Figure 7.1: Comparison of V_{S30}-scaling model derived for LAB [dashed black line] versus the SoCal model by Nweke et al. (2022) [dotted black line] for peak ground acceleration (PGA). Gray markers represent all the sites in SoCal.

7.3 Discrepancies in V_{S30} Scaling Slopes Between Individual Basins and All SoCal Sites

Our analysis, illustrated in Figures 7.2-7.5, reveals significant variations in V_{S30}-scaling slopes between different basins and the regional SoCal model. Figure 7.2 shows the trends of V_{S30}-scaling slope with period for various site classes in SoCal (regressed with the same trilinear functional form as the regional SoCal model), providing a baseline for comparison. It can be seen from Figure 7.2 that basin and basin edge sites show stronger scaling at short periods than the regional SoCal model. Valley sites show stronger scaling at short periods and weaker scaling at longer periods than the regional. While mountain-hill sites show stronger scaling at short periods and weaker scaling at longer periods in comparison. For the individual basins, coastal basins like Los Angeles, Venture Basin and San Fernando (Figures 7.3) exhibit stronger scaling at very short and long periods compared to the regional model. In contrast, inland graben-type basins such as Chino and San Bernardino (Figures 7.4) show stronger scaling at short periods but weaker scaling at longer periods. The exception is the San Gabriel basin which shows weaker scaling at very short periods but aligns with the regional trends for all other periods. The plate boundary basins like Imperial Valley (Figure 7.5) consistently demonstrates weaker scaling across all periods, while Cochella Valley basin shows weaker scaling for long periods and stronger scaling for short periods. The Ventura basin, unlike the other coastal basins, shows a significantly stronger scaling at long periods and weaker at intermediate periods, which could be a result of the depth extents as VB is the deepest of the coastal group.

These variations highlight potential basin-specific effects not fully captured by the current regional V_{S30}-scaling model. However, it's crucial to interpret these results cautiously, considering the limited V_{S30} range within individual basins. Basins are primarily composed of softer materials, restricting the V_{S30} range and potentially leading to unrealistic scaling relationships if extrapolated beyond this range. In addition, some of these basins have a limited number of sites (ground motion recording stations) that make up the data used to regress these scaling relationships. These limitations underscore the importance of maintaining a broader, ergodic V_{S30}-scaling model while developing complementary approaches to capture basin-specific effects.

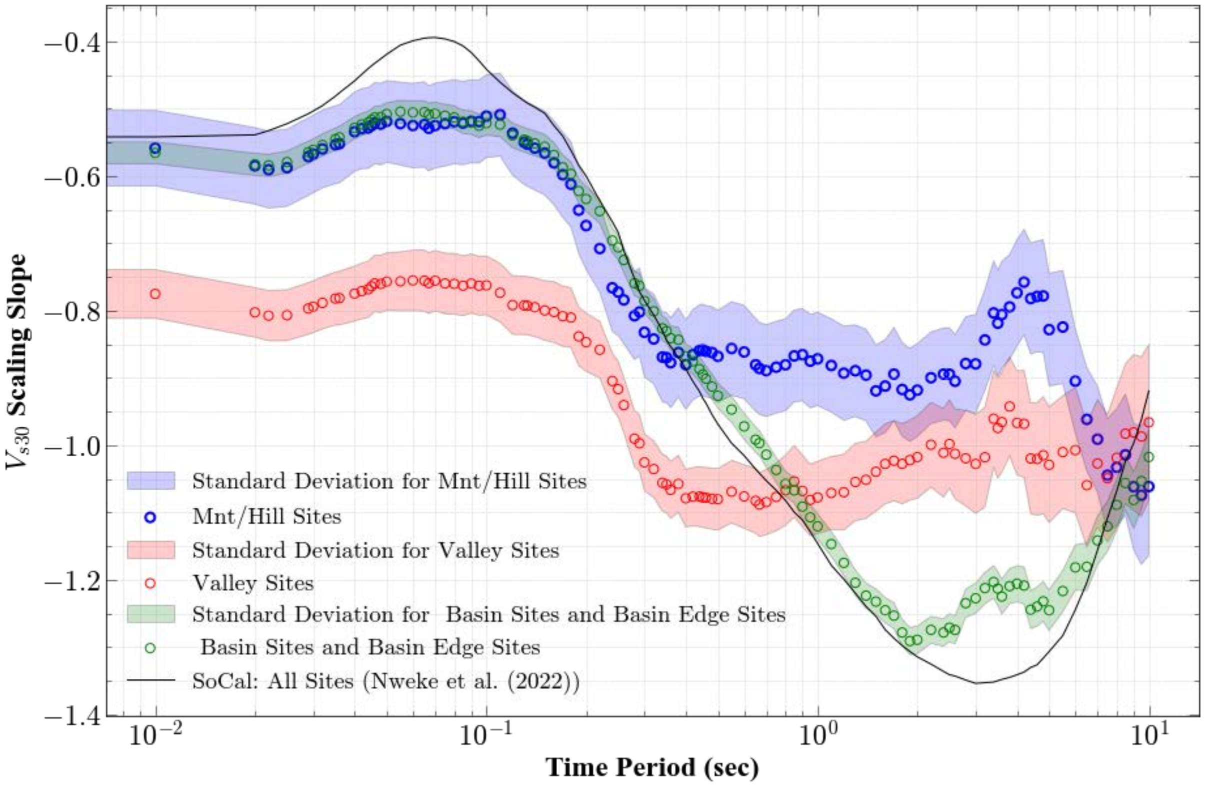

Figure 7.2: Comparison between regressed V_{S30}-Scaling relationships (slope) for different geomorphic site classes (basin, non-basin, intermediate) and the regional V_{S30}-Scaling slope for SoCal (from Nweke et al. (2022).

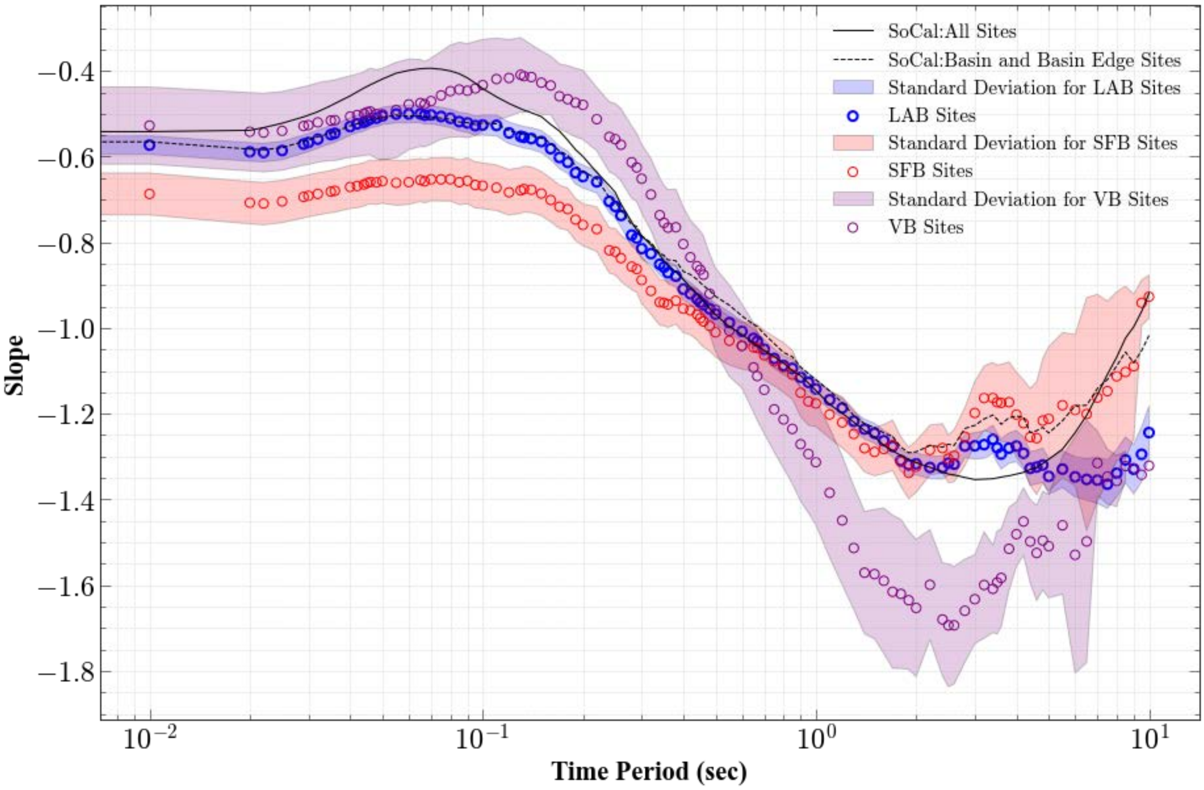

Figure 7.3: Comparison between regressed V_{S30}-Scaling relationships (slope) for the different coastal basins and the regional V_{S30}-Scaling slope for SoCal (from Nweke et al. (2022).

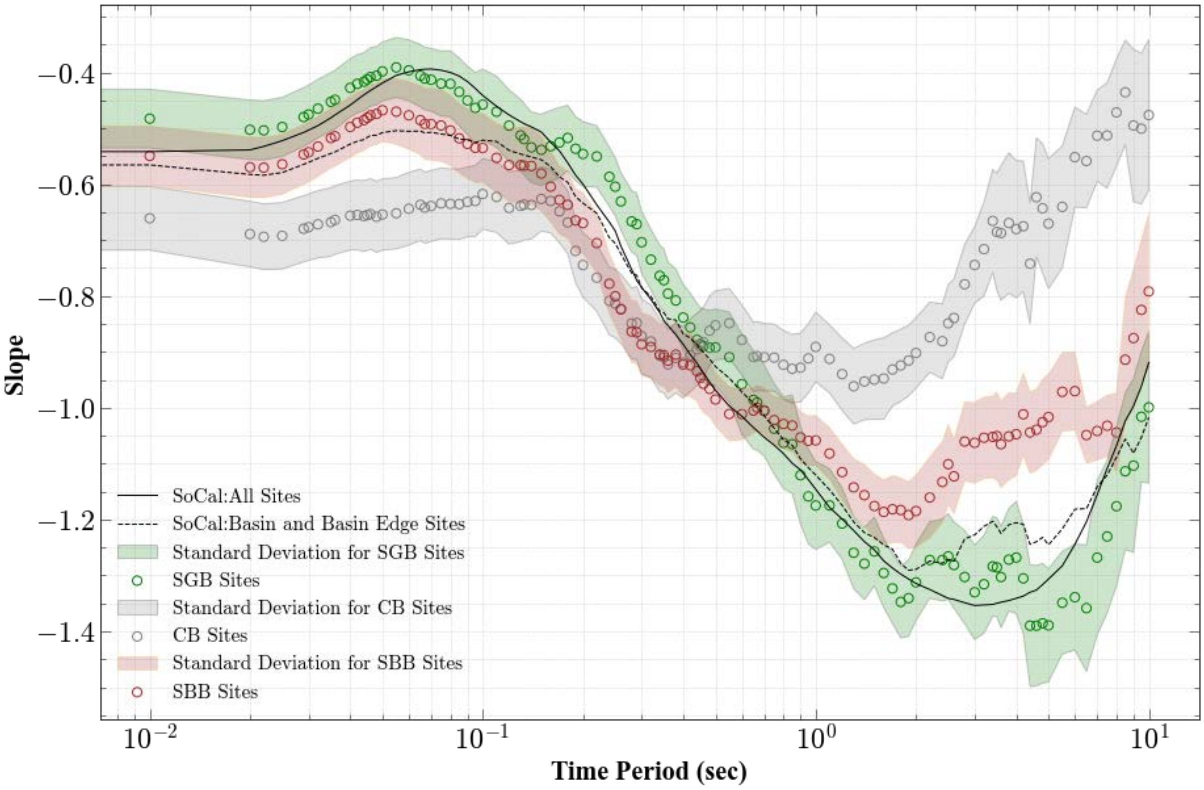

Figure 7.4: Comparison between regressed V_{S30}-Scaling relationships (slope) for the different graben-type basins and the regional V_{S30}-Scaling slope for SoCal (from Nweke et al. (2022).

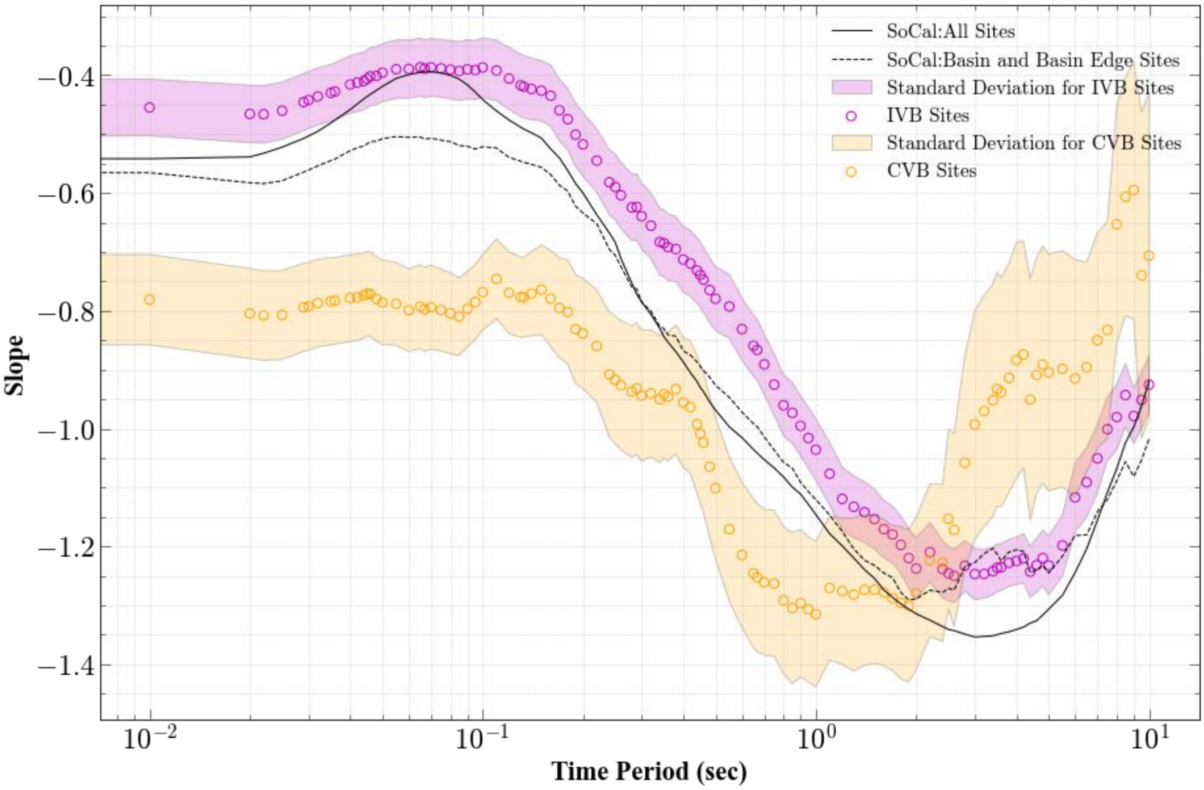

Figure 7.5: Comparison between regressed V_{S30}-Scaling relationships (slope) for the different plate boundary-type basins and the regional V_{S30}-Scaling slope for SoCal (from Nweke et al. (2022).

7.4 Implications on Developing Geometric Parameter Site Response Models

The observed discrepancies between basin-specific and regional V_{S30}-scaling underscore the complex nature of basin response. These findings suggest that current GMMs may under- or over-predict ground motions in specific basins due to unaccounted basin effects. Additionally, some basin-specific features may be partially captured by V_{S30}-scaling, potentially leading to double-counting when combined with other basin parameters in GMMs. To address these issues, future research should focus on:

1. Developing complementary basin parameters that capture the observed variations without compromising the broad applicability of V_{S30}-scaling.
2. Investigating the physical mechanisms behind basin-specific V_{S30}-scaling differences to inform more comprehensive basin models.
3. Exploring non-ergodic approaches that can account for basin-specific effects while maintaining robust performance across diverse geological settings.

This chapter highlights the limitations of applying a single V_{S30}-scaling model across diverse basin environments. While developing basin-specific V_{S30}-scaling is not a viable solution due to limited V_{S30} ranges and data points within individual basins, the observed variations provide valuable insights for refining GMMs. By identifying discrepancies between basin-specific behavior and the overall model, we can guide the development of more nuanced, physics-based approaches (parameters) to capture basin effects in seismic hazard assessment. In the subsequent chapter, we will build upon these findings to develop and evaluate new geometric parameters. These parameters will aim to complement the existing V_{S30}-scaling and basin models, addressing the basin-specific variations observed in this analysis. By incorporating these insights, we hope to enhance the accuracy and reliability of ground motion predictions in complex basin environments, ultimately improving seismic hazard assessments in these challenging geological settings.

Chapter 8: Modelling and Evaluation of Model Performance

8.1 Modeling of Geometric Parameters

Based on the comprehensive assessment of parameters conducted in Chapter 6, five geometric parameters initially showed promise. These parameters were the ones that exhibited some semblance of a 2D description of subsurface variations, and came from the "depth-related", "surface-related", and "distance/shape-related" parameter categories. Three of these demonstrated notable predictive power relative to the full site response model (V_{S30}-, basin depth-, and basin category-adjusted site terms; Nweke et al. 2022). These include the Standard Deviation of z_{cb} (SD_{zcb}), Spatial Area of Influence based on V_{S30} (SAI_{VS30}), and Standard Deviation of Absolute Difference between $z_{1.5}$ and z_{cb} ($SD_{|zcb-z1.5|}$). Out of these three, only SAI_{VS30} is applicable to the entire SoCal domain, while the other two are confined to the LAB domain until robust resources to derive the parameters are provide for the areas outside the basin. Two additional parameters, SAI_{VS} and C_b, showed appreciable association with the adjusted site terms. However, after thorough evaluation, SAI_{VS} and C_b were not recommended for further development as they did not provide significant (if any) reduction in variability of the median GMM estimates. For the three selected parameters, we employed a second-degree polynomial functional form to represent the relationship with the uncaptured site response. This choice was motivated by the observed non-linear trends in our data and the desire for a relatively simple functional form that could capture these trends without overfitting. The functional form is expressed in Equation 8.1 as:

$$F_{geom} = \mathrm{a}X_{geom}^2 + bX_{geom} + c \tag{8.1}$$

where $X_{geo}m$ represents the geometric parameter (either SD_{zcb}, SAI_{VS30}, $SD_{|zcb-z1.5|}$), a, b, & c are the model coefficients, and F_{geom} is the modeled effect on site response. We acknowledge that this choice represents a balance between simplicity and flexibility, and other functional forms may be worth exploring in future work. Figures 8.1-8.3 illustrate the relationship between site terms and each geometric parameter, along with the best-fit curves for the functional form.

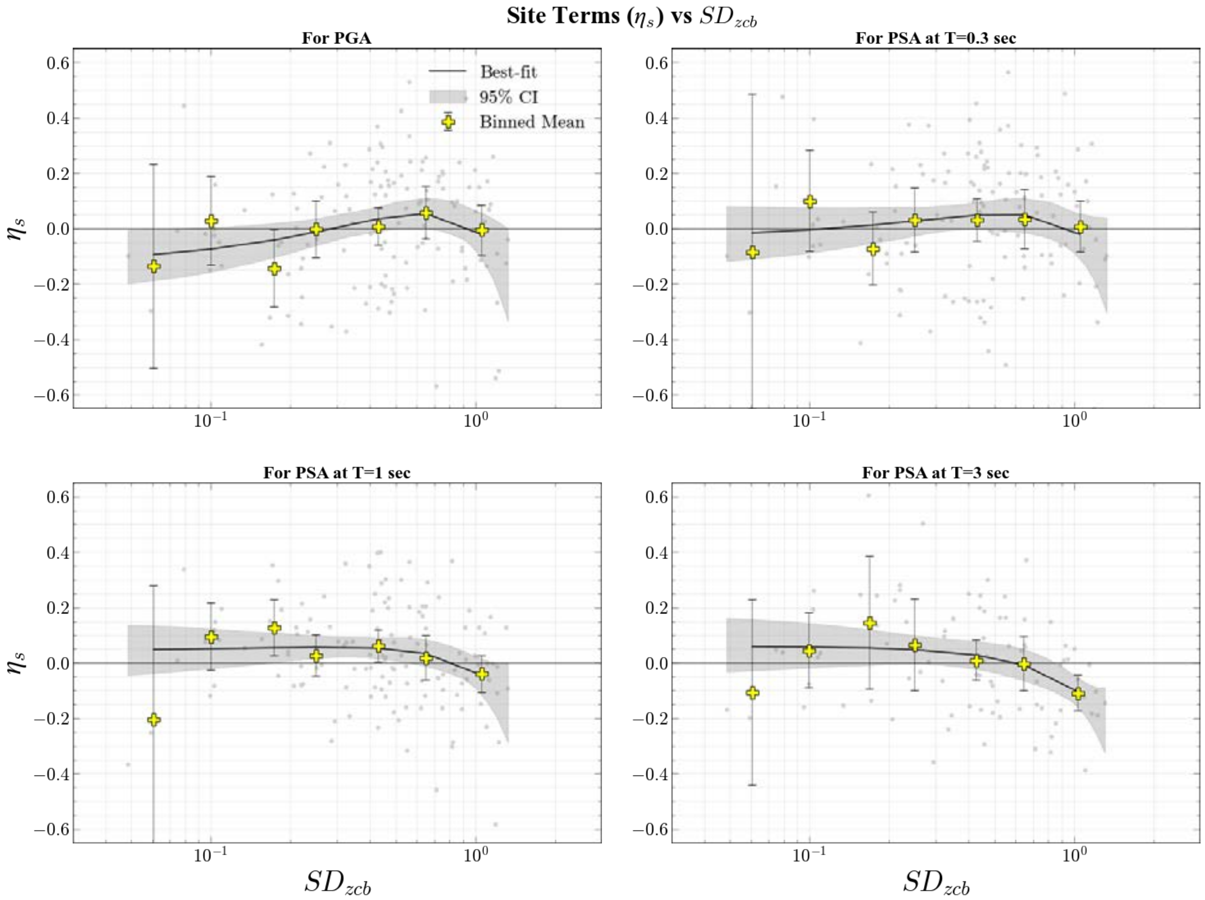

Figure 8.1: Trends of η_s as a function of Standard deviation of z_{cb} (SD_{zcb}) for LAB sites compared to the F_{geom} model fit (black lines).

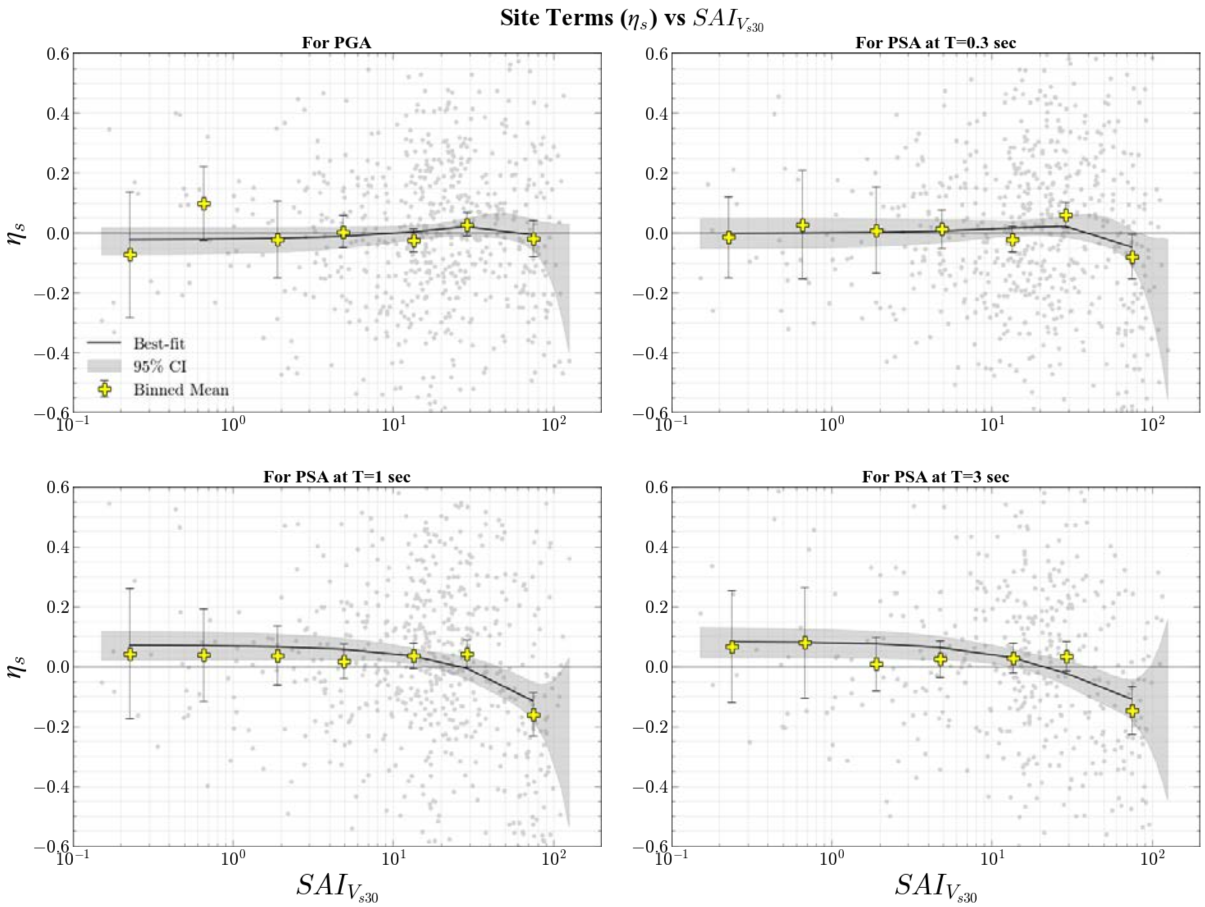

Figure 8.2: Trends of η_s as a function of SAI_{VS30} for all sites in SoCal compared to the F_{geom} model fit (black lines).

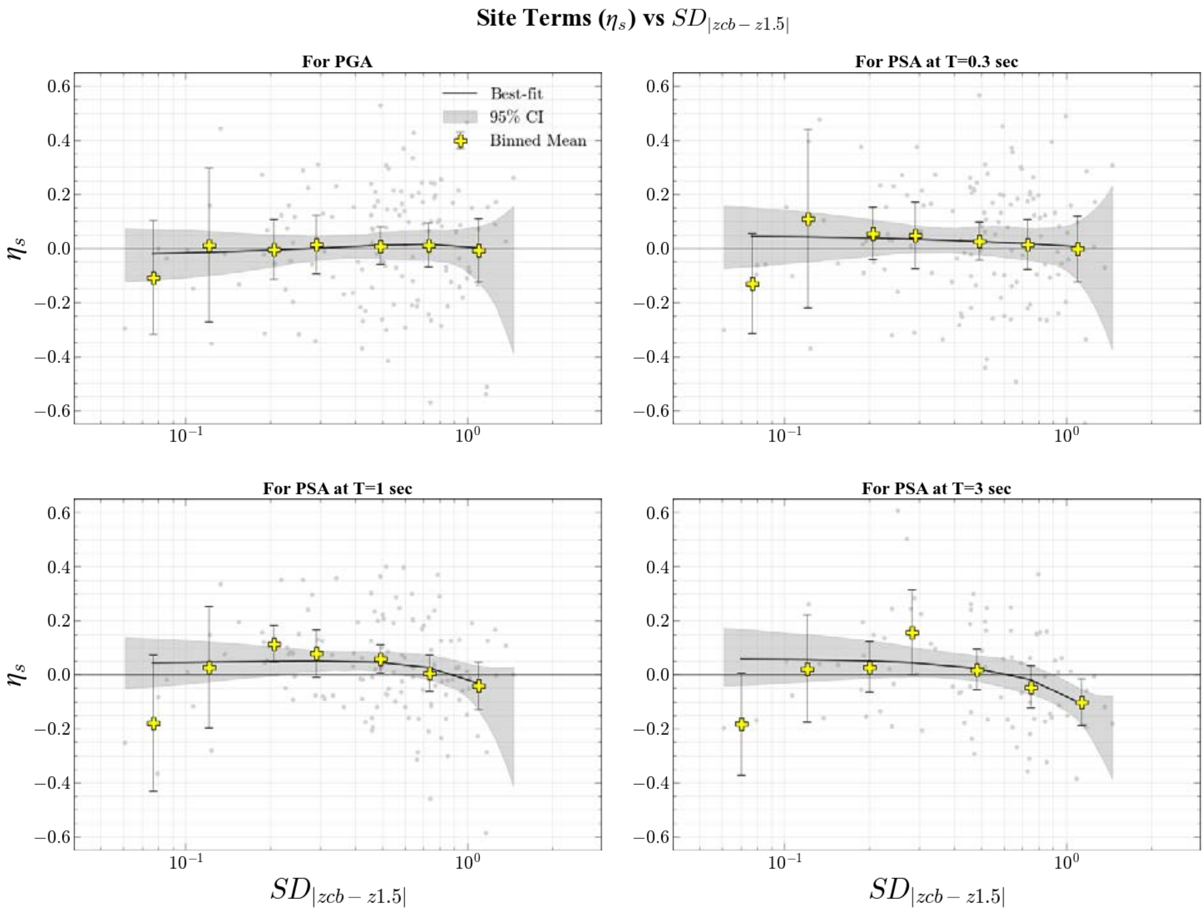

Figure 8.3: Trend of η_s as a function of $SD_{|zcb\text{-}z1.5|}$ for LAB sites compared to the F_{geom} model fit (black lines).

These figures reveal distinct patterns for each parameter at short to intermediate periods (T < 0.4 sec), and similar patterns at longer periods (T > 1 second). SD_{zcb} and $SD_{|zcb\text{-}z1.5|}$ show discernible positive associative relationships with uncaptured site response that plateaus for higher dependent variable values at short to intermediate periods, while SAI_{VS30} exhibits weak to no scaling for those same periods of intensity measure. At longer periods, all three parameters display constant positive bias that decays to a negative bias at higher dependent variable values. The polynomial fits appear to capture the general trends in the data, but there is noticeable scatter, particularly for extreme parameter values. This is supported by the range of the 95% confidence intervals, which is shown by grey coloured region. Figure 8.4 presents the coefficients (a, b, c) for each parameter model across different periods.

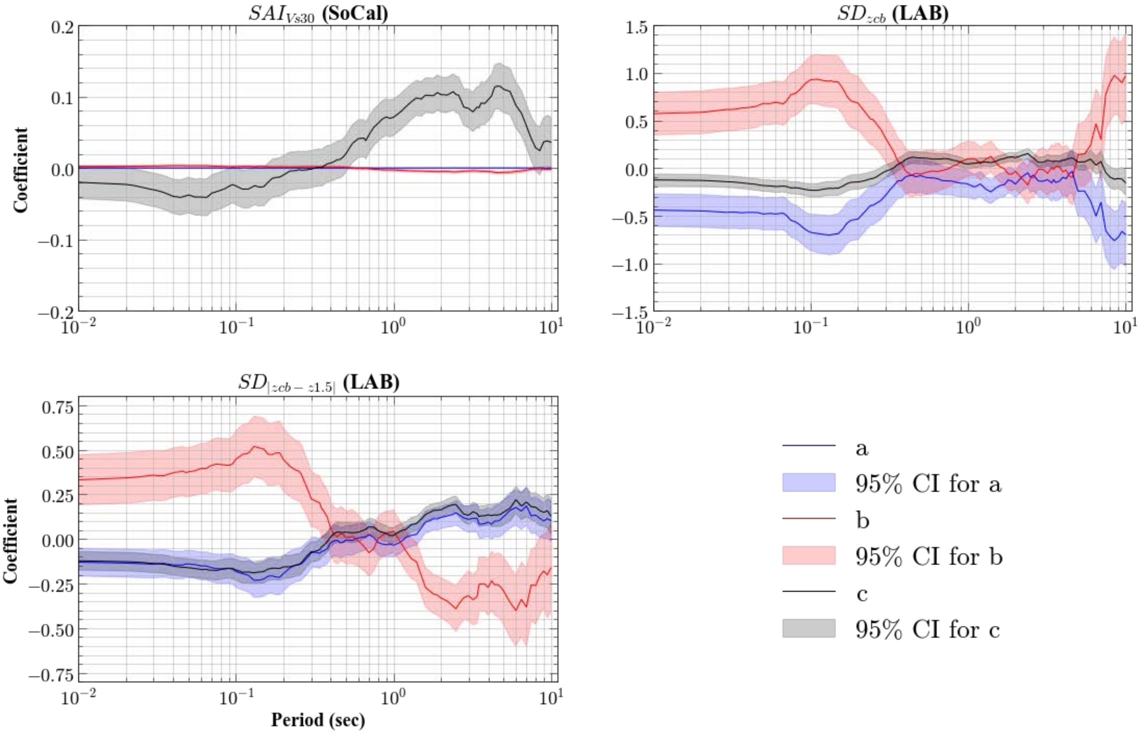

Figure 8.4: Trends of the F_{geom} model coefficients (a, b, & c) for three geometric parameters.

The variation in coefficients across periods indicates that the influence of these geometric parameters on site response is frequency dependent. However, the physical interpretation of these coefficients is not straightforward and warrants further investigation. While our modeling approach provides a consistent framework for all parameters, it has limitations. For instance, the polynomial form may not fully capture/represent the complete underlying physical processes, particularly at the extremes of parameter ranges. In subsequent sections, we will evaluate the performance of these models when incorporated into existing ground motion prediction equations. This evaluation will provide insights into the effectiveness of our modeling approach and guide future refinements. Future work should consider alternative modeling approaches, explore the physical basis of the observed relationships, and quantify model uncertainties to enhance the robustness of these geometric parameter models.

8.2 Performance Evaluation Methodology for the Geometric Parameter Model

To assess the effectiveness of our newly developed geometric parameter models, we will employ a systematic approach for their evaluation. This methodology aims to provide a quantitative representation of the improvements that were qualitatively observed in Chapter 6, measuring the enhancement these parameters bring to ground motion predictions when incorporated into existing Ground Motion Models (GMMs). The evaluation will be based on the Nweke et al. (2022) updated BSSA14 GMM. Our performance evaluation will proceed as follows:

1. Incorporation into GMM - We will integrate each geometric parameter model into the site component of the GMM. This integration will take the form:
   $$Site\ Amplification = f(V_{S30}, z_{1.0}, basin\ category), +F_{geom} \quad (8.2)$$
   Where $f(parameters)$ is the current site response model, and F_{geom} represents the contribution of the geometric parameter model.
2. Residual Analysis - Using the methodology described in Chapter 3, we will perform a comprehensive residual analysis on the site response-modified GMM. This analysis

will allow us to compute new site terms (η_S^{geom}) that account for the geometric parameter's contribution.

3. Trend Analysis - We will examine the relationship between the geometrically adjusted site terms (η_S^{geom}) and the respective geometric parameters. This analysis will help us determine if the incorporation of the geometric parameter has reduced or eliminated trends that were present in the original site terms.
4. Quantitative Metrics - We will calculate several quantitative metrics to measure the performance improvement:
   - Reduction in mean site terms
   - Decrease in site-to-site variability (ϕ_{S2S})
   - Changes in within-event standard deviation (ϕ)

This systematic evaluation will provide a comprehensive understanding of each geometric parameter's contribution to improving site response predictions.

8.3 Incorporation of Geometric Parameter Model in Residual Analysis

Building upon the methodology outlined in Section 8.2, we now detail the process of incorporating our geometric parameter models into the existing Ground Motion Model (GMM) and the subsequent residual analysis. The Nweke et al. (2022) update of the BSSA14 GMM is comprised of three parts: (1) the source component, F_E; the path component, F_P; and the site component, F_S. These three portions are combined to get the median estimate of the ground motion intensity, μ_{ij}, at any given location, as shown in Equation 8.3:

$$\mu_{ij} = F_E(\boldsymbol{M}, F) + F_P(R, region) + F_S(V_{S30}, z_{1.0}, basin\ category) \tag{8.3}$$

Where ***M*** is the moment magnitude, *F* is the style of faulting (strike-slip, normal, reverse), *R* is the distance metric (Joyner-Boore Distance for the chosen model), and the rest are as previously defined. The integration of the geometric parameter model into the BSSA14 GMM is achieved by modifying the site component, F_S as shown in Equation 8.4:

$$F_s = F_{lin}(V_{S30}) + F_{nl}(V_{S30}, PGA_R) + F_b(z_{1.0}, basin\ category) + F_{geom}(X_{geom}) \tag{8.4}$$

Where F_{lin} is the linear V_{S30}-scaing relationship, F_{nl} is the nonlinear component of the GMM site response condition on the reference rock motion (PGA_R), F_b is the basin-effect model, and F_{geom} represents the contribution of the geometric parameter model as described in Section 8.1. This additive approach allows us to isolate and evaluate the contribution of the geometric parameter while preserving the existing site response components. This also addresses, to some extent, issues related to collinearity as the additive nature necessitates that the added model builds upon the uncaptured features of the prior model (i.e., F_{nl} augments F_{lin}, F_b augments/adjusts for features beyond what the combination of F_{lin} and F_{nl} can capture, F_{geom} augments/adjusts for features beyond what the combination of F_{lin}, F_{nl}, and F_b can capture, and so on). This emulates an implicitly imposed orthogonalization to ensure the F_{geom} term captures unique information not already accounted for by the current GMM site response model.

Following the incorporation of each geometric parameter (done separately from each other), we perform a comprehensive residual analysis using the methodology described in Chapter 3. This process involves calculating new residuals (R_{ij}^{geom}) that now feature the influence of the geometric parameters, and using mixed-effect analysis to partition these residuals to get the associated event terms ($\eta_{E,i}^{geom}$), within-event terms (δW_{ij}^{geom}) , and site terms ($\eta_{S,j}^{geom}$). The mathematical representation of this formulation is shown in Equation 8.5:

$$R_{ij}^{geom} = ln\left(Y_{ij}\right) - \mu_{ij}^{geom} = \eta_{E,i}^{geom} + \delta W_{ij}^{geom} = \eta_{E,i}^{geom} + \boldsymbol{\eta}_{\boldsymbol{S,j}}^{\boldsymbol{geom}} + \varepsilon_{ij} \tag{8.5}$$

Here μ_{ij}^{geom} is the median estimate of the GMM that has been adjusted for the influence of geometric parameters, while $\eta_{S,j}^{geom}$is bolded because it is the residual of interest that will be used to evaluate the performance of the new geometric parameter models. This will be accomplished by examining the relationship between $\eta_{S,j}^{geom}$ and the respective geometric parameter (X_{geom}) to assess if the trends observed in Chapter 6 have been reduced or eliminated. Following this task, the improvement offered by each geometric parameter will be quantified by calculating the reduction in mean site terms across different period ranges, the decrease in site-to-site variability ($\phi_{S2S,j}^{geom}$, shown in Equation 8.6 & 8.7), and the changes in witin-event standard deviation (ϕ_{ij}^{geom}, shown in Equation 8.6). Equation 8.7 shows estimation of the single station sigma (ϕ_{SS}^{geom}).

$$\phi_{ij}^{geom} = \sqrt{\phi_{SS}^{geom^2} + \phi_{S2S,j}^{geom^2}} \tag{8.6}$$

$$\phi_{S2S,j}^{geom} = std.dev.\left(\boldsymbol{\eta}_{\boldsymbol{S,j}}^{\boldsymbol{geom}}\right) = \sqrt{\frac{\sum_{j=1}^{N}\left(\boldsymbol{\eta}_{\boldsymbol{S,j}}^{\boldsymbol{geom}} - \overline{\boldsymbol{\eta}_{\boldsymbol{S}}^{\boldsymbol{geom}}}\right)^2}{N}}, N = \# \, of \, stations \tag{8.7}$$

$$\phi_{SS}^{geom} = std.dev.\left(\delta W_{ij}^{geom} - \boldsymbol{\eta}_{\boldsymbol{S,j}}^{\boldsymbol{geom}}\right) \tag{8.8}$$

In the following sections, we present and discuss the results of this analysis for each geometric parameter model. We will compare their relative performance across different spectral periods and site conditions, providing insights into which parameters offer the most substantial improvements in ground motion prediction for various scenarios. This comprehensive evaluation will allow us to assess the effectiveness of our geometric parameter models in capturing previously unaccounted site effects and guide future refinements in seismic hazard assessment for complex basin environments.

8.4 *SAI$_{Vs30}$* Geometric Model

Following the methodology outlined in Sections 8.2 and 8.3, we evaluated the performance of the Spatial Area of Influence based on *V_{S30}* (*SAI_{VS30}*) when incorporated into the BSSA14 Ground Motion Model (GMM). This analysis aims to quantify the improvements observed qualitatively in Chapter 6 and compare the parameter's effectiveness across different regions and site conditions. Figure 8.5 illustrates the relationship between *SAI_{VS30}* and the corresponding site terms ($\eta_S^{geom}\ for\ SAI_{V_{S30}}$) that was adjusted after its incorporation into the GMM. The reduction in trends (approximately zero binned means) for all periods shown compared to the original site terms trends in Figure 6.23 suggests that *SAI_{VS30}* captures some site effects not accounted for by conventional parameters.

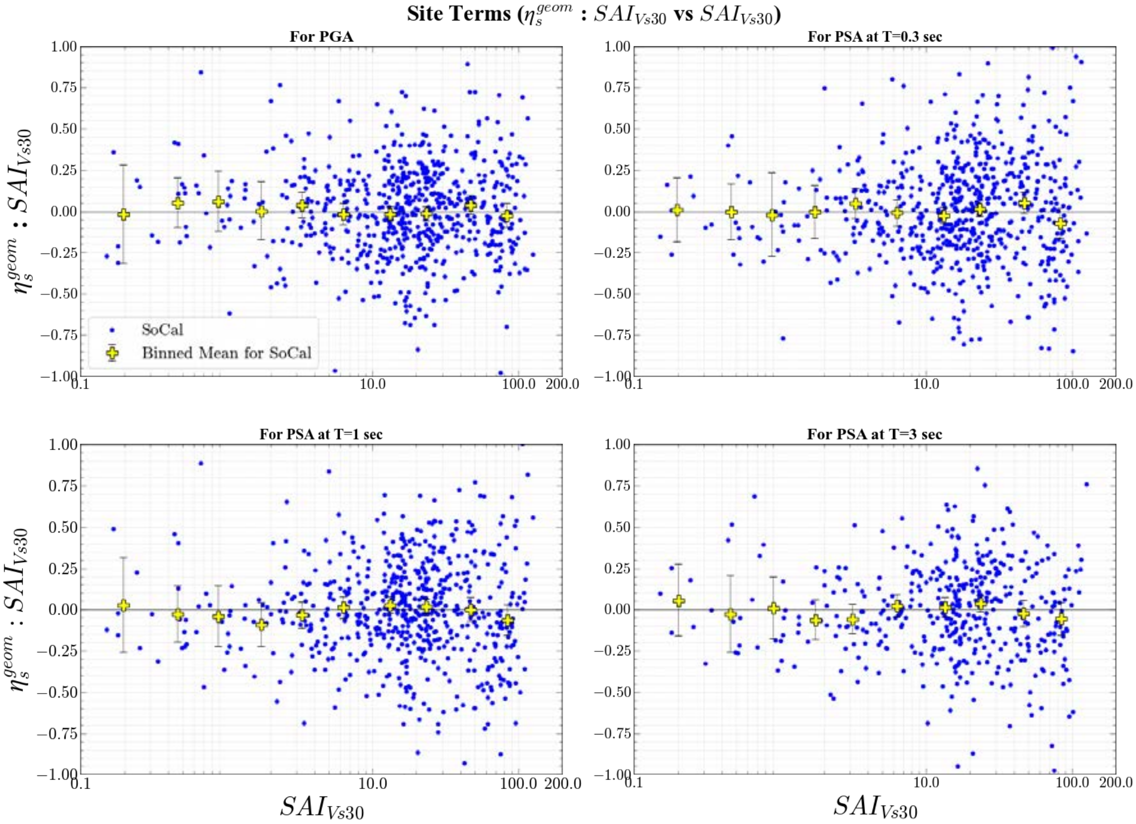

Figure 8.5: Trends of site terms (*η_S^{geom} for $SAI_{V_{S30}}$*) with $SAI_{V_{S30}}$ *obtained after incorporating $SAI_{V_{S30}}$ model in the GMM.*

Examining the mean site terms as a function of period for different site conditions (Figure 8.6), we observe a significant reduction in average bias for basin and basin edge sites in Southern California (SoCal) to the amount of 0.005 – 0.03 ln units (up to a 60% reduction in mean bias from the prior BSSA14-NEA22 GMM depending on period) when $SAI_{V_{S30}}$ is incorporated, particularly at intermediate and longer periods. Similarly, valley sites saw a bias reduction of up to 0.02 ln units (up to a 25% reduction in mean bias from the prior BSSA14-NEA22 GMM depending on period), while mountain-hill sites saw a bias reduction of up to 0.03 ln units (up to a 75% reduction in mean bias from the prior BSSA14-NEA22 GMM depending on period). As expected, this improvement is also evident for the Los Angeles Basin (LAB) specifically (Figure 8.7), exhibiting a reduction on par with the general basin and basin edge sites of up to 0.03 ln units (up to a 100% reduction in mean bias from the prior BSSA14-NEA22 GMM depending on period), indicating that $SAI_{V_{S30}}$ effectively captures remnant unresolved 2D/3D-specific site response effects. In the same vein, the fact that the bias for different site categories is approaching zero for all periods suggest that $SAI_{V_{S30}}$ is capturing more unexplained variability in the GMM estimates. This implies that it is an adequate compliment to the conventional site parameters.

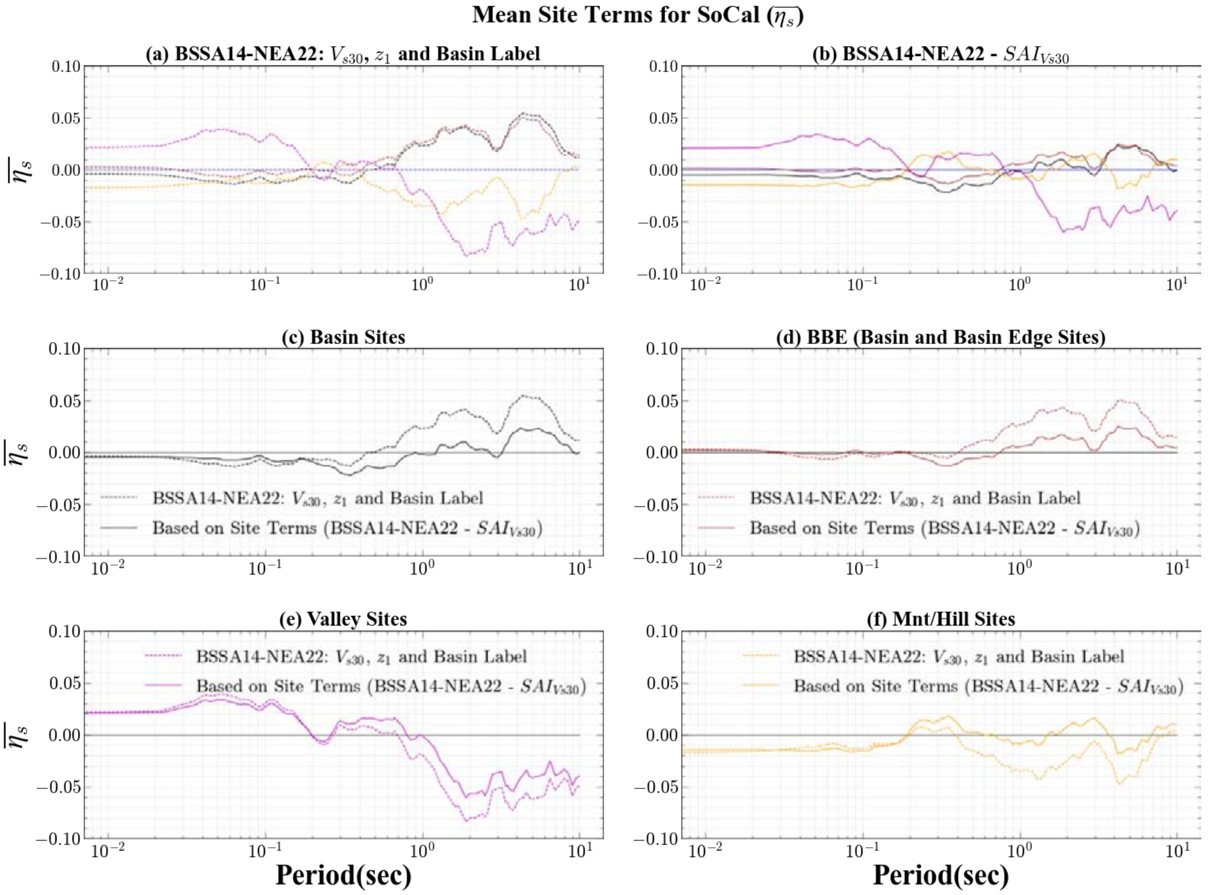

Figure 8.6: Comparison of the mean of the geometric parameter model-adjusted site terms based on $SAI_{V_{S30}}$ (η_S^{geom} $for\ SAI_{V_{S30}}$) (a) Shows the comparison *for* different site conditions using the Nweke et al. (2022) updates to BSSA14 (BSSA14-NEA22). (b) Shows the comparison for the same suite of site conditions using the geometric site model updates. (c-f) Shows the comparison between the proposed geometric site model and the current GMM site response model for the different geomorphic categories (basins, non-basins, and intermediate conditions).

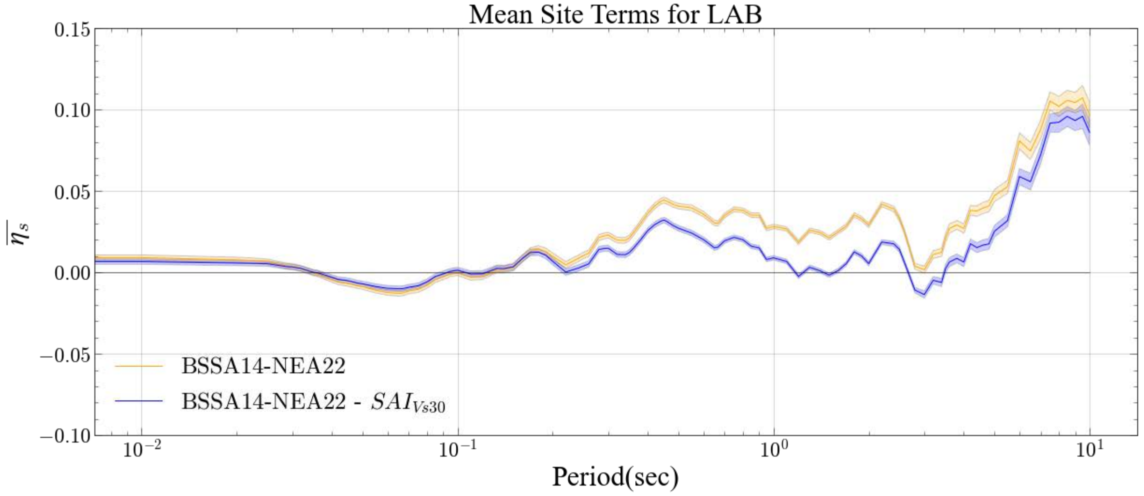

Figure 8.7: Comparison of the mean of the geometric parameter model-adjusted site terms based on $SAI_{V_{S30}}$ for the current (BSSA14-NEA22) and proposed (BSSA14-NEA22-Geom) GMM site response mode for LAB.

However, when applied to the other Southern California basins, the benefits of the geometric model were inconsistent. Figure 8.8 shows the results and the $SAI_{V_{S30}}$ site model improves the bias description in LAB, SGB, IVB, and to a much minor extent VB and SBB, but it exacerbates the bias in SFB, CB, and CVB. This may be due to efficacy of the $SAI_{V_{S30}}$ parameter, as the V_{S30} employed for some of these basins were derived from proxies and not measured, introducing potential unaccounted bias and uncertainty. In addition, some of these basins (VB, SBB, CVB, and CB have a limited number of sites that contribute enough records to be considered for this analysis, potentially impacting the robustness and quality of the achieved results.

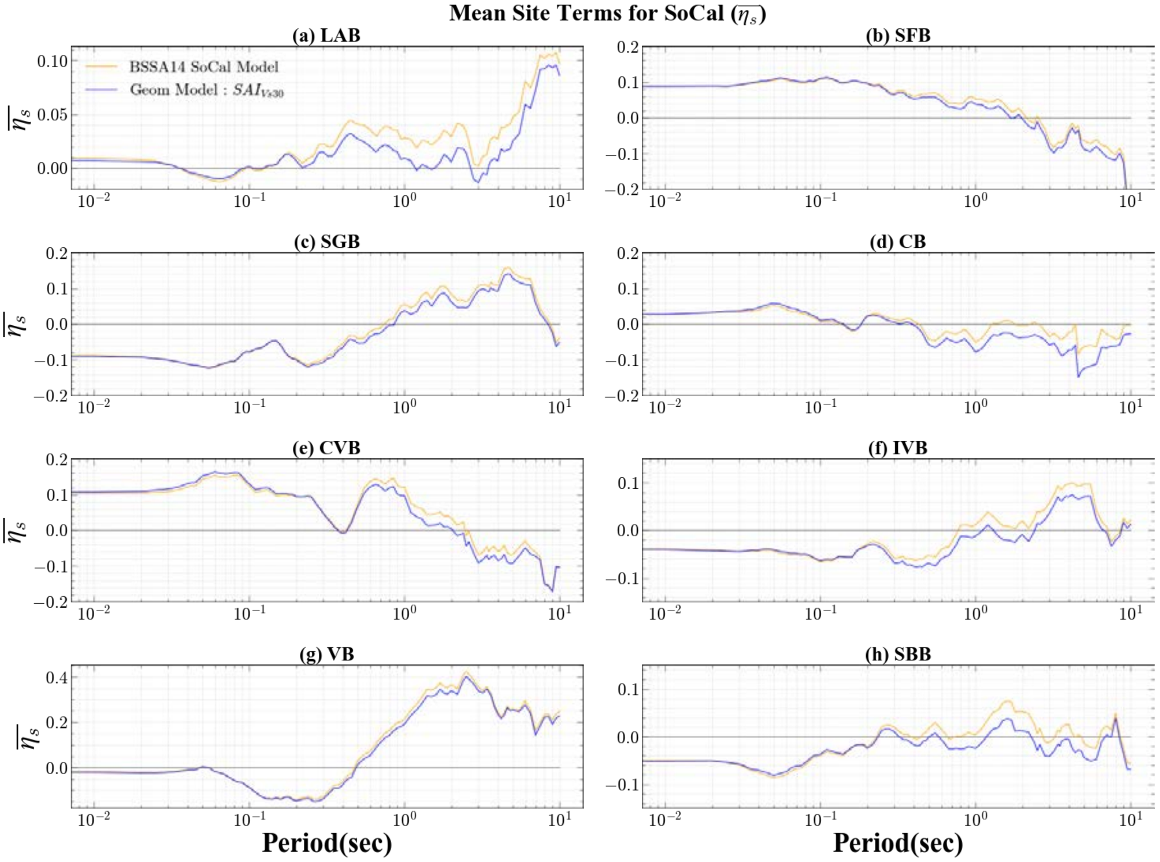

Figure 8.8: Comparison of the mean of the geometric parameter model-adjusted site terms based on $SAI_{V_{S30}}$ for the current (BSSA14-NEA22) and proposed (BSSA14-NEA22-Geom) GMM site response mode for the eight major SoCal sedimentary basins.

To evaluate the effect of $SAI_{V_{S30}}$ on dispersion of ground motion we compute site-to-site variability ($\phi_{S2S,j}^{geom}$) for both the BSSA14-NEA22 and BSSA14-NEA22-$SAI_{V_{S30}}$ model. A reduction in $\phi_{S2S,j}^{geom}$ indicates an improvement in the ability of the model to describe more complex site response features contained in the data, thereby indicating a robust GMM site response mode that approaches more non-ergodic (site-specific) formulations. Figure 8.9 shows that the incorporation of $SAI_{V_{S30}}$ leads to a reduction in site-to-site variability (φS2S) up to the amount of 0.01 ln units (up to a 3% reduction in variability from the prior BSSA14-NEA22 GMM), particularly at longer periods (T > 1 second). Interestingly, our analysis also revealed that the $SAI_{V_{S30}}$ geometric site response model performs better for valley sites (small basins) compared to large basins sites at high-intermediate to long periods. Figure 8.10 shows a maximum of 10-12% reduction for valley sites compared to a 5% reduction in dispersion for basins. Mountain-hill sites also show reductions in dispersion comparable to that basin sites.

This outcome is likely due to the ability of $SAI_{V_{S30}}$ to capture near-surface heterogeneity, which is more influential in small basins (with variations in margin condition make up and formations, i.e., different valley configurations like slender, shallow, deep-narrow, etc.). The same reasoning can be applied to non-basin sites, where in basin sites the closeness to uniformity may make the parameter partially redundant with existing basin depth terms or V_{S30} values, limiting its additional contribution.

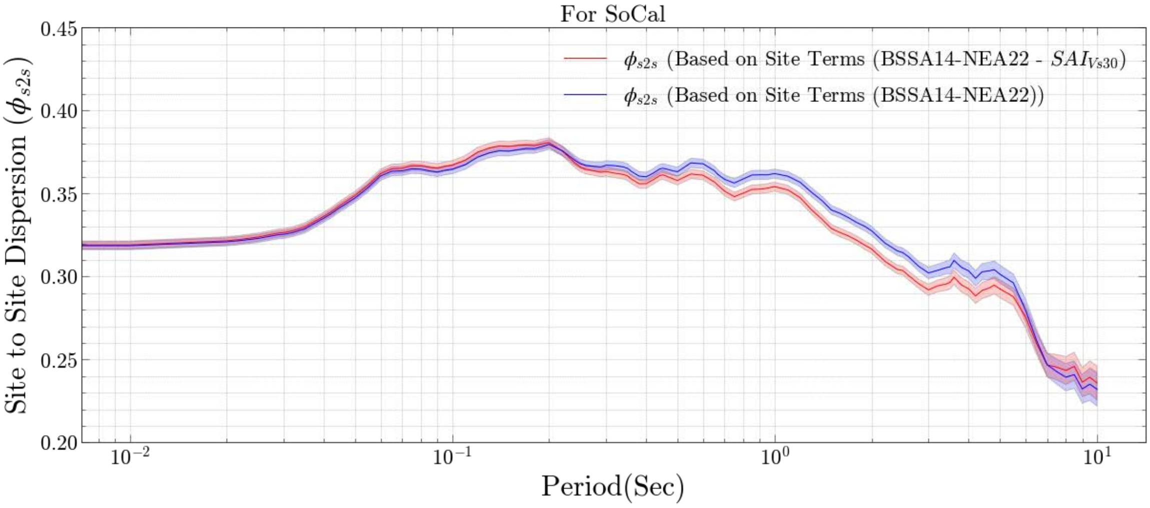

Figure 8.9: Comparison of Site-to-Site dispersion ($\phi^{geom}_{S2S,j}$) for all sites in SoCal obtained after incorporating the $SAI_{V_{S30}}$ model versus $\phi_{S2S,j}$ for BSSA14-NEA22 GMM using conventional site parameters.

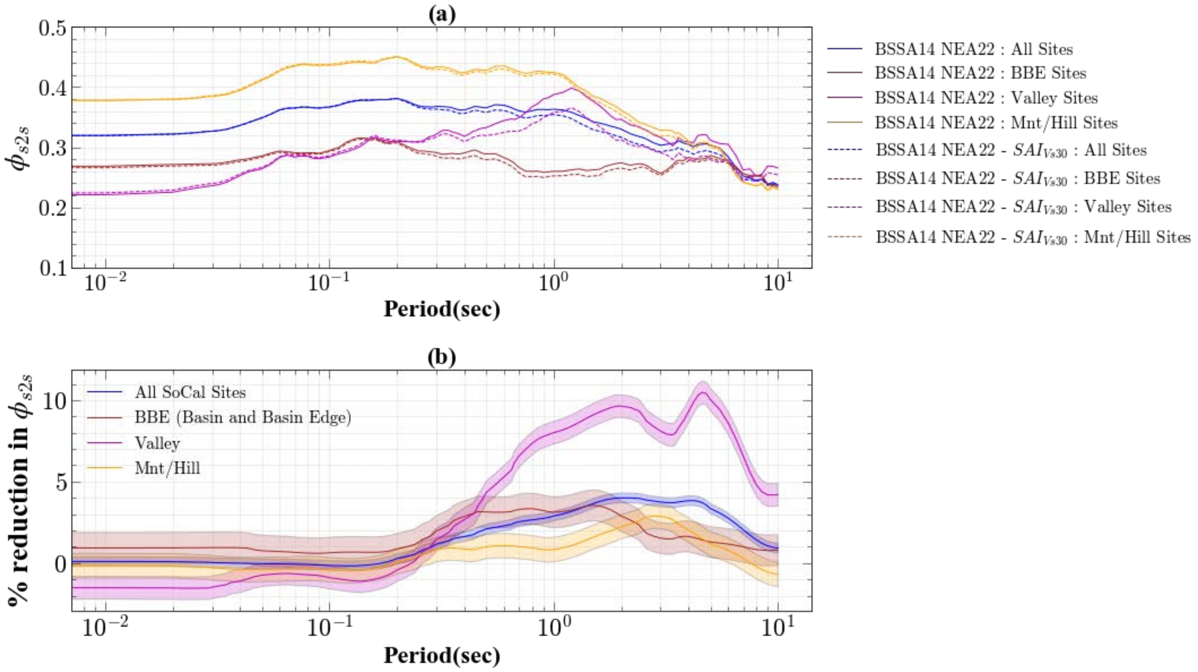

Figure 8.10: (a) Trends of Site-to-Site dispersion with period, highlighting the changes from the BSSA14-NEA22 GMM to the BSSA14-NEA22-$SAI_{V_{S30}}$ GMM for the different geomorphic categories. (b) The percent reduction quantified versus period for each geomorphic category, with the shaded regions signifying the upper and lower bound reduction percentages based on the 95% confidence interval.

Figure 8.11 shows the dispersion analysis of individual basins that reveals varying degrees of improvement, with some basins (e.g., CVB) showing significant reductions in $\phi_{S2S,j}^{geom}$, while others (e.g., LAB, IVB, SFB, and others) show minimal change. These variations might be attributed to differences in basin geometry, near-surface geology, or the range of $SAI_{V_{S30}}$ values within each basin. While $SAI_{V_{S30}}$ demonstrates promise in improving ground motion predictions, particularly for small basin and non-basin sites at longer periods, some limitations should be noted. The parameter's effectiveness may be constrained in areas with limited V_{S30} data or where near-surface conditions poorly represent deeper structure. Additionally, its performance in basins suggests potential redundancy with existing basin parameters, which warrants further investigation.

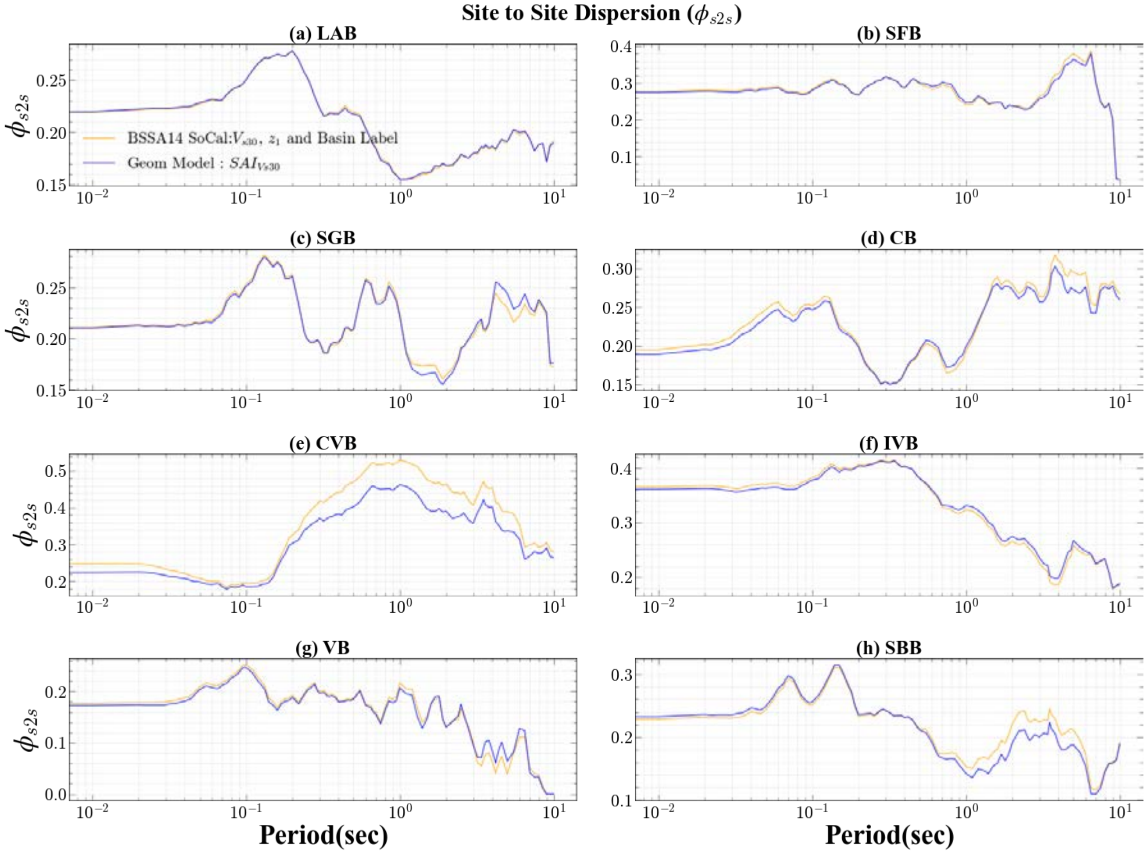

Figure 8.11: Trends of Site-to-Site dispersion with period, highlighting the changes from the BSSA14-NEA22 GMM to the BSSA14-NEA22-$SAI_{V_{S30}}$ GMM for the different sedimentary basins.

8.5 Standard Deviation of Absolute Difference between z_{cb} and $z_{1.5}$ ($SD_{|zcb-z1.5|}$) Geometric Model

Adhering to the evaluation methodology described in Section 8.2 and 8.3, we assessed the performance of the Standard Deviation of Absolute Difference between z_{cb} and $z_{1.5}$ ($SD_{|zcb-z1.5|}$) when incorporated into the BSSA14-NEA22 GMM. This parameter, designed to capture the variability in basin depth structure, showed promising results in our initial analysis in Chapter 6, specifically for the Los Angeles Basin (LAB). Figure 8.12 illustrates the relationship between $SD_{|z_{cb}-z_{1.5}|}$ and the corresponding site terms ($\eta_S^{geom}\ for\ SD_{|z_{cb}-z_{1.5}|}$) that was adjusted after its incorporation into the GMM. The reduction in the mean trends is appreciable for all periods shown compared to the original site terms trends in Figure 6.15. However, some minute discernable trends are present particularly at low values of $SD_{|z_{cb}-z_{1.5}|}$. This suggests that $SD_{|z_{cb}-z_{1.5}|}$ captures some (but not all) site effects that are not accounted for by conventional parameters.

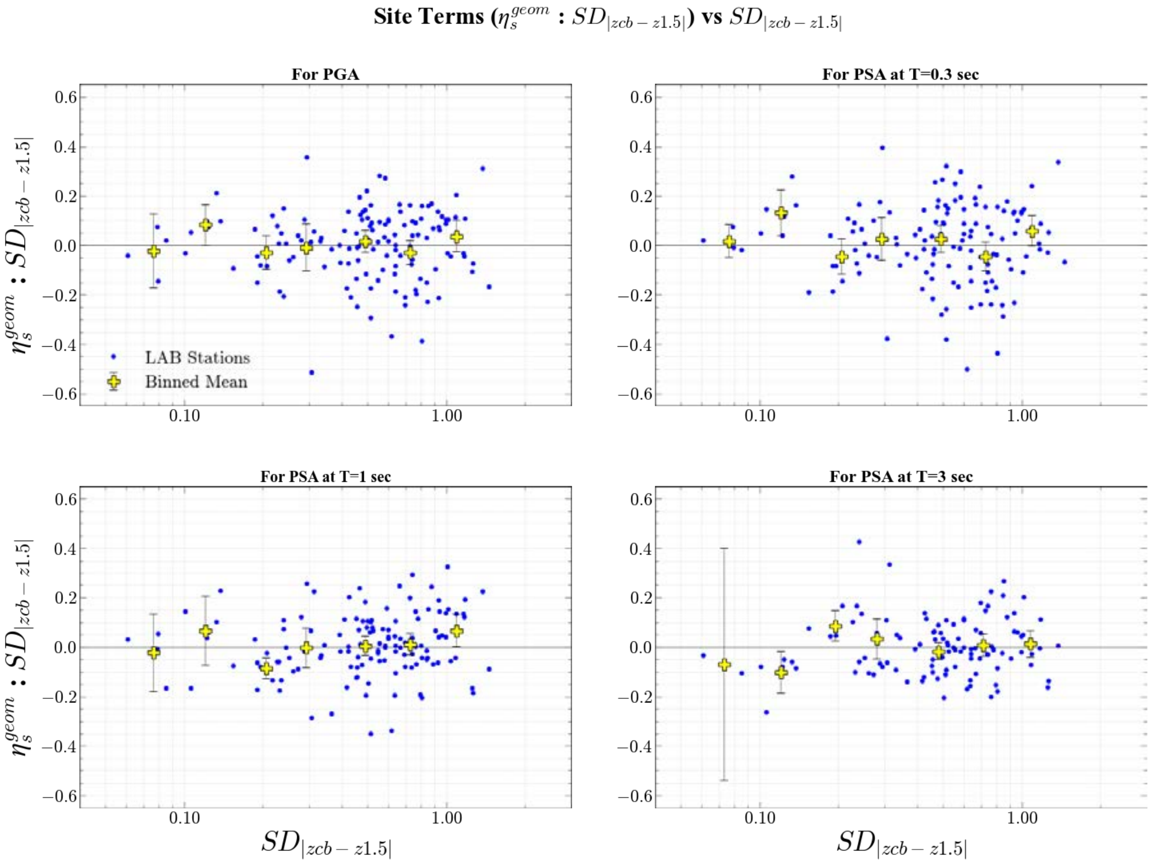

Figure 8.12: Trends of site terms (η_S^{geom} for $SD_{|z_{cb}-z_{1.5}|}$) with $SD_{|z_{cb}-z_{1.5}|}$ obtained after its incorporating into the BSSA14-NEA22.

Examining the mean site terms for LAB (Figure 8.13), we observe a significant reduction across all periods when $SD_{|z_{cb}-z_{1.5}|}$ is incorporated, with the most substantial improvements at longer periods (T > 1 second). This trend aligns with our understanding of basin effects, which tend to be more pronounced at longer periods due to the influence of deeper structure on long-wavelength seismic waves. With regards to the dispersion analysis, Figure 8.14 shows that the incorporation of $SD_{|z_{cb}-z_{1.5}|}$ leads to a substantial reduction in site-to-site variability ($\phi_{S2S,j}^{geom}$) across all periods, with improvements ranging from 20-42%. This consistent performance across the spectral range suggests that $SD_{|z_{cb}-z_{1.5}|}$ captures fundamental aspects of basin structure that influence site response at various frequencies. The effectiveness of $SD_{|z_{cb}-z_{1.5}|}$ can be attributed to its ability to represent the complexity of the depth profile within the LAB. By quantifying the variability between the crystalline basement (z_{cb}) and the 1.5 km/s velocity horizon ($z_{1.5}$), this parameter likely captures impedance contrasts and velocity gradients that play crucial roles in seismic wave amplification and propagation within the basin.

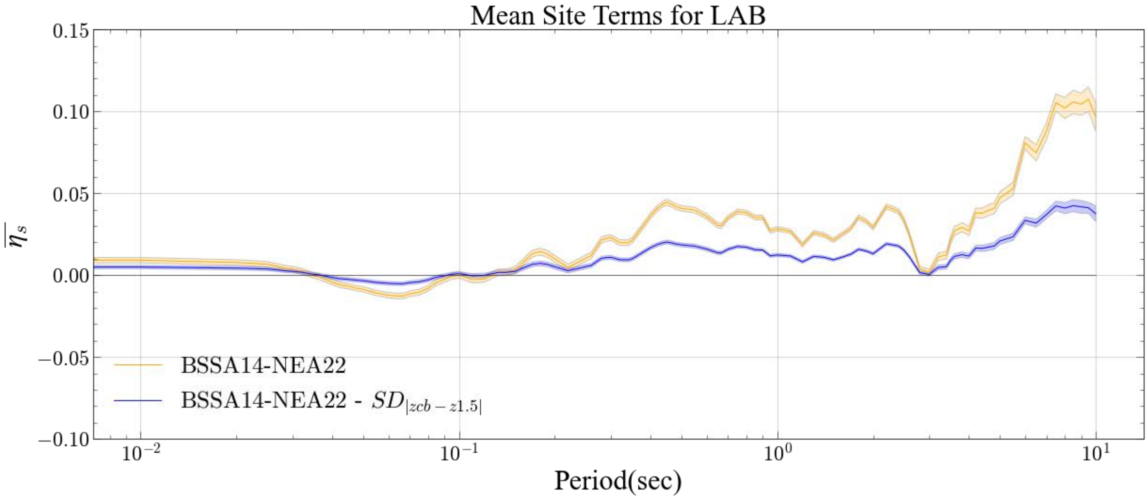

Figure 8.13: Comparison of the mean of the geometric parameter model-adjusted site terms based on $SD_{|z_{cb}-z_{1.5}|}$ for the current (BSSA14-NEA22) and proposed (BSSA14-NEA22-Geom) GMM site response model in the Los Angeles Basin (LAB).

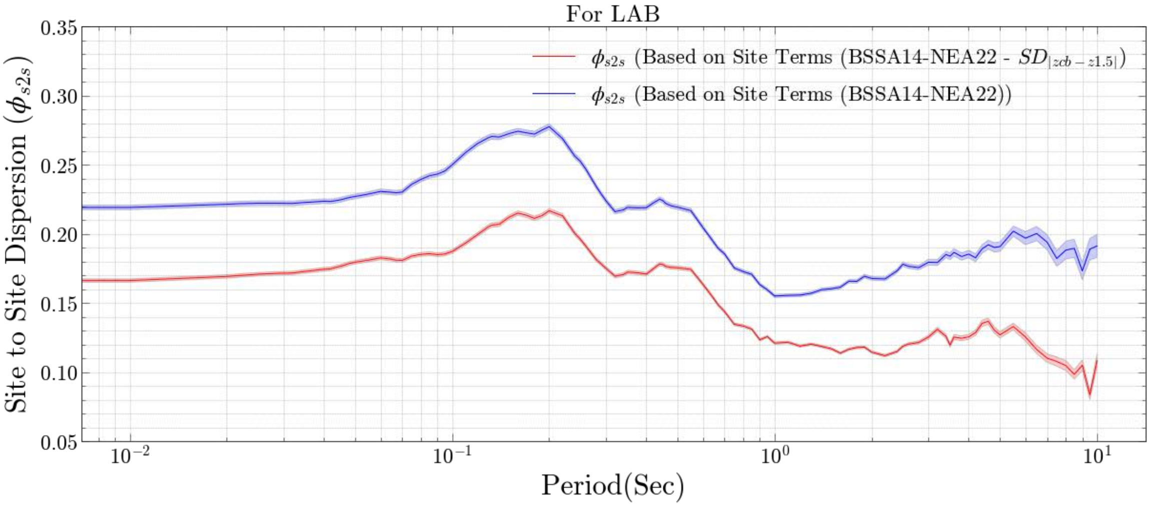

Figure 8.14: Comparison of Site-to-Site dispersion ($\phi_{S2S,j}^{geom}$) for LAB sites obtained after incorporating the $SD_{|z_{cb}-z_{1.5}|}$ model versus $\phi_{S2S,j}$ for BSSA14-NEA22 GMM using conventional site parameters.

While $SD_{|z_{cb}-z_{1.5}|}$ shows significant promise in improving ground motion predictions for the Los Angeles Basin, its broader applicability (use in areas outside the LAB) warrants additional considerations. First, the parameter's effectiveness hinges on the availability of accurate, high-resolution velocity models, which may be limited or unavailable in other regions. Moreover, its performance in areas with simpler basin structures or non-basin environments remains unexplored.

8.6 Standard Deviation of z_{cb} (SD_{zcb}) Geometric Parameter Model

Continuing our evaluation of geometric parameters, we assessed the performance of the Standard Deviation of z_{cb} ($SD_{z_{cb}}$) when incorporated into the BSSA14 GMM. This parameter was designed to capture the variability in crystalline basement depth and it showed promise in our initial analysis in Chapter 6 for the Los Angeles Basin (LAB). Figure 8.15 illustrates the relationship between $SD_{z_{cb}}$ and the corresponding site terms ($\eta_S^{geom}\ for\ SD_{z_{cb}}$) that was adjusted after its incorporation into the GMM. The reduction in the mean trends is appreciable for all periods shown compared to the original site terms trends in Figure 6.4. However, like $SD_{|z_{cb}-z_{1.5}|}$, some minute discernable trends are present particularly at low values of $SD_{z_{cb}}$. This suggests that $SD_{z_{cb}}$ captures some (but not all) site effects that are not accounted for by conventional parameters.

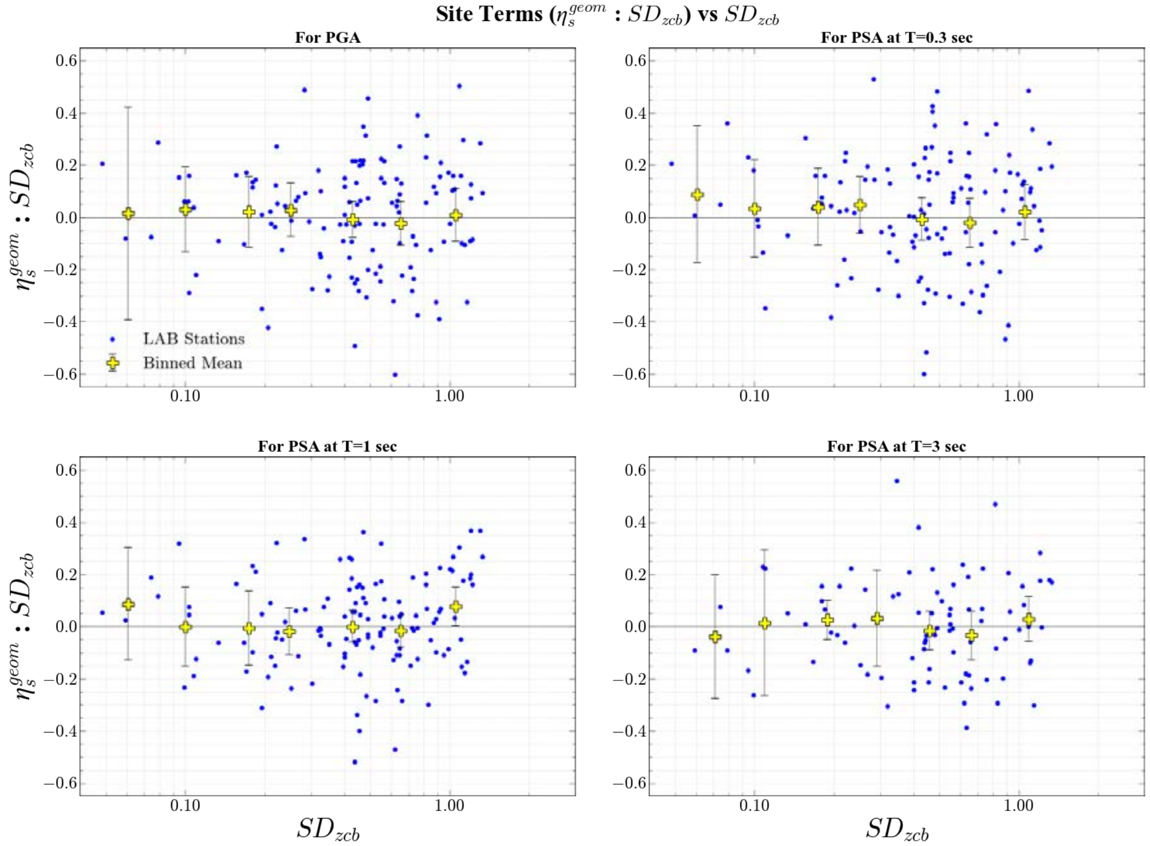

Figure 8.15: Trends of site terms (η_S^{geom} for $SD_{z_{cb}}$) with $SD_{z_{cb}}$ obtained after its incorporating into the BSSA14-NEA22.

Figure 8.16 shows that the implementation of $SD_{z_{cb}}$ in the BSSA14-NEA22 GMM leads to a notable reduction in the mean of the site terms (mean bias) across all periods for the Los Angeles basin. This reduction is pronounced at longer periods (T >1 second), which aligns with the expected behavior for basins, especially where deeper structure tends to influence longer-period ground motions. Along the same lines, Figure 8.17 shows that BSSA14-NEA22-$SD_{z_{cb}}$ GMM induces a reduction in the dispersion of the adjusted site terms on the order of 6-12% from the prior GMM (BSSA14-NEA22) across the entire spectral period range of engineering interest. The reduction range suggests that $SD_{z_{cb}}$ captures fundamental aspects of the overall Los Angeles basin structure that influence site response at various frequencies. The observed benefits of $SD_{z_{cb}}$ as a parameter for site response modeling can likely be attributed to its ability to adequately represent the Los Angeles basin's overall geometry and depth variability. By quantifying the spatial variability of the crystalline basement depth, this parameter is likely capturing large-scale basin features, such as interface gradients and orientations, that influence seismic wave propagation and amplification, such as focusing effects and the generation of propagating surface waves from the basin edges.

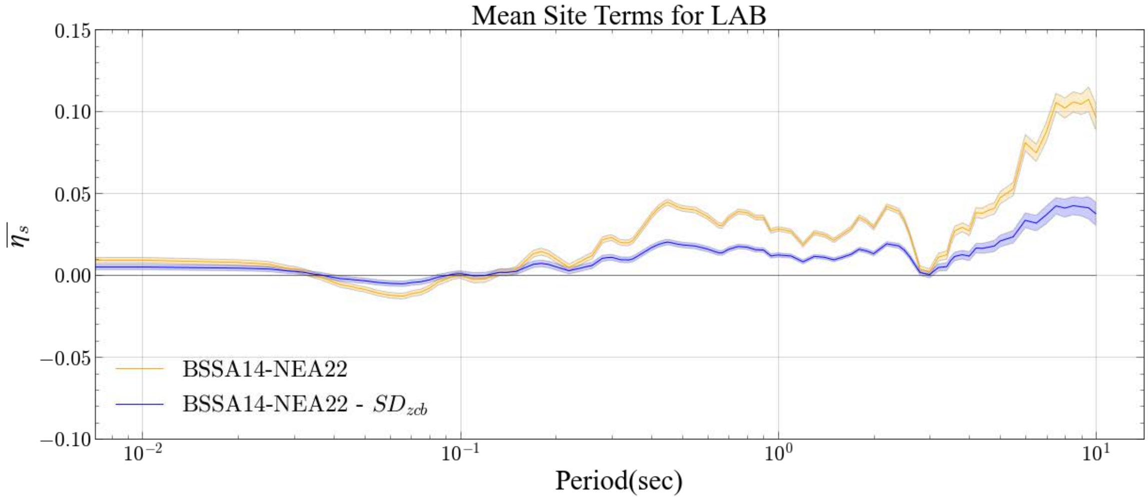

Figure 8.16: Comparison of the mean of the geometric parameter model-adjusted site terms based on $SD_{z_{cb}}$ for the current (BSSA14-NEA22) and proposed (BSSA14-NEA22-Geom) GMM site response model in the Los Angeles Basin (LAB).

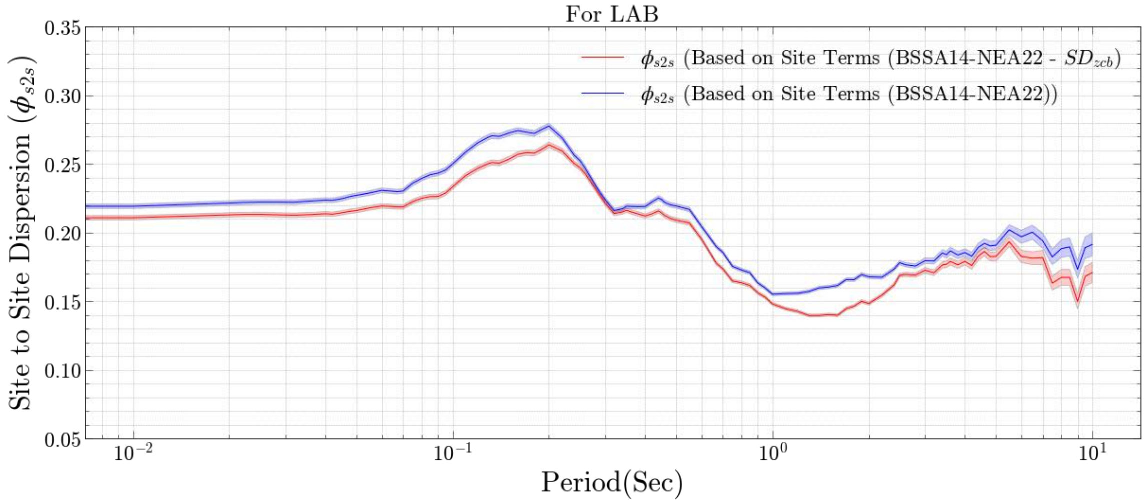

Figure 8.17: Comparison of Site-to-Site dispersion ($\phi_{S2S,j}^{geom}$) for LAB sites obtained after incorporating the $SD_{z_{cb}}$ model versus $\phi_{S2S,j}$ for BSSA14-NEA22 GMM using conventional site parameters.

Like the other depth-related geometric parameter discussed in the previous section, $SD_{z_{cb}}$ demonstrates good performance in improving ground motion predictions for LA, but they share identical limitations to consider. Due to the nature of how this parameter is derived, it is limited to LAB sites only. As a result, robust application to regions outside of LAB rely on on accurate mapping of the crystalline basement depth to be effective. Unfortunately, this resource is not available for all regions with the same level of detail as in the Los Angeles Basin. Moreover, its performance in non-basin environments or basins with less complex structure remains to be evaluated. In the following section, we will provide a synthesis of the performance of all three geometric parameters, offering comparative insights into their relative strengths and potential applications in seismic hazard assessment.

8.7 Comparison of Performance of Modelled Geometric Parameters

Following the individual performance evaluation conducted for the three selected geometric parameters ($SAI_{V_{S30}}$, $SD_{|z_{cb}-z_{1.5}|}$, $SD_{z_{cb}}$) in the previous sections of this chapter, this section focuses on a comparative assessment to of their ability to improve ground motion estimates in the Los Angeles basin (LAB). The objective of this comparison is to synthesize our findings and provide insigths into the relative effectiveness of each parameter across different spectral periods. Figure 8.18 depicts the impact of each geometric parameter on the mean of the site terms across the LAB. All three parameters show a reduction the average bias compared to the baseline model (the Nweke et al. (2022) updated BSSA14 GMM; BSSA14-NEA22), with notable reductions at high-intermediate to long periods (i.e., T > 0.6 second). At very long periods (T > 3 seconds), $SD_{|z_{cb}-z_{1.5}|}$ outperforms the other two parameters and is either comparable or slightly better at all other spectral periods. This superior performance likely stems from its ability to capture both the overall basin depth and internal velocity structural variability (i.e., how quickly are the impedance contrasts changing and where; how that correlates with between the deep interface and the ground surface). By quantifying the difference between the crystalline basement depth (z_{cb}) and the 1.5 km/s velocity horizon ($z_{1.5}$), $SD_{|z_{cb}-z_{1.5}|}$ effectively represents the significant complex 2D and 3D configurations within the basin that play a crucial role in altering and augmenting seismic wave amplification and propagation.

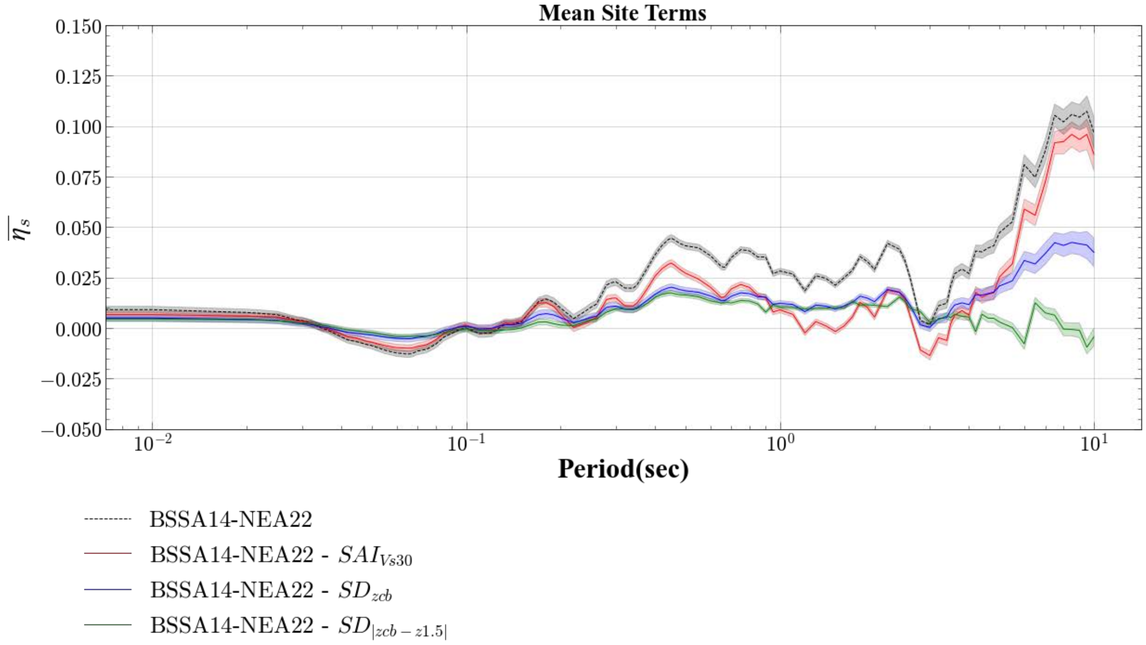

Figure 8.18: Comparison of η_S^{geom} based on the three geometric parameters ($SAI_{V_{S30}}$, $SD_{|z_{cb}-z_{1.5}|}$, $SD_{z_{cb}}$) compared with those derived from the baseline GMM (BSSA14-NEA22) for sites in the Los Angeles Basin (LAB).

Figure 8.19 shows the comparison of geometric parameter-adjusted site-to-site dispersion ($\phi_{S2S,j}^{geom}$) for each parameter model in the LAB. Similar to the mean site term plots, $SD_{|z_{cb}-z_{1.5}|}$ shows the most significant reduction in variability, at all periods. $SD_{z_{cb}}$ is the next best performing parameter with reductions in site-to-site variability across all periods, though much less than $SD_{|z_{cb}-z_{1.5}|}$. $SAI_{V_{S30}}$ is the worst performing parameter, showing very little to no reduction in site term dispersion, even though it exhibits the largest reduction in mean bias between the periods of 1 second and 3 seconds. Figure 8.20 quantifies the average changes for each geometric parameter from the baseline GMM in the form of a bar plot. The values presented confirm the visual inspection of Figure 8.19, but with the addition of the impact when $SAI_{V_{S30}}$ is applied to the broader SoCal region.

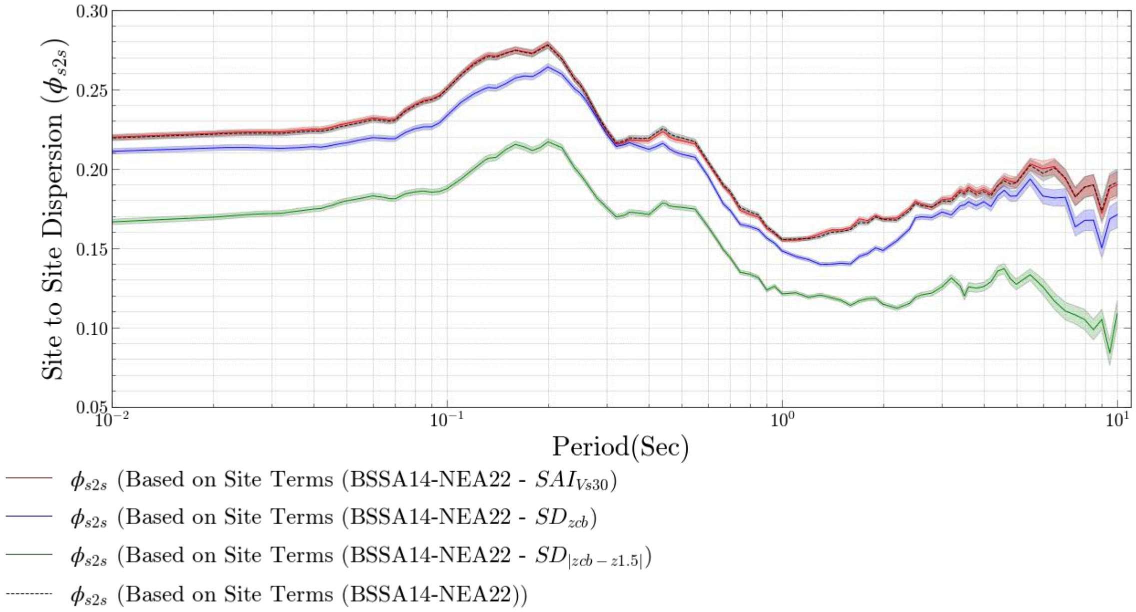

Figure 8.19: Comparison of $\phi_{S2S,j}^{geom}$ based on the three geometric parameters ($SAI_{V_{S30}}$, $SD_{|z_{cb}-z_{1.5}|}$, $SD_{z_{cb}}$) compared with those derived from the baseline GMM (BSSA14-NEA22) using conventional parameters for sites in the Los Angeles Basin (LAB).

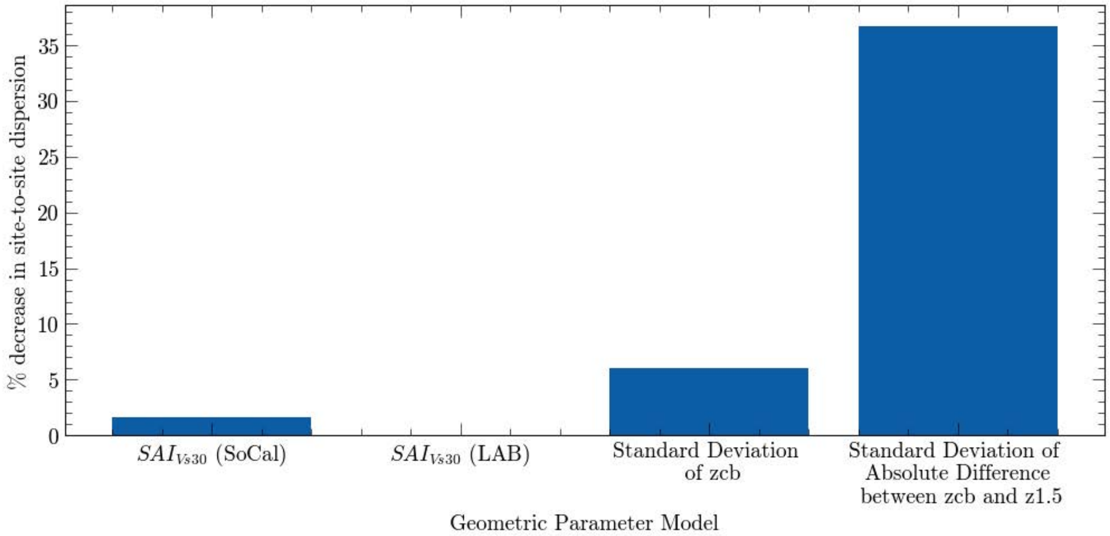

Figure 8.20: Average Percentage reduction in Site-to-Site Dispersion (across all periods) from the BSSA14-NEA22 GMM (Nweke et al. 2022) after incorporating selected geometric parameter models (BSSA14-NEA22-Geom).

The superior performance of $SD_{|z_{cb}-z_{1.5}|}$ highlights that capturing the variability in basin (LAB) structure, particularly the relationship between the crystalline basement and the overlying sedimentary layers, is crucial for improving ground motion predictions in complex basin environments. This parameter effectively accounts for the three-dimensional nature of the basin, which is especially critical for predicting for longer-period ground motions that are influenced by deeper structure. Furthermore, the improvements observed in the short period range, particularly in reducing site-to-site variability (site term dispersion), indicates that $SD_{|z_{cb}-z_{1.5}|}$ is either correlated to the shallow features at a site or it capture subtle feature/changes at depth that influence high frequency content of seismic waves. The percent reduction in dispersion shown in Figure 8.20 suggests that $SD_{z_{cb}}$ emulates the same features and abilities, but to a lesser extent than $SD_{|z_{cb}-z_{1.5}|}$. While $\mathrm{SAI}_{\mathrm{V_{S30}}}$ performs well in non-basin regions and small basins, its poor performance in large and complex basins (LAB) underscores its limitations. This parameter primarily reflects near-surface and shallow depth 2D/3D characteristics, with little to no relation to the deeper features that govern site response in large basins.

While these results are promising, it's important to note some limitations. A notable nuance to consider is that the comparative analysis is specific to the Los Angeles Basin, and the relative performance of these parameters may vary in other geological settings. Furthermore, the effectiveness of $SD_{|z_{cb}-z_{1.5}|}$ and $SD_{z_{cb}}$ relies on the availability of detailed velocity models, which may not be present for all regions. These findings have significant implications for future ground motion modeling efforts. They suggest that incorporating parameters that capture basin depth variability, particularly those that represent the relationship between different velocity horizons, can substantially improve the accuracy of ground motion predictions in basin environments. This could be particularly valuable for both deterministic and probabilistic seismic hazard analyses, especially for intermediate and more so, long-period ground motions that are critical for the response of tall buildings and long-span structures.

Future research should explore the potential for combining these parameters to capture different aspects of basin geometry and site response. Additionally, investigating the applicability of these parameters to other basin environments (as well as other site conditions and regions) and developing strategies for their incorporation into next-generation ground motion prediction equations will be crucial steps in advancing our ability to assess seismic hazards in complex geological settings.

Chapter 9: Conclusion

9.1 Summary of Key Findings

This study explored the geometric parameterization of sedimentary basins in Southern California (SoCal) to enhance site response analysis and modeling. Building upon the strengths of traditional one-dimensional site parameters like V_{S30}, basin depth, and basin category (discussed in Chapter 1 and 2), we addressed some of their limitations by investigating a suite of geometric parameters to capture two- and three-dimensional site response effects. These parameters would complement the conventional GMM site parameters by augmenting their estimates of site response. This approach, within an ergodic formulation (the Nweke et al. 2022 update to the Boore et al. 2014 GMM: BSSA14-NEA22), resulted in an enhanced partially non-ergodic framework that progresses towards fully non-ergodic predictions. Figure 9.1 provides a schematic representation of the workflow adopted in this study.

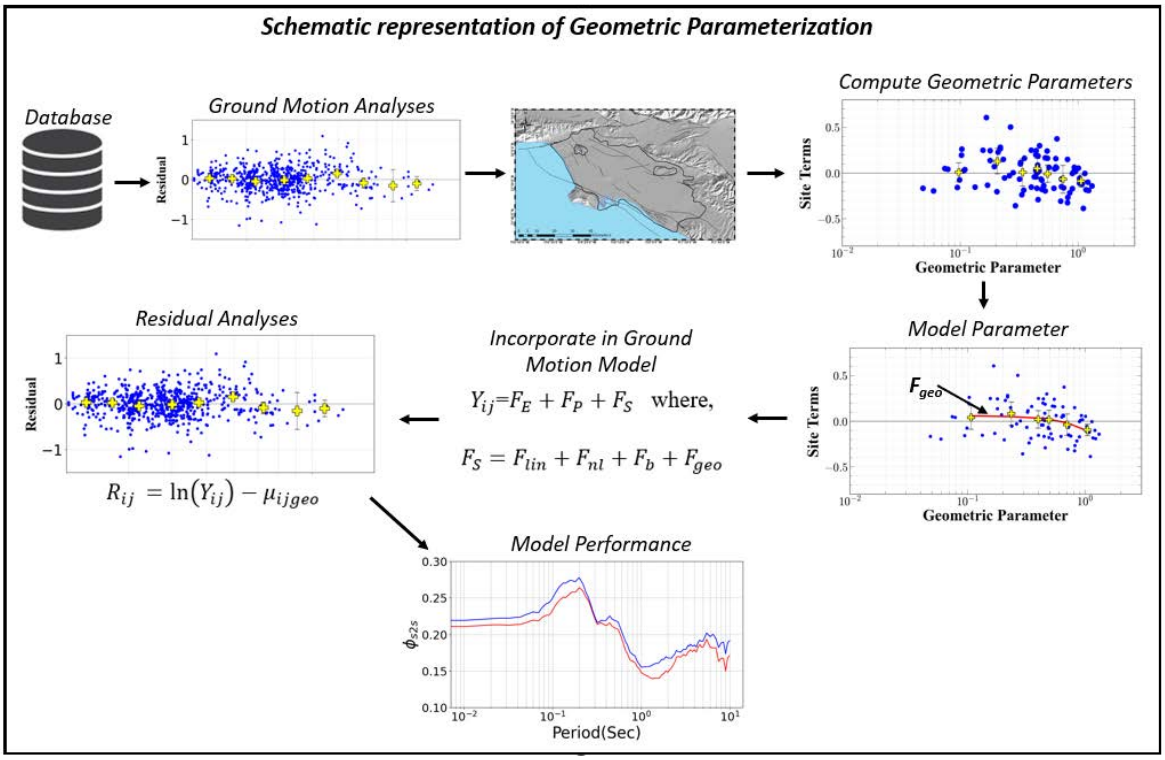

Figure 9.1: A schematic representation of the research workflow summary, including the various steps involved in studying and modelling geometric parameters.

Our analysis of the Los Angeles Basin (LAB) shape and depth constraints (discussed in Chapter 5) led to several key outcomes. The primary outcome was the establishment of a defined sedimentary basin boundary at the surface that help constrain the extents of basin-related site conditions in our dataset. Next, was the determination of the sediment-crystalline bedrock interface extents, which combined with the aforementioned outcome served as the reference for the derivation of the geometric parameters. This effort also allowed for the description of intra-basin heterogeneities. Moreover, we adopted $z_{1.5}$ and $z_{2.3}$ surfaces as appropriate iso-surfaces to represent the impedance contrasts associated with the stiffest sedimentary formation above the crystalline basement interface. These findings provided a crucial foundation for subsequent parameter development and analysis.

Through comprehensive exploration of various geometric parameters (Chapter 6), we identified three promising candidates:

1. Spatial Area of Influence based on V_{S30} ($SAI_{V_{S30}}$)
2. Standard Deviation of z_{cb} ($SD_{z_{cb}}$)
3. Standard Deviation of Absolute Difference between $z_{1.5}$ and z_{cb} ($SD_{|z_{cb}-z_{1.5}|}$)

These parameters are geometric representations of the combined multidimensional features related to depth and lateral extents, showing potential to complement traditional site parameters in capturing basin-related site effects.

Our investigation of V_{S30} scaling slopes (Chapter 7) revealed significant bias between individual basins and the overall SoCal scaling model. This finding underscores the unique characteristics of different basins and the importance of basin-specific considerations in site response analysis.

9.2 Model Performance and Implications

The incorporation of our selected geometric parameters into ground motion models (Chapter 8) demonstrated promising results:

1. $SAI_{V_{S30}}$, modeled for SoCal, showed particular effectiveness for non-basin sites, which include valley sites (small basin areas) and mountain/hill sites. It reduced the mean bias and site-to-site variability, especially at intermediate and longer periods.
2. $SD_{|z_{cb}-z_{1.5}|}$ and $SD_{z_{cb}}$, modeled for LAB, significantly reduced mean bias and site-to-site variability within the basin across all periods, including shorter periods.

These improvements addressed key limitations of traditional site parameters. The reduction in site-to-site variability ranged from 2% to 37% on average, depending on the parameter and site conditions (Figure 8.20), representing a substantial improvement in our ability to predict site response.

9.3 Practical Implications and Recommendations

The findings from this research investigation have several practical implications for engineers and seismologists working in seismic hazard assessment. In SoCal, particularly for non-basin sites, incorporating $SAI_{V_{S30}}$ can improve site response predictions by capturing lateral variability not accounted for by traditional 1D parameters. For the LAB, using $SD_{|z_{cb}-z_{1.5}|}$ or $SD_{z_{cb}}$ as complementary parameters to V_{S30}, basin depth, and basin category can enhance the accuracy of site-specific analyses, especially in areas with complex subsurface geometry. We also identified a 2 km threshold from basin boundaries for distinguishing basin edge sites, which should be considered when characterizing sites near basin margins. These recommendations can be integrated into current practices to refine site response analyses and potentially improve seismic hazard assessments in regions with complex basin structures.

9.4 Limitations and Future Work

While our study advances the understanding of the effects of 2D/3D subsurface characteristics (deep and shallow) on site response, several limitations should be noted. The applicability of our findings is primarily constrained to SoCal basins, particularly the LAB. Basins with different geological histories may require separate investigations. Additionally, the effectiveness of some of the identified parameters ($SAI_{V_{S30}}$) in reducing uncertainty for basin sites was less pronounced than for non-basin sites, indicating room for further improvement.

Future research directions should include extending this analysis to other basins in SoCal and beyond, including the San Francisco Bay Region and the California Central Valley. Investigating the performance of these parameters in basins with different geological origins, such as glacial basins, would also be valuable. Further exploration of additional geometric parameters that might capture basin effects not accounted for in this study could yield additional insights. By the same token, parameters that were assessed in the study but not used in model development could show viable predictive capabilities in other types of basins and regions. In particular, SAI_{VS} (Spatial Area of Influence based on the slope of the shear wave velocity profile), C_b (Distance from Basin Centroid/Basin Eccentricity), and R^b_{mar} (Distance from Basin Margin) could provide good performance under different site conditions in other regions. Finally, developing methodologies to integrate these parameters into probabilistic seismic hazard analysis frameworks would be a crucial next step in applying these findings to practical seismic hazard assessment.

9.5 Concluding Remarks

This study represents a significant step towards more comprehensive characterization of site response in complex basin environments. By complementing traditional one-dimensional site parameters with carefully selected geometric parameters, we can improve our ability to predict and model seismic site effects. As we continue to refine these methods and extend them to diverse geological settings, we move closer to more accurate and reliable seismic hazard assessments, ultimately contributing to enhanced earthquake resilience in urban areas situated on sedimentary basins.

9.6 Data Availability

Electronic supplements for geometric parameters computed for SoCal and LAB sites as well as shapefiles are published as DesignSafe Project-4667 (Nweke and Shams, 2024): Geometric Parameterization of Sedimentary Basin in Southern California. The DesignSafe project provides the ability to view the distribution of the parameters and their values throughout the area of interest. It also provides access to all the resources used for the analysis in this research investigation.

References

Aki, K., & Richards, P. G. (2002). Quantitative seismology.

Abrahamson, N. A., & Youngs, R. R. (1992). A stable algorithm for regression analyses using the random effects model. Bulletin of the Seismological Society of America, 82(1), 505-510.

Abrahamson, N. A., Silva, W. J., & Kamai, R. (2014). Summary of the ASK14 ground motion relation for active crustal regions. Earthquake Spectra, 30(3), 1025-1055.

Al Atik, L., Abrahamson, N., Bommer, J. J., Scherbaum, F., Cotton, F., & Kuehn, N. (2010). The variability of ground-motion prediction models and its components. Seismological Research Letters, 81(5), 794-801.

Ancheta TD, Darragh RB, Stewart JP, Seyhan E, Silva WJ, Chiou BS-J, Wooddell KE, Graves RW, Kottke AR, Boore DM, Kishida T, Donahue JL (2014) NGA-West2 database. *Earthquake Spectra,* 30(3): 989–1005.

Assimaki, D., Ledezma, C., Montalva, G. A., Tassara, A., Mylonakis, G., & Boroschek, R. (2012). Site effects and damage patterns. *Earthquake Spectra*, *28*(1_suppl1), 55-74.

Bard, P. Y., & Bouchon, M. (1985). The two-dimensional resonance of sediment-filled valleys. Bulletin of the Seismological Society of America, 75(2), 519-541.

Bates, D., Mächler, M., Bolker, B., & Walker, S. (2015). Fitting linear mixed-effects models using lme4. Journal of Statistical Software, 67(1), 1-48.

Beyer L. A. (1988). Summary of geology and petroleum plays used to assess undiscovered recoverable petroleum resources of Sacramento Basin province, California. United States Geological Survey, 10.3133/ofr88450

Boore, D. M., Stewart, J. P., Seyhan, E., & Atkinson, G. M. (2014). NGA-West2 equations for predicting PGA, PGV, and 5% damped PSA for shallow crustal earthquakes. Earthquake Spectra, 30(3), 1057-1085.

Catchings, R. D., Gandhok, G., Goldman, M. R., Okaya, D., Rymer, M. J., & Bawden, G. W. (2008). Near-surface location, geometry, and velocities of the Santa Monica fault zone, Los Angeles, California. *Bulletin of the Seismological Society of America*, *98*(1), 124-138.

Campbell, K. W., & Bozorgnia, Y. (2014). NGA-West2 ground motion model for the average horizontal components of PGA, PGV, and 5% damped linear acceleration response spectra. *Earthquake Spectra*, *30*(3), 1087-1115.

Choi, Y., Stewart, J. P., & Graves, R. W. (2005). Empirical model for basin effects accounts for basin depth and source location. Bulletin of the Seismological Society of America, 95(4), 1412-1427.

Chiou, B and R Youngs. (2014). Update of the Chiou and Youngs NGA model for the average horizontal component of peak ground motion and response spectra. Earthquake Spectra 30(3), 1117-1153. https://doi.org//10.1193/072813EQS219M.

Davis, T., and Namson, J., (1998) Southern California Cross Section Study Cross-Section 12-12', USGS Cross Section 12.pdf (davisnamson.com)

Davis, P. M., Rubinstein, J. L., Liu, K. H., Gao, S. S., & Knopoff, L. (2000). Northridge earthquake damage caused by geologic focusing of seismic waves. *Science*, *289*(5485), 1746-1750.

Day, S. M., Graves, R., Bielak, J., Dreger, D., Larsen, S., Olsen, K. B., ... & Juve, G. (2008). Model for basin effects on long-period response spectra in southern California. Earthquake Spectra, 24(1), 257-277.

Gao, S., Liu, H., Davis, P. M., & Knopoff, L. (1996). Localized amplification of seismic waves and correlation with damage due to the Northridge earthquake: evidence for focusing in Santa Monica. *Bulletin of the Seismological Society of America*, *86*(1B), S209-S230.

Gautier, L. (2009). rpy2: A simple and efficient access to R from Python. URL http://rpy.sourceforge.net/rpy2.html.

Graves, R. W., Pitarka, A., & Somerville, P. G. (1998). Ground-motion amplification in the Santa Monica area: Effects of shallow basin-edge structure. Bulletin of the Seismological Society of America, 88(5), 1224-1242.

Graves, R., et al. (2011). CyberShake: A physics-based seismic hazard model for southern California. Pure and Applied Geophysics, 168(3-4), 367-381.

Field, E. H., & Jacob, K. H. (1995). A comparison and test of various site-response estimation techniques, including three that are not reference-site dependent. *Bulletin of the seismological society of America*, *85*(4), 1127-1143.

Ingersoll, R. V., & Rumelhart, P. E. (1999). Three-stage evolution of the Los Angeles basin, southern California. Geology, 27(7), 593-596.

Kawase, H. (1996). The cause of the damage belt in Kobe: "The basin-edge effect," constructive interference of the direct S-wave with the basin-induced diffracted/Rayleigh waves. Seismological Research Letters, 67(5), 25-34.

Kishida T, Darragh RB, Chiou BSJ, Bozorgnia Y, Mazzoni S, Contreras V, Boroschek R, Rojas F and Stewart JP (2020) Chapter 3 Ground motions and intensity measures Data resources for NGA-subduction project. PEER Report 2020/02. Berkeley, CA: Pacific Earthquake Engineering Research Center, UC Berkeley.

Lee, E. J., Chen, P., Jordan, T. H., Maechling, P. B., Denolle, M. A., & Beroza, G. C. (2014). Full-3-D tomography for crustal structure in southern California based on the scattering-integral and the adjoint-wavefield methods. *Journal of Geophysical Research: Solid Earth*, *119*(8), 6421-6451.

Ma, Y., & Clayton, R. W. (2016). Structure of the Los Angeles Basin from ambient noise and receiver functions. Geophysical Journal International, 206(3), 1645-1651.

McCulloh, T.H., and Beyer, L.A. (2003). Mid-Tertiary Isopach and Lithofacies Maps for the Los Angeles Region, California: Templates for Palinspastic Reconstruction to 17.4 Ma. U.S. Geological Survey Professional Paper 1690.

Nweke, C. C., Stewart, J. P., & Brandenberg, S. J. (2020). Site response of southern California sedimentary basins and other geomorphic provinces. *Report GIRS-2020-12202012*. Doi: https://doi.org/10.34948/N3159F

Nweke, C. C., Stewart, J. P., Wang, P., & Brandenberg, S. J. (2022). Site response of sedimentary basins and other geomorphic provinces in southern California. Earthquake Spectra, 38(4), 2341-2370.

Nweke, C. C., & Shams, R. (2024). "Geometric Parametrization of Sedimentary Basins in Southern California", in *Geometric Parametrization of Sedimentary Basins in Southern California*. DesignSafe-CI. https://doi.org/10.17603/ds2-54xr-mm22

Nweke, C. C., & Shams, R., (202x) "Southern California Basin and Non-Basin Classification Algorithm for Ground Motion Site Amplification Model Applications" *In review* at Earthquake Spectra

Olsen, K. B. (2000). Site amplification in the Los Angeles basin from three-dimensional modeling of ground motion. Bulletin of the Seismological Society of America, 90(6B), S77-S94.

Pilz, M., Parolai, S., Stupazzini, M., Paolucci, R., & Zschau, J. (2011). Modelling basin effects on earthquake ground motion in the Santiago de Chile basin by a spectral element code. *Geophysical Journal International*, *187*(2), 929-945.

R Core Team (2019) *R: A Language and Environment for Statistical Computing*. Vienna: R Foundation for Statistical Computing.

Rodriguez-Marek A, Rathje EM, Bommer JJ, Scherbaum F and Stafford PJ (2014) Application of single-station sigma and site-response characterization in a probabilistic seismic-hazard analysis for a new nuclear site. Bulletin of the Seismological Society of America 104: 1601–1619.

Sawyer, D.S., Hsui, A.T., and Toksöz, M.N. (1987). Extension, subsidence and thermal evolution of the Los Angeles basin—a two-dimensional model. Tectonophysics, 133(1-2), 15-32.

Seed, H. B., Romo, M. P., Sun, J. I., Jaime, A., & Lysmer, J. (1988). The Mexico earthquake of September 19, 1985—Relationships between soil conditions and earthquake ground motions. Earthquake Spectra, 4(4), 687-729.

Seyhan, E., & Stewart, J. P. (2014). Semi-empirical nonlinear site amplification from NGA-West2 data and simulations. Earthquake Spectra, 30(3), 1241-1256.

Shaw, J. H., et al. (2015). Unified structural representation of the southern California crust and upper mantle. Earth and Planetary Science Letters, 415, 1-15.

Stafford, P. J. (2014). Crossed and nested mixed-effects approaches for enhanced model development and removal of the ergodic assumption in empirical ground-motion models. Bulletin of the Seismological Society of America, 104(2), 702-719.

Stafford, P. J., Rodriguez-Marek, A., Edwards, B., Kruiver, P. P., & Bommer, J. J. (2017). Scenario dependence of linear site-effect factors for short-period response spectral ordinates. *Bulletin of the Seismological Society of America*, *107*(6), 2859-2872.

Thompson, E. M., Baise, L. G., Tanaka, Y., & Kayen, R. E. (2014). A taxonomy of site response complexity. Soil Dynamics and Earthquake Engineering, 41, 32-43.

Wills, Christopher & Gutierrez, Carlos & Perez, Ante & Branum, David. (2015). A Next Generation VS30 Map for California Based on Geology and Topography. Bulletin of the Seismological Society of America. 105. 10.1785/0120150105.

Wright, T.L. (1991). Structural geology and tectonic evolution of the Los Angeles Basin, California. Active Margin Basins, 52, 35-134.

Wright, T.L. (I987), Geologic summary of the Los Angeles basin, in Wright, T., and Heck, R., eds., Petroleum geology of coastal southern California: American Association of Petroleum Geologists, Pacific Section, no. 60, p. 21-31.

Yerkes, R.F., et al. (1965). Geology of the Los Angeles Basin, California: An Introduction. U.S. Geological Survey Professional Paper 420-A.

Bibliography

Geometric Parameterization of Sedimentary Basins for Seismic Site Response Analysis and Modelling, *Poster presented at Seismology Student Workshop organized by Lamont-Doherty Earth Observatory, Columbia University*, 15-17 March 2023. *(Poster)*

Geometric Parameters for Seismic Site Response in Sedimentary, *Poster presented at Physics-Based Ground Motion Modeling, SSA, 10-13 October 2023, Vancouver, BC (Poster)*

Shams, R, Nweke, C. C., Parker, G. A., (202x),"Site Response Models based on Geometric Parameter for Southern California Sedimentary Basins", In preparation, to be submitted to *Earthquake Spectra*.

Shams, R, Nweke, C. C., Parker, G. A., (202x), "Identifying Geometric Parameters for Site Response Modelling in Los Angeles and other Southern California Sedimentary Basins", In preparation, to be submitted to *Earthquake Spectra*.